HYDROGEN BOND TOPOLOGY: ORDER/DISORDER TRANSITIONS IN ICE AND THE BEHAVIOR OF DEFECTS IN A DISORDERED ICE LATTICE

DISSERTATION

Presented in Partial Fulfillment of the Requirements for

the Degree Doctor of Philosophy in the

Graduate School of The Ohio State University

By

Christopher J. Knight, B.S.

* * * * *

The Ohio State University

2009

Dissertation Committee:

Professor Sherwin J. Singer, Adviser

Professor James V. Coe

Professor Russell M. Pitzer

Approved by

_____

Adviser

Graduate Program in Chemistry

ABSTRACT

To date, fifteen phases of ice have been discovered. Many of these phases occur in pairs consisting of a fully ordered member and a hydrogen bond (H-bond) disordered phase. The disordered phase contains the water oxygens in nearly the same positions as the fully ordered phase, but the orientations of hydrogens are disordered. Our research examines the phase transitions between members of these ordered/disordered pairs. These transitions are sluggish because they occur at such low temperatures that water molecules cannot easily rotate to rearrange the directions in which the hydrogen bonds point. It is defects in the ice lattice that make the transitions possible. For instance, ice Ih transforms to ice XI only when doped with hydroxide ions, but many questions linger about the mechanism since experiments suggest that hydroxide ions are not mobile near the transition temperature. In this dissertation, theoretical methods are introduced which are capable of describing the small energy differences among the innumerable H-bond configurations of the water molecules in ice. The theory uses input from periodic electronic density functional theory calculations for small unit cells to parameterize interactions in terms of the H-bond topology. This parameterization enables statistical mechanical calculations for systems large enough to approximate the thermodynamic limit. Our calculations were the first to confirm that ordinary ice, a disordered phase, transforms into a fully ordered counterpart, ice XI. For those disordered phases for which an ordered version has been experimentally

characterized, our methods yield transition temperatures in good agreement with experiment. We also proposed a candidate structure to experimentalists for proton-ordered ice VI, for which an ordered version has yet to be observed. We have also extended these methods to describe the interactions of the H-bond topology with defects (ionic and orientational) and oxygen site-disorder. We have successfully constructed a model to describe a hydroxide ion in an ice Ih lattice. We found that the lowest-energy configuration surrounding the ion is the experimentally proposed ice XI structure. When coupled to the proton transfer events between hydroxide and water, our statistical mechanical simulations provide a description of defect diffusion within the disordered H-bond network.

Dedicated to all my family and friends...

ACKNOWLEDGMENTS

I am immensely thankful to Mom, Dad, Brad, Matt, and the rest of my family for their constant love and support. I am indebted to Nicole for always being there when it was time to escape and relax, whether it was a night out at the bar or a weekend trip to Europe. My sincere gratitude goes to my advisor, Dr. Singer, for his guidance throughout my time here at Ohio State. I am grateful to Dr. Coe and Dr. Pitzer for serving on my dissertation examination committee, carefully reading my manuscript, and all of the help and assistance they have given to me over the years. I'm thankful to all of the great friends that I have made here in Columbus. In particular, I'm thankful to Sara, Matt, Travis, and Gab for all of the great times, especially that first year and those still to come. Of course, I can't forget how grateful I am to my fellow group members Tanping, Yun, Ali, Hui, and Corey for all of the mischief and entertaining conversations, not necessarily about science. I am appreciative to the Winking Lizard for its awe-inspiring beer selection. I would also like to thank the chemistry department, the Ohio State University, and National Science Foundation for funding and the Ohio Supercomputing Center for resources.

VITA

November 11, 1981	Born - Lincoln Park, MI, USA
2003	B.S., Eastern Michigan University
2003-2007	Graduate Teaching and Research Associate, The Ohio State University
2008	Presidential Fellow, The Ohio State University
2009-present	Graduate Research Associate, The Ohio State University

PUBLICATIONS

Research Publications

1. Christopher Knight and M. C. Milletti, "Theoretical characterization of two reaction pathways for the intramolecular cyclization of 2-(3-benzylaminopropanoylamino)benzamide", *J. Mol. Struct.: THEOCHEM* **724**:143 (2005)

2. Sherwin J. Singer, Jer-Lai Kuo, Tomas K. Hirsch, Chris Knight, Lars Ojamäe and Michael L. Klein, "Hydrogen bond topology and the ice VII/VIII and Ih/XI proton ordering phase transitions", *Phys.Rev.Lett.* **94**(13):135701 (2005)

3. Chris Knight and Sherwin J. Singer, "Prediction of a phase transition to a hydrogen bond ordered form of ice VI", *J. Phys. Chem.* **B109**(44):21040 (2005)

4. Chris Knight, Sherwin J. Singer, Jer-Lai Kuo, Tomas K. Hirsch, Lars Ojamäe and Michael L. Klein, "Hydrogen bond topology and the ice VII/VIII and Ih/XI proton ordering phase transitions", *Phys.Rev.* **E73**(5):056113 (2006)

5. Chris Knight and Sherwin J. Singer, "A re-examination of the ice III/IX hydrogen bond ordering phase transition ", *J. Chem. Phys.* **125**(6):064506 (2006)

6. Chris Knight and Sherwin J. Singer, "Tackling the problem of hydrogen bond order and disorder", *Physics and Chemistry of Ice* (Proceedings of the 11th International Conference on the Physics and Chemistry of Ice), ed., Werner F. Kuhs (Royal Soc. of Chemistry, 2007), p.329

7. Chris Knight and Sherwin J. Singer, "Theoretical study of a hydroxide ion within the ice-Ih lattice", *Physics and Chemistry of Ice* (Proceedings of the 11th International Conference on the Physics and Chemistry of Ice), ed., Werner F. Kuhs (Royal Soc. of Chemistry, 2007), p.339

8. Chris Knight and Sherwin J. Singer, "Hydrogen bond ordering in ice V and the transition to ice XIII", *J. Chem. Phys.* **129**(16): 164513 (2008)

FIELDS OF STUDY

Major Field: Chemistry

TABLE OF CONTENTS

LIST OF FIGURES

LIST OF TABLES

CHAPTER 1

INTRODUCTION

Water is a unique substance. All other compounds made up of small molecules – nitrogen, oxygen, carbon dioxide, for example – exist only as gases on earth. In contrast, water is commonly found as a vapor, liquid or solid. The uniqueness of water arises because of the strong attractions, known as "hydrogen bonds," between water molecules. Not only are hydrogen bonds (H-bonds) unusually strong, they are directional.

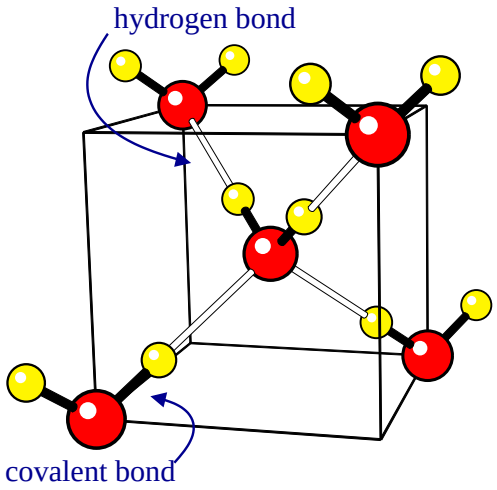

Figure 1.1: A set of 4 non-adjacent corners from among the 8 corners of a cube define the tetrahedral directions for hydrogen bonds.

A water molecule prefers to accept two H-bonds and donate two other H-bonds in tetrahedral directions (Fig. 1.1). When liquid water is cooled below 0°C, ice is formed. In this phase of ice, called ice Ih, the oxygen atoms of water form a periodic lattice, an infinitely repeating pattern. The hydrogen atoms, however, do not form a periodic lattice (Fig. 1.2), though they are always found in between two oxygen atoms forming a covalent bond with one oxygen and an H-bond with the other oxygen. The water molecules in ice always donate and accept two H-bonds. This is such a well accepted notion that the previous statements are recognized as the "ice rules" and have been used for decades. [1]

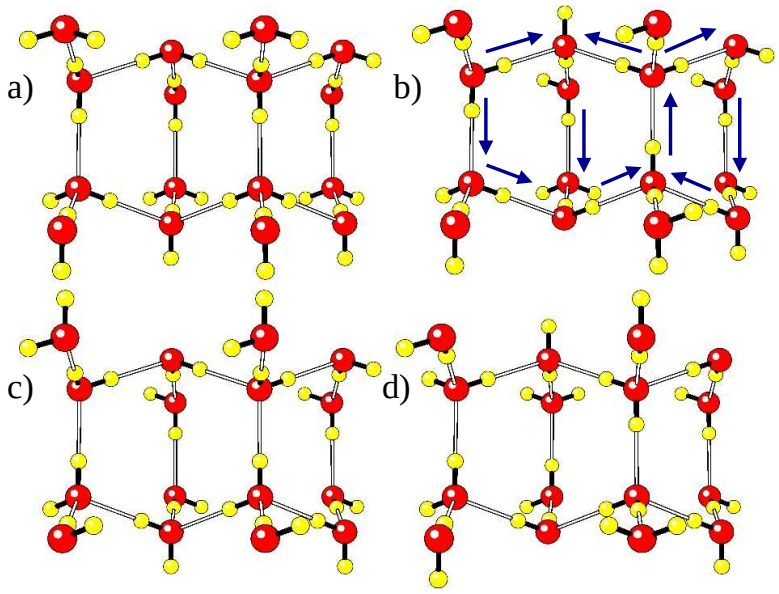

Figure 1.2: Four possible arrangements of H-bonds within a 16-water-molecule unit cell of ice Ih. The H-bonds in ice can be described by arrows which point from H-bond donor to H-bond acceptor as shown for isomer (b).

In 1935, Linus Pauling [15] predicted that there are $(3/2)^N$ different ways to arrange the H-bonds of N water molecules in an ice Ih lattice subject to the "ice

rules" for which several examples are shown in Fig. 1.2. Pauling's estimate would prove to be remarkably accurate. In the following year, Giauque and Stout [16] measured the disorder of ice Ih near 0 K and the experiments agreed with Pauling's estimate. The experiment confirmed that the H-bonds in ice are in a nearly random arrangement, i.e. the H-bonds are disordered. The third law of thermodynamics states that as the temperature is lowered to 0 K (absolute zero), the entropy of a crystalline system approaches zero. If ice were to behave as a perfect pure crystal, then its entropy would drop to zero at 0 K and, somewhere between the freezing temperature of water and 0 K, all H-bonds in ice should become ordered.

Little progress was made concerning a possible low-temperature form of ice until the 1980's, when calorimetry experiments on samples doped with impurities, particularly potassium hydroxide (KOH), exhibited a clear signature of a proton ordering transition at 72 K. [2, 17] The transition temperature was independent of the KOH concentration, suggesting that KOH acts like a catalyst. This proton-ordered structure is called ice XI, i.e. it was the eleventh crystalline phase of ice characterized in the literature. The mechanism by which KOH induces the proton ordering transition in ice Ih is unclear. Furthermore, the structure of ice XI is most unexpected. It has a net electrical polarization, meaning that a crystal has negatively and positively charged ends. This type of crystal is called a ferroelectric, in analogy with iron magnets (ferromagnets) which have magnetic north and south ends. Over the years, there has been continued debate and research as to whether the H-bond arrangements in ice are actually random, whether a phase transition to a fully H-bond-ordered structure exists, and if so, its identity. To give an example of the debate in the literature, a skeptical viewpoint was expressed by Cowin and co-workers [18]: "Over the years

there have been many UFI citings (underidentified ferroelectric ices) in the literature regarding ice I, often where the hope was high, and the data suggestive, that a fully proton-ordered ice phase was created." Our calculations were the first to confirm that ice XI was the low-temperature form of ordinary ice. [19, 20] Our calculated transition temperature, 98 K, is in good agreement with experiment, 72 K. Predictions of H-bond ordering in ice encounter several obstacles.

An important approximation made in Pauling's estimate was that all allowed H-bond configurations occurred with equal probability which implies that the energy differences between isomers is zero. Realistically, these energy differences are not exactly zero, but are indeed very small. It has been shown that commonly used models disagree amongst each other with regard to the subtle energetic ordering of H-bond isomers in ice Ih and by an order of magnitude with respect to the range of energy differences. [21] Furthermore, none of the models predicted the ground state to be the ice XI structure, including one they constructed with that hope in mind. [21] We overcome the problem of determining H-bond energetics via electronic density functional theory (DFT) calculations which we have found yields accurate results for the relative energetics of H-bond isomers.

While it may be feasible to perform electronic structure calculations on several H-bond isomers for a small unit cell (10−100 waters), it would certainly be impractical to perform the same level of calculation on the numerous H-bond isomers of a unit cell (thousands of waters) large enough to obtain good statistics. We solve the problem of statistical sampling of H-bond configurations by linking the energy of a configuration to the orientation of the H-bonds, the arrows in Fig. 1.2. We have developed group theoretical tools to construct analytic expressions, as functions of the

H-bond orientations, which exploit the symmetry of the ice lattice. [20, 22] We can then use these functions, what we call graph invariants, to describe scalar physical properties of the system, such as energy. Graph invariants provide us with a means to "bootstrap" from expensive DFT calculations for small unit cells to statistical mechanics simulations using much larger cells.

At present, there are fifteen crystalline phases of ice whose structures have been characterized and reported in the literature. [1] In total, there are five phases of disordered ice (Ih, III, V, VII, and XII as highlighted in Fig. 1.3) which when cooled under appropriate conditions transform to a proton-ordered version (XI, IX, XIII, VIII, and XIV respectively). The proton-ordered version of another disordered phase, ice VI, has yet to be identified experimentally. The VII−VIII system is the best characterized of all the proton order/disorder transitions in ice. Calculations using the graph invariant methodology predict that, of all possible H-bond isomers, ice VII transforms into the correct low-temperature ice VIII structure. The calculated transition temperature of 228 K is in good agreement with experimental reports in the range 263−274 K. [19,20] As stated above, an ordered version of ice VI has not yet been experimentally characterized, although various attempts have been made. Using graph invariants coupled with electronic structure calculations, we find a transition to a ferroelectric proton-ordered phase at 108 K. [23] Thus, we were able to propose to experimentalists a candidate structure for proton-ordered ice VI.

The disordered phases of ice discussed above are regarded as nearly fully disordered phases. Neutron diffraction studies on ices III and V, however, have shown that these phases are only partially disordered, i.e. some H-bond arrangements are preferred over others. The degree of partial order/disorder can be determined experimentally using

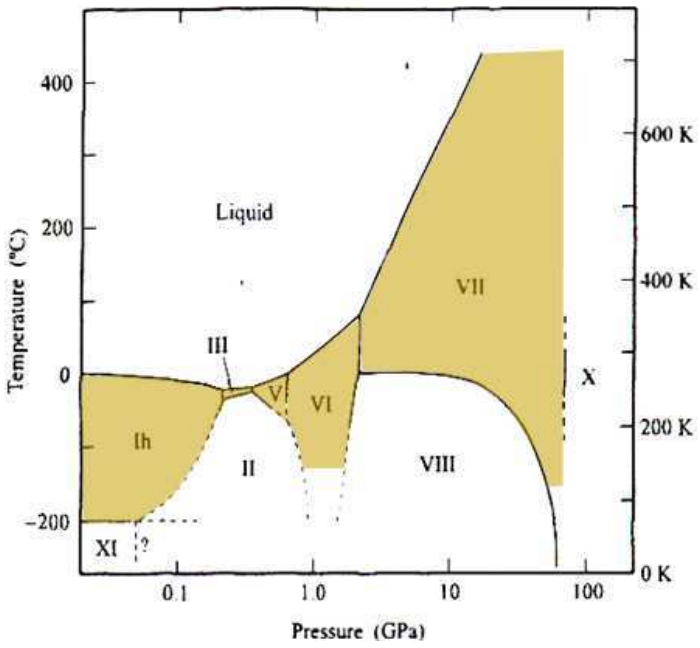

Figure 1.3: A series of H-bond disordered phases, the shaded regions in the figure, surround the liquid in the phase diagram of water. [1]

diffraction and/or calorimetry techniques to measure occupational probabilities and the transition entropy respectively. For the ice III−IX system, we again found that the ground state configuration and transition temperature agree with experiment. [24] Because our work includes a statistical mechanical treatment of H-bond fluctuations, we can estimate the degree of partial H-bond order in the high-temperature disordered phases and partial disorder in the low-temperature ordered phases. Our calculated transition entropies are in good agreement with available experiment and we have been able to provide some insight regarding an apparent contradiction in the literature.

It was only recently that the proton-ordered versions of ices V and XII were first reported. Similar to the ice Ih/XI system, these proton ordering transitions were

only observed in the presence of a small amount of dopant, in this case HCl. It has been stated in the literature [25], "It would be a challenging test of the ability of modern day computational methods to reproduce our experimentally found lowest energy state." With our methods, we have found that the ground state configuration agrees with the experimental ice XIII structure as well as provide insight into the degree of partial ordering. [26]

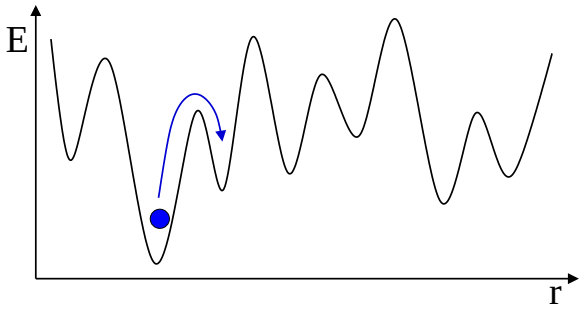

Figure 1.4: Defects in ice move in a random potential created by the disordered hydrogen bonds.

In the work discussed so far, no defects were present in the ice lattices. The ordering transitions of ice Ih, V, and XII only occur when a small amount of dopant is present presumably introducing defects. Recent experiments indicate that ionic defects are immobilized on an accessible experimental time scale somewhere between 100−200 K. [27, 28] If there are no ionic defects actively diffusing at 72 K, then it is unclear how hydroxide ions catalyze the ice Ih/XI transition. In ice Ih, the H-bond disorder sets up a random medium (Fig. 1.4) for the defects to diffuse with potential traps for defects. With an appropriate description of defects in ice, the mobility of

defects throughout the disordered ice lattice, and hence the mechanism of H-bond order and disorder in ice, could be studied.

To date, we have successfully extended graph invariants to describe a hydroxide ion and its accompanying orientational defect in an ice Ih lattice. We have found that the lowest energy configuration agrees with the experimentally proposed ice XI structure. [29] We are currently analyzing the proton transfer between water molecules and hydroxide ions in ice. Hydroxide ions in an ice lattice accept three H-bonds and donate a single H-bond. Hydroxide ion motion occurs via proton transfer from one of the three donating water molecules to the hydroxide ion, as illustrated in Fig. 1.5.

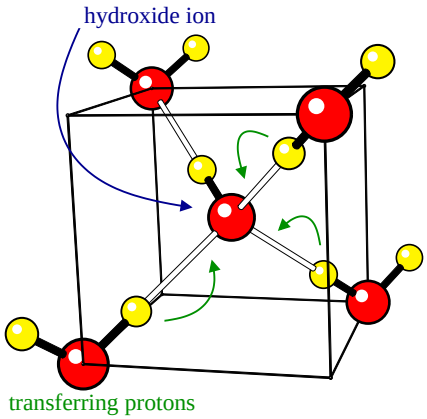

Figure 1.5: Hydroxide motion in ice occurs when protons transfer from water molecules to the hydroxide ion.

After the proton hops across the H-bond, the water molecule and hydroxide ion will have switched places resulting in migration of the hydroxide within the ice lattice. Coupling this "microscopic" proton transfer event with our "macroscopic" statistical mechanical simulations, using graph invariants, will provide a description of defect diffusion within the disordered H-bond network.

CHAPTER 2

PREDICTION OF THE Ih/XI AND VII/VIII PROTON ORDERING PHASE TRANSITIONS

2.1 Introduction

As mentioned in chapter 1, Linus Pauling [15], in 1935, predicted that there were $(3/2)^N$ different ways to arrange the hydrogen bonds (H-bonds) of N water molecules in an ice Ih lattice, "ordinary ice", subject to the ice rules. The ice rules state that each oxygen must be covalently bonded to two hydrogens, there is only one hydrogen per bond, and each water molecule accepts a maximum of two hydrogens from other waters, as illustrated in Fig. 2.1. The following year, Giauque and Stout measured the entropy of ice Ih near 0 K to be $Nk_B \ln \frac{3}{2}$ within experimental error. [16] Pauling's estimate proved to be remarkably accurate and was verified when the exact result was calculated to be 1.5069^N. [10] This nonzero entropy implies that somewhere between freezing and 0 K, ordinary ice becomes a proton glass with a quenched, nearly random, arrangement of H-bonds. There has been continued debate and research as to whether the H-bond arrangements are truly random, whether a phase transition to a fully proton-ordered structure exists, and if so, the identity of that structure.

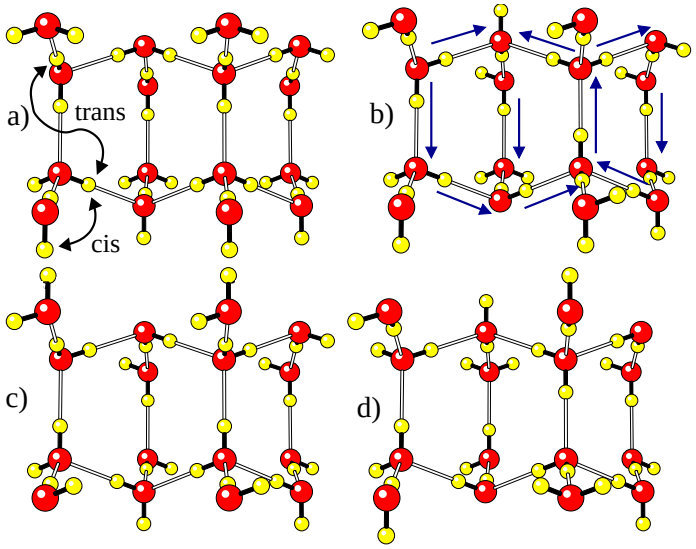

Figure 2.1: Four possible arrangements of H-bonds within a 16-water 2x1x1 orthorhombic unit cell of ice Ih. Cis and trans H-bonds are defined as whether protons lie on the same or opposite side of the H-bond respectively, as indicated for isomer (a). The H-bond isomers are summarized mathematically by directed graphs in which directional bonds point from H-bond donor to H-bond acceptor, as illustrated for isomer (b).

Close to the melting point of ice, the protons are fully disordered subject to the ice rules. As ice is cooled to low temperatures, proton motion comes to a halt, and a glassy transition has been observed to occur ∼110 K [30] prohibiting the transition to a proton-ordered phase. As tabulated in Ref. [31], numerous dielectric studies on powder and single crystal samples have been performed over the years. Kawada and Niinuma reported results on dielectric studies on single crystals with a Curie-Weiss temperature of 46 K and 55 K for H_2O [32, 33] and D_2O [34] respectively with the electric field parallel to the $c-$axis. Studies by Johari and Whalley on powdered samples of H_2O indicate a Curie-Weiss temperature significantly lower, 6.2 K [31].

However, in samples doped with impurities, particularly KOH, it was observed that there is a clear calorimetric signature of a first order phase transition at 72 K with weak dependence on the concentration of the KOH impurity. [17, 34] In experiments with samples of D_2O, the transition temperature is shifted by four degrees to 76 K. Antarctic ice samples have been examined with neutron diffraction and Raman spectroscopy. It is believed that these samples, kept at a constant low temperature for thousands of years, have equilibrated to a proton-ordered arrangement [35]. These studies indicate that a second-order phase transition to an H-bond ordered phase of ice occurs at 237 K, which is significantly larger than the observed transition temperature in KOH doped ice samples. Neutron diffraction spectra of Greenland ice samples, prepared under similar conditions, showed no distinct differences when compared to the spectra of ice Ih, thus casting doubt on the earlier Antarctic studies. [36] Additional diffraction studies on Antarctic ice samples concur that it is unlikely that a proton-ordered arrangement can be observed under such conditions. [37]

The unit cell of ice Ih, Fig. 2.2, is hexagonal with space group $P6_3/mmc$. The symmetry of the low-temperature proton-ordered configuration, ice XI, shown in Fig. 2.2c, is orthorhombic, space group $Cmc2_1$, as indicated by neutron scattering [2–5] and thermal depolarization experiments [6, 7] on KOH-doped ice Ih. Bonds that are oriented parallel to the $c-$axis all point in the same direction. The $ab-$layers, composed of bonds oriented perpendicular to the $c-$axis are polarized parallel to the $b-$axis with alternating layers oppositely aligned. Thus, the structure is overall anti-ferroelectric in the $a-$ and $b-$directions and ferroelectric in the $c-$direction. This anti-ferroelectric arrangement of the $ab-$layers gives rise to a slight displacement of the oxygen lattice parallel to the $b-$axis in the direction of the polarization. The calculated shift,

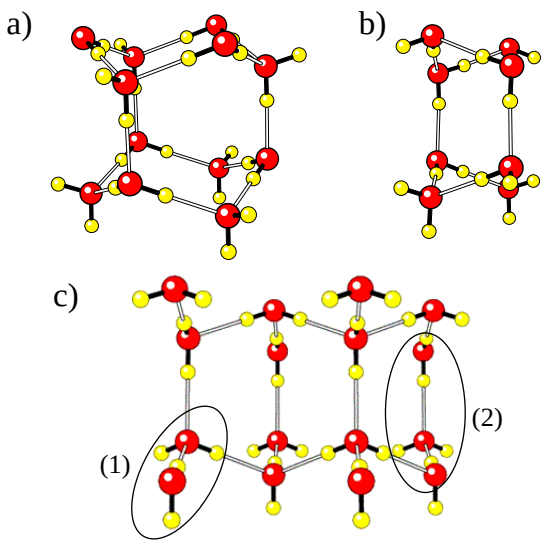

Figure 2.2: a) A $1 \times 1 \times 1$ hexagonal unit cell of ice Ih, space group $P6_3/mmc$, containing 12 water molecules. b)A $1 \times 1 \times 1$ orthorhombic unit cell of ice Ih, space group $Cmc2_1$, containing 8 waters. Both unit cells are appropriate for describing the relative energetics of the H-bond isomers possible in each unit cell. Bonds that appear to point straight up and down are parallel to the $c-$axis and hence called $c-$axis bonds. The remaining bonds, perpendicular to the $c-$axis, are referred to as $ab-$bonds. c) Proposed experimental structure of proton ordered ice Ih, ice XI, as determined from diffraction and thermal depolarization experiments [2–7]. The $ab-$layer bonds(1) are all cis with the ab-layers polarized parallel to the $b-$axis and alternating layers oppositely aligned. The $c-$axis bonds(2) are trans and all oriented in the same direction. Cis and trans H-bonds are defined, respectively, as to whether the non-hydrogen bonded hydrogens fall on the same or opposite side of the H-bond.

0.11 Å, determined from the optimized geometry of the ice XI configuration, calculated as described below, is in agreement with the experimentally determined shift of 0.12 Å [2].

This view has been contested: Iedema *et al.* [18] referred to more recent claims as "UFI citings (underidentified ferroelectric ices) in the literature." Even if the $Cmc2_1$ structure proves to be correct, there is some justification for characterizing

the current state of knowledge of low-temperature ice Ih/XI as "underidentified." While a mechanism has been proposed for incomplete conversion of ice Ih to ice XI [38], several features of the presumed ice Ih/XI transition are not understood. While the calorimetric signature of the Ih/XI transition is remarkably insensitive to KOH concentration, the amount of conversion, as measured by the total heat of transformation, is strongly concentration dependent. If KOH truly acts as a catalyst and samples have adequate time to equilibrate, there should be no concentration dependence. The KOH seems to be playing another role, perhaps related to the crystal strain discussed by Johari [38]. Furthermore, there are reports that protons in ice become immobile below a certain temperature due to being trapped by the defects present in ice [39]. Wooldridge and Devlin performed FT-IR experiments which indicated that proton motion comes to a halt below 100 K [27]. More recently, "soft-landing" experiments by Cowin *et al.* indicate that hydronium ions are in fact immobile at all temperatures below 190 K [28]. If hydroxide is as immobile as excess protons at low temperature, then the basis for the catalytic role of hydroxide would be cast in doubt. Recent dielectric and calorimetric experiments [40] indicate that the alkali hydroxide dopants polarize nearby water molecules to promote orientational ordering at low temperatures which may explain the observed weak concentration dependence on the amount of transformation achieved.

In contrast to the controversy surrounding the ice Ih/XI proton ordering phase transition, the ice VII/VIII transition has been well characterized. The ice VII/VIII proton ordering transition will then serve as a means for validating our theoretical methods. Ice VII was first identified by Bridgman [41] in 1937. Ice VII has one of the simplest structures of all the high pressure phases of ice, two interpenetrating, but

not interconnected ice Ic lattices. The unit cell of the ice VII crystal is cubic, space group $Pn3m$, containing 2 water molecules. X-ray [42, 43] and neutron [44] diffraction studies indicate that the H-bonds in ice VII, the structure of which is shown in Fig. 2.6, are fully disordered subject to the ice rules. Ice VIII is the corresponding low-temperature proton-ordered structure. The ice VIII unit cell is tetragonal, space group $I4_1/amd$, containing 8 water molecules. Both sub-lattices are ferroelectrically aligned parallel to the $c-$axis, but the sub-lattices are oriented opposite to one another resulting in an overall anti-ferroelectric structure. The relative oxygen positions remain essentially unchanged from that of the ice VII structure except for a small distortion, $\sim$0.2 Å [45], arising from the nonbonded oxygen-oxygen interactions between the sub-lattices.

The ice VII/VIII proton ordering transition was first observed when dielectric experiments indicated that the Debye relaxation disappeared below 0°C [46]. Over a range of pressures from 2.1 to 12 GPa, proton ordering, via rearrangement of H-bonds, occurs at nearly constant temperature. All experiments are in general agreement on the ice VII/VIII transition temperature, 263 to 273 K [44,47], although hysteresis [48] effects make the precise determination difficult. The effects of D_2O on the transformation are negligible at these temperatures, shifting on the order of a degree [49], indicating quantum effects are minimal. In the ice Ih-XI transition, the transition temperature shifts from 72 K for H_2O to 76 K for D_2O. With still higher pressure, the ice VII/VIII transition temperature abruptly decreases as the mechanism of the transition shifts to proton tunneling across the shortened H-bonds. Our calculations are pertinent to the temperature independent region.

Predictions of H-bond ordering in ice encounters several obstacles. Buch, Sandler, and Sadlej [21] showed that commonly used empirical potentials disagree amongst each other with regard to the subtle energetic ordering of the H-bond isomers in ice Ih and by an order of magnitude with respect to the range of energy differences. Furthermore, none of the empirical potentials predicted the ground state to be the $Cmc2_1$ crystal structure, Fig. 2.2, suggested by diffraction data, including a potential they constructed with that hope in mind. We overcome the problem of determining H-bond energetics by using electronic DFT calculations. Below, we report results from three DFT methods that yield consistent results for the relative energetics of H-bond isomers, including the identification of the ground state. In the future, empirical potentials capable of describing the energetics of H-bond isomers in ice may be available. Even if that goal is realized, it is useful to have a method in which the construction of empirical potentials is entirely circumvented. The data presented in this work provides a benchmark by which future empirical potentials can be calibrated.

While it may be feasible to perform electronic structure calculations on a handful of H-bond isomers for a small unit cell, it would certainly be impractical to perform the same level of calculation on the $\sim(\frac{3}{2})^N$ H-bond isomers of a unit cell large enough to obtain good statistics. We solve the problem of statistical sampling of H-bond configurations by linking energy to hydrogen-bond topology using graph invariants [19,22,50–52], combinations of H-bond variables which are invariant to symmetry operations of the appropriate space group and are therefore appropriate variables for describing scalar physical properties. Graph invariants provide a means to "bootstrap" from expensive DFT calculations for smaller unit cells to statistical mechanics simulations using a larger unit cell.

In section 2.2, we gently introduce the graph techniques we use to link hydrogen bond topologies to scalar physical quantities. A more detailed account can be found in previous works [22, 51]. Graph invariants are then validated, in section 2.4, as an appropriate method of treating H-bond fluctuations in a large simulation cell by direct comparison to experimental data on the proton ordering transition in the ice VII/VIII system. In section 2.5, we discuss the agreement among various DFT methods in describing the energetics of H-bond isomers for two unit cells of ice Ih and present the results of statistical simulations on the ice Ih/XI proton ordering phase transition.

2.2 Introduction to Graph Invariants for Ice

Each hydrogen bond in ice consists of a single hydrogen covalently bonded to the oxygen from the donor molecule and hydrogen bonded to the second oxygen from the acceptor molecule. Hence, H-bonds are directional and conventionally taken to point from donor to acceptor, as shown in Fig. 2.3. The H-bond network can then be summarized mathematically by oriented graphs, vertices connected by directed lines. The direction of the rth H-bond in the ice lattice is specified by a bond variable b_r which takes values ± 1 according to whether the bond points along, or opposite to, an arbitrarily defined canonical direction for that bond. The directed graph of Fig. 2.3b defines our canonical orientation of the H-bonds in the 2-water primitive unit cell of ice VII. The bond variables b_1, b_2, b_3, and b_4 for one of the actual H-bond isomers of ice VII are assigned the value of $+1$ when they point in the directions shown in Fig. 2.3b, and -1 when they point in the opposite direction. Examples of directed graphs for the 2-water unit cell of ice VII are shown in the bottom of Fig. 2.3.

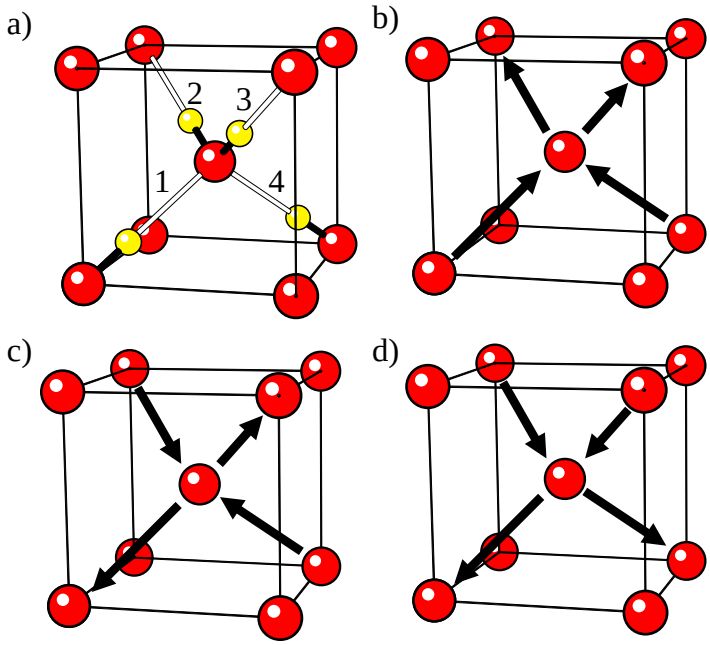

Figure 2.3: a) An isomer of a 2-water primitive unit cell of ice VII, obeying the Bernal-Fowler ice rules, is shown. The thin black lines outline the unit cell and neighboring oxygen atoms are included for clarity. The H-bonds are labeled from 1 to 4 to provide a means to associate a bond variable, b_r, with the H-bond labeled r. b) The H-bond configuration in (a) is summarized by a directed graph. The H-bonds are taken to point from oxygen donor to oxygen acceptor as discussed in the text. c, d) Additional directed graphs corresponding to other H-bond isomers of ice VII that satisfy the ice rules and periodicity constraints. As an example, if all the bond variables, b_r, for configuration (b) were assigned the value $+1$, then all the b_r's for configuration (d) would take the value -1 since all H-bonds are reversed.

Some graphs or their corresponding H-bond isomers may be related to others by one or more symmetry operations, such as rotations, reflections, and translations. In this simple exercise using the highly symmetric unit cell of ice VII, it so happens that all H-bond configurations of this primitive unit cell, obeying the ice rules and periodicity constraints, are related to every other graph via symmetry operations of the corresponding symmetry group, space group $Pn3m$ for ice VII, and thus there

is only one symmetry-distinct H-bond configuration. Therefore, scalar properties, such as energy, should be equivalent for all H-bond configurations allowed in this unit cell. In larger unit cells, the possible graphs can be partitioned into sets (orbits) of symmetry-related configurations. All scalar physical properties, such as the energy, must be identical for all configurations within a set. If the energy depends on the topological features of the H-bond configuration, then it must depend on functions of bond variables, b_r, that are themselves equivalent under symmetry operations [22,51].

Functions of bond variables that are invariant to symmetry operations of the corresponding symmetry group can be constructed by the application of the projection operator for the totally symmetric representation, $\hat{G}$. Application of the projection operator on a single bond variable, b_r, yields

$$I_r = \hat{G}(b_r) = \frac{1}{|G|}\sum_{\alpha=1}^{|G|} g_\alpha(b_r), \tag{2.1}$$

where g_α is a symmetry element of the group G, $|G|$ is the number of symmetry elements in the group, and the sum is performed over all elements in the group G. I_r is referred to as a first-order graph invariant constructed by application of the projection operator to bond r and is an intensive quantity. For systems with sufficient symmetry, most first-order invariants are algebraically equal to zero. A necessary and sufficient condition for any graph invariant to be identically zero is the existence of symmetry elements that take bond b_r into minus itself: [51]

$$g_\alpha(b_r) = -b_r. \tag{2.2}$$

Higher order graph invariants, $I_{rs}, I_{rst}, \ldots$, can be constructed as follows,

$$I_{rs} = \hat{G}(b_r b_s) = \frac{1}{|G|}\sum_{\alpha=1}^{|G|} g_\alpha(b_r b_s), \tag{2.3}$$

$$I_{rst} = \frac{1}{|G|} \sum_{\alpha=1}^{|G|} g_\alpha(b_r b_s b_t), \ldots, \tag{2.4}$$

where I_{rs} is a second-order graph invariant, I_{rst} is a third-order graph invariant, etc. For the primitive cell of ice VII, all first-order invariants are algebraically zero. Application of the projection operator for the totally symmetric representation onto all pairs of bonds yields two unique second-order graph invariants,

$$I_{1,1} = \frac{1}{4}(b_1^2 + b_2^2 + b_3^2 + b_4^2), \tag{2.5}$$

$$I_{1,2} = \frac{1}{6}(b_1 b_2 + b_1 b_3 + b_1 b_4 - b_2 b_3 - b_2 b_4 - b_3 b_4). \tag{2.6}$$

The details of constructing $I_r(b_1, b_2, \ldots)$ and $I_{rs}(b_1, b_2, \ldots)$ given the crystalline space group are provided in another publication. [22] The action of the projection operator on bond pairs $b_r b_s$ when $r = s$ yield Eq. (2.5) while all permutations of r and s such that $r \neq s$ yield Eq. (2.6). Evaluating the second-order graph invariants for the H-bond configurations in Fig. 2.3 yields $I_{1,1} = 1$ and $I_{1,2} = 0$ for all three configurations. The second-order invariant $I_{1,1}$ effectively counts the number of H-bonds in the system, which is a constant for all H-bond configurations allowed by the ice rules and periodicity constraints. Since $I_{1,2}$ is zero for all possible H-bond configurations allowed in this primitive cell, both second-order invariants will have the same value for all H-bond isomers allowed by the ice rules and periodicity constraints reflecting the fact that there is only one symmetry distinct H-bond isomer possible in the primitive unit cell of ice VII. A more interesting exercise, although still relatively simple, would be to analyze the invariants obtained from a unit cell of ice VII measuring $2 \times 1 \times 1$ primitive cells on each side as shown in Fig. 2.4. There are three symmetry-distinct isomers allowed in this unit cell. All first-order invariants for this cell are identically

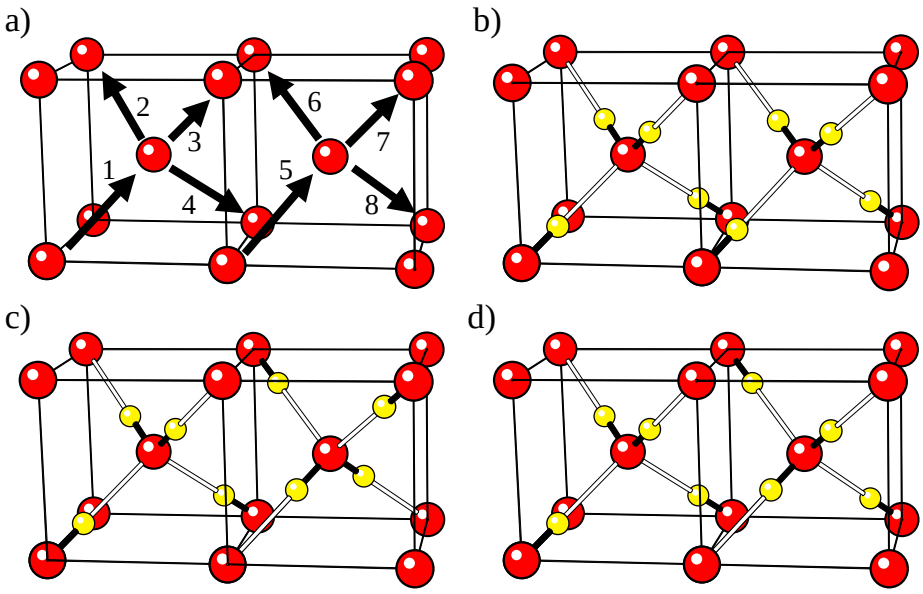

Figure 2.4: a) The canonical orientation of H-bonds, obeying the Bernal-Fowler ice rules, for a unit cell of ice VII measuring $2 \times 1 \times 1$ primitive cells on each side. The black lines outline the primitive unit cells and neighboring oxygen atoms are included for clarity. H-bonds are labeled so as to identify a bond variable, b_r, with H-bond r. The orientation of H-bonds in this isomer are assigned to be the canonical arrangement of H-bonds and all bond variables are assigned the value $+1$. b$-$d) Isomers of three symmetry-distinct H-bond configurations possible in this unit cell. The bond variables for each of the three configurations, assigned according to H-bond configuration (a), are given in Table 2.1.

zero and there are four unique second-order invariants,

$$I_{1,1} = \frac{1}{8}[b_1b_1 + b_2b_2 + b_3b_3 + b_4b_4 + b_5b_5 + b_6b_6 + b_7b_7 + b_8b_8] \quad (2.7)$$

$$I_{1,2} = \frac{1}{24}[2b_1b_2 - 2b_3b_4 + 2b_5b_6 - 2b_7b_8 + b_1b_3 - b_2b_3 + b_1b_4 - b_2b_4 + b_3b_5 + b_4b_5 - b_3b_6 - b_4b_6 + b_1b_7 - b_2b_7 + b_5b_7 - b_6b_7 + b_1b_8 - b_2b_8 + b_5b_8 - b_6b_8] \quad (2.8)$$

$$I_{1,5} = \frac{1}{12}[b_1b_5 + b_2b_6 + b_3b_7 + b_4b_8 + b_1b_1 + b_2b_2 + b_3b_3 + b_4b_4 + b_5b_5 + b_6b_6 + b_7b_7 + b_8b_8] \quad (2.9)$$

$$I_{1,6} = \frac{1}{24}[2b_1b_6 + 2b_2b_5 - 2b_3b_8 - 2b_4b_7 + b_1b_3 - b_2b_3 + b_1b_4 - b_2b_4 + b_3b_5 + b_4b_5 - b_3b_6 - b_4b_6 + b_1b_7 - b_2b_7 + b_5b_7 - b_6b_7 + b_1b_8 - b_2b_8 + b_5b_8 - b_6b_8]. \quad (2.10)$$

By examining the generating bond pairs for the second-order invariants in this larger cell, it is seen that two of the invariants, $I_{1,1}$ and $I_{1,2}$, have the same generating bond pairs as found in the second-order invariants for the primitive cell. The other two

Graph	b_1	b_2	b_3	b_4	b_5	b_6	b_7	b_8	$I_{1,1}$	$I_{1,2}$	$I_{1,5}$	$I_{1,6}$
a,b	1	1	1	-1	1	1	1	-1	1	$\frac{1}{3}$	$\frac{1}{3}$	-$\frac{1}{3}$
d	1	1	1	-1	-1	-1	-1	1	1	$\frac{1}{3}$	$\frac{2}{3}$	0
d	1	1	1	-1	-1	-1	1	-1	1	$\frac{1}{3}$	1	$\frac{1}{3}$

Table 2.1: Bond variables and second-order invariants for the three symmetry-distinct H-bond isomers of the $2\times1\times1$ unit cell of ice VII. The bond variables are assigned the value of ±1 depending on the orientation of the H-bond with respect to the canonical orientation illustrated in Fig. 2.4a. The last four columns indicate the values that the second-order graph invariants take when evaluated for each H-bond configuration.

invariants, $I_{1,5}$ and $I_{1,6}$, are generated by bond pairs that are farther apart than possible in the primitive cell. It should be noted that H-bonds throughout the entire lattice are generated by the action of the projection operator on a single bond. However, because of periodicity, the *value* of the bond variables can be expressed as the value of a bond within the unit cell. That is why the action of a projection operator containing an infinite number of translation elements gives rise to the finite expressions in Eqs. (2.7– 2.10) . The presence of $I_{1,1}$ and $I_{1,2}$ in this larger cell illustrates an important fact that invariants in small cells will also be found in larger cells. In addition, new invariants not possible in the small cell will be associated with the larger cell. From close inspection of the invariants, when evaluated for the H-bond configurations consistent with the ice rules, it is clear that some invariants are now linearly dependent on other invariants. For example, in Table 2.1 one can verify that

$$I_{1,2} = \frac{1}{3} I_{1,1} \tag{2.11}$$

$$\begin{aligned} I_{1,5} &= I_{1,6} + 2I_{1,2} \\ &= I_{1,6} + \frac{2}{3} I_{1,1}. \end{aligned} \tag{2.12}$$

Using $I_{1,1}$ and $I_{1,6}$ as independent variables, we can write down an expression relating scalar physical quantities to functions of the H-bond topology. Assuming a simple linear form, the energy of an H-bond isomer, as a function of the bond variables, can be written as

$$E(b_1, b_2, \ldots, b_8) = E_0 + \alpha I_{1,6}, \tag{2.13}$$

where E_o, a constant, and α can be determined by fitting to energies, obtained from either experiment or calculation, of H-bond configurations.

The idea of correlating the energy of an H-bond configuration of ice to features of the H-bond topology is not new, but has never been successfully implemented in the past. Long ago, Bjerrum [53] suggested that H-bonds in ice break into two categories, depending on whether the non-hydrogen bonded hydrogens are in a trans or cis arrangement, that is whether they fall on opposite or the same sides of the H-bond, as illustrated in Figs. 2.1 and 2.2. The presumed dominance of pairwise interactions has led to proposals that ice structures with the highest fraction of trans H-bonds are most stable [53], a notion that, if correct, would conflict with the proposed ferroelectric structure of ice XI, Fig. 2.2, in which three-quarters of the H-bonds are cis. Also, as described below, another conflicting result is that both the lowest and highest energy configurations for a $2 \times 2 \times 2$ unit cell of ice VII contain no H-bonds in the trans configuration. Nevertheless, the number of trans H-bonds is actually an example of an invariant and is useful for outlining our bootstrap strategy of invariants to larger unit cells. The cis/trans energy difference is a parameter that can be determined from small unit cells [54]. Electronic structure calculations could be performed on a small unit cell to calculate the cis/trans energy. Next, the cis/trans energy difference could be calculated for larger unit cells, for which these types of calculations are feasible, thus indicating whether convergence to the large cell limit has been reached. Then, the number of trans H-bonds could be used to extrapolate to even larger unit cells where it is not possible to do these calculations on the billions of possible H-bond arrangements needed for statistical simulations. If the relative number of cis and trans H-bonds did control the energy, then the energy of the billions of H-bond arrangements possible in a large cell would be known by counting the relative number of cis and trans H-bonds in each of those configurations. While, as argued above, the

number of cis/trans H-bonds is not sufficient to describe the H-bond energetics of ice, an analogous bootstrap strategy using graph invariants will prove successful.

Graph invariants provide a hierarchy of increasingly accurate approximations, with two independent routes for improving the description of scalar physical quantities. The first is determined by the number of bonds multiplied to generate an invariant, i.e. the order of the invariant polynomial in bond variables. Invariants can be constructed by projecting onto a single bond, a bond pair, a bond triplet, and so on corresponding to invariants of first, second, third and higher order, respectively. We have already demonstrated [51] how graphical techniques can be used to understand and predict physical properties of water clusters, finding that the expansion was well-converged at second order. As will be described below, the energy of H-bond isomers for various unit cells of ice is also well described using second-order invariants. The second manner by which the invariant approximation could be improved is by including invariants generated by bond pairs separated by greater distances. As described above, invariants for a large unit cell, when compared to invariants from a smaller unit cell, can be divided into two groups. Those invariants that were only present in the smaller unit cell and those invariants generated by bond pairs farther apart than possible in the smaller unit cell. Including invariants generated by bonds only possible in the larger unit cells would improve the approximation. As will be described below, acceptable convergence for the energy of H-bond isomers of ice only requires bond pairs that are nearest neighbors.

The proton order/disorder transitions in the various ice phases all share similar features. The underlying oxygen lattice is essentially unchanged between the disordered and ordered configurations. Hence, we neglect the small lattice parameter

changes as the temperature changes. As indicated above, experiments on samples of H_2O and D_2O indicate a difference in the transition temperature of a few degrees. In experiments on ice Ih, the proton ordering transition occurs at 72 K for H_2O and 76 K for D_2O, a difference of 4 K [17, 34]. A significant change in the transition temperature due to a change in mass is a sign that quantum effects are important. The small shift in the transition temperature indicates that quantum effects are negligible, thus we use classical statistical mechanics for our calculations.

If we stay away from extremely high pressure where the hydrogen bond becomes symmetrical, the potential energy surface for ice exhibits a number of deep minima, each corresponding to a different hydrogen bond topology. Working within the framework of classical statistical mechanics, the partition function can be written as a sum of contributions from each of the M symmetry-distinct local minima of the potential energy surface. [55–63] We have previously discussed [22, 51] how the partition function for ice can be written as a sum over M symmetry-distinct H-bond topologies

$$Q = \sum_{i=1}^{M} f_i e^{-\beta(E_i + A_{vib,i})} \,, \tag{2.14}$$

where f_i is the number of symmetry-related configurations which are represented by one symmetry-distinct configuration, E_i is the potential energy at the ith potential minimum, and $A_{vib,i}$ is the vibrational free energy associated with movement near that minimum. At sufficiently low temperature the classical procedure could be modified to incorporate some quantum effects, for example by calculating $A_{vib,i}$ quantum mechanically. However, the use of classical statistical mechanics seems warranted for H-bond order/disorder transitions in ice.

Each E_i and $A_{vib,i}$ in Eq. (2.14) corresponds to a local minimum of the potential surface defined by an H-bond topology. The graph invariants we have introduced

[19, 22, 51] provide a feasible way to circumvent the need to calculate all the E_i and $A_{vib,i}$ for the billions of hydrogen bond topologies found in a "simulation cell", a unit cell large enough to approximate the thermodynamic limit. Graph invariants link quantities like E_i and $A_{vib,i}$ to H-bond topology, and allow us to construct statistical models with a kind of bootstrap procedure. [22, 51] In all of our work on ice to date, we have obtained good agreement with available experiments assuming that $A_{vib,i}$, the vibrational free energy in each of the H-bond isomers, is approximately the same: $A_{vib,i} \approx \overline{A}_{vib}$. Then the problem reduces to estimating the energy E_i of each of the symmetry-distinct isomers. If the approximation $A_{vib,i} \approx \overline{A}_{vib}$ would break down, then an alternative would be to fit the $A_{vib,i}$ to invariants with an expression similar to the energy expansion in Eq. (2.15).

Assuming the simplest linear dependence[1], the energy of an H-bond isomer as a function of the bond variables is written as,

$$E(b_1, b_2, \ldots) = E_0 + \sum_r \alpha_r I_r + \sum_{rs} \alpha_{rs} I_{rs} + \ldots\ldots \ , \tag{2.15}$$

with the overall constant E_0 and the α-coefficients to be determined either by comparison with experiment, or as we do in this work, by first-principles calculations. For our bootstrap strategy, we first determine the graph invariants for a small unit cell of ice from which a training set of isomers is chosen for DFT calculations which will determine the coefficients in the energy expression Eq. (2.15). Next, the graph invariants for a larger unit cell are determined. Each successively larger cell contains invariants that were already present in the smaller cell as well as new invariants involving bond combinations that are farther apart than possible in the small unit cell.

[1]Including high order invariants could be regarded as implementing a more complicated functional form.

A handful of isomers is chosen from the larger cell, DFT calculations are performed, and invariant parameters are refit to the energy expression. Enlarging the unit cell is continued until the invariant parameters converge and new invariants become unimportant. The converged invariant parameters will then be used to evaluate the energy expression for the many H-bond isomers of a large simulation cell to generate statistical averages. Our results indicate there are other important features, besides cis and trans H-bonds, which are required to appropriately link scalar physical properties to H-bond topology in ice. The use of graph invariants provides a systematic means to generate the full set of topological parameters, in the form of invariant polynomials of bond variables b_r, and organizing them in a hierarchy of increasingly accurate approximations [22, 51]. In this work we only retain the leading order, that is second-order invariants, which will be seen to provide an accurate description of the H-bond energetics of larger ice unit cells.

2.3 Metropolis Monte Carlo Simulations of Ice

Rather than introducing possible uncertainty associated with further approximations, we obtained an essentially exact numerical solution for the thermal behavior governed by the H-bond Hamiltonian using the standard Metropolis Monte Carlo algorithm(e.g. Ref. [64]). Metropolis Monte Carlo simulations were typically performed on simulation cells containing thousands of water molecules. A series of simulations were performed for both increasing and decreasing temperatures. The initial structure for the increasing temperature simulations was that of the ground state H-bond configuration. To date, this configuration agreed with the experimental structure for all cases where experimental data was available. A highly disordered configuration

obtained from simulation at an extremely large temperature ($\sim 10^7$ K) was used to initialize the sequence of simulations descending in temperature. The final configuration for each simulation was always the initial configuration for the next simulation.

When simulating our model at low temperatures, where acceptance of trial moves is rare, we found that care in the choice of random number generator was required, and that some random number generators produced artificial periodic excitations out of the ground state with a period lasting thousands of Monte Carlo passes. Since this behavior only occurred when excitations were rare, it actually had no effect on the statistical averages reported below. Nevertheless, we took care to find simulation conditions free of the artificial periodic behavior. We found that the "Mersenne Twister" generator developed by Matsumoto and Nishimura [65] was not susceptible to the spurious behavior.

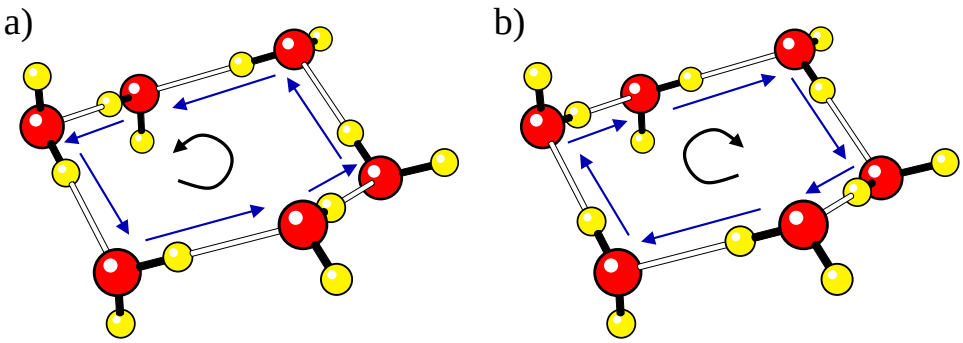

Figure 2.5: Example of flipping a loop of H-bonds which point in similar directions to generate trial configurations that are allowed by ice rules.

The only non-standard feature of our Monte Carlo algorithm is the generation of the trial moves, since our trial rearrangements of H-bonds must not violate the

ice rules. We use the algorithm invented by Rahman and Stillinger [66] for sampling H-bond configurations in ice, which randomly identifies closed loops of H-bonds. Flipping the entire loop of H-bonds, as shown in Fig. 2.5, will preserve the number of outgoing and incoming bonds at each oxygen atom and will not "break" any water molecules, thereby preserving the ice rules. Recently, Rick and Haymet have generalized the Rahman-Stillinger idea to do off-lattice simulations of ice [67]. In their paper, one can find references to work where the ergodic nature of the Rahman-Stillinger loop algorithm was proved. In an approximation where the total dipole is a sum of bond dipoles, it is easily seen that closed loops do not change the total dipole moment of the system. However, as Rahman and Stillinger noted, loops that begin in one periodic simulation cell and terminate in another cell will change the dipole moment. We allow both types of moves because we want to sample all H-bond configurations, including ferroelectric and anti-ferroelectric configurations, and allow exact statistical simulations to identify the equilibrium properties of the system.

The transition temperature is calculated as the point of equal free energy($\Delta A = 0$ in Eq. (2.16)) between the two phases as determined by thermodynamic integration of the low-temperature proton-ordered phase from 0 K and the high-temperature proton-disordered phase from infinite temperature.

$$\Delta A(T) = (E_H(T) - E_L(T)) - T(S_H(T) - S_L(T)) \tag{2.16}$$

$$S_H(T) = S(\infty) - \int_T^\infty dT' \frac{C_V}{T'} \tag{2.17}$$

$$S_L(T) = \int_0^T dT' \frac{C_V}{T'} \tag{2.18}$$

Since we neglect the effect of what is known to be a small change in the lattice constants with temperature, we do not include a pressure-volume term in the free

energy. The constant, $S(\infty)$, in Eq. (2.17) for the entropy of the high temperature phase is the configurational entropy for a fully disordered ice phase subject to the ice rules which we take from the work of Nagle: $S(\infty) = Nk_B \ln(1.5069)$ [10].

2.4 The VII/VIII Proton Ordering Transition

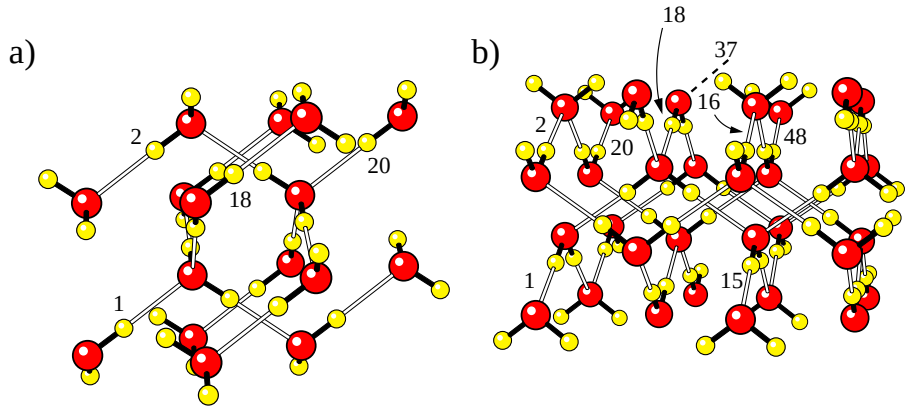

Figure 2.6: a) An H-bond isomer of a 16-water unit cell of ice VII measuring 2 primitive unit cells on each side. Bonds representative of the three 2nd-order graph invariants used to fit the DFT energies are shown, as further described in Table 2.2. b) The ground-state H-bond isomer of a 32-water unit cell of ice VII measuring $2\sqrt{2}\times 2\sqrt{2}\times 2$ primitive cells on each side corresponding to the experimentally determined ice VIII structure. Bond pairs representative of the 2nd-order graph invariants, including bond pairs not possible in the smaller 16-water unit cell, used to fit the DFT energies are shown. Bond 37 connects to a water molecule in an adjoining cell.

Our study of proton ordering phase transitions in ice begins with the ice VII/VIII transition. The smallest unit cell we examined was a cubic 16-water unit cell of ice VII, 2 primitive unit cells on each side as shown in Fig. 2.6. The lattice constant used in the following calculations was $a = 3.337$ Å, as determined by diffraction studies at 1.1 GPa and 263 K [44].

All first-order invariants for the $2 \times 2 \times 2$ cell were identically zero for reasons described in section 2.2. There are eight second-order graph invariants for this cell, which, when evaluated for the 52, symmetry-distinct H-bond isomers possible in this unit cell, enumerated using previously described methods [50, 51, 68], could be sorted into two groups. The first group contained two invariants which evaluated to the same constant for all H-bond configurations and the second group consisted of the remaining six invariants. The two invariants in the first group, $I_{1,1}$ and $I_{1,5}$, were generated by bond pairs that had at least one common vertex. $I_{1,1}$ was generated from $\hat{G}(b_r b_r)$ and $I_{1,5}$ is equivalent to invariant $I_{1,2}$ found in the smaller unit cells discussed in section 2.2. Due to the periodicity constraints and the ice rules, invariants may become linearly dependent on other invariants when evaluated for H-bond isomers. The second group contained three linearly independent invariants while the first group contained only one invariant. We will speak of "eliminating linearly dependent invariants" when, more precisely, we are eliminating invariants which are dependent on others over the restricted set of configurations allowed by the ice rules. Since it is arbitrary which invariants are chosen to be the linearly independent set of invariants, we selected invariants based on geometrical features of the generating bond pairs such as whether the generating bond pairs belong to the same sub-lattice and minimum distance between bond pairs. Geometrical features of the invariants included in Eq. (2.15) are described in Fig. 2.6 and at the top of Table 2.2.

Periodic DFT calculations were performed on all 52 enumerated H-bond configurations using the Car-Parrinello Molecular Dynamics(CPMD) [69–71] program with the Becke-Lee-Yang-Parr gradient correction [72, 73] to the local density approximation, Troullier-Martins norm-conserving pseudopotentials [74], and a planewave cutoff of

70 Ry. The Brillouin zone sampling was restricted to the $\Gamma-$point. The dependence of energy on H-bond topology was well captured by an expression, Eq. (2.15), with second-order invariants as the leading term, as shown in Fig. 2.7a. The DFT energy is plotted against a linear fit to the 52 energies using the first three invariants listed in Table 2.2 plus an overall constant. In Fig. 2.7, perfect agreement is indicated when points lie on the diagonal line.

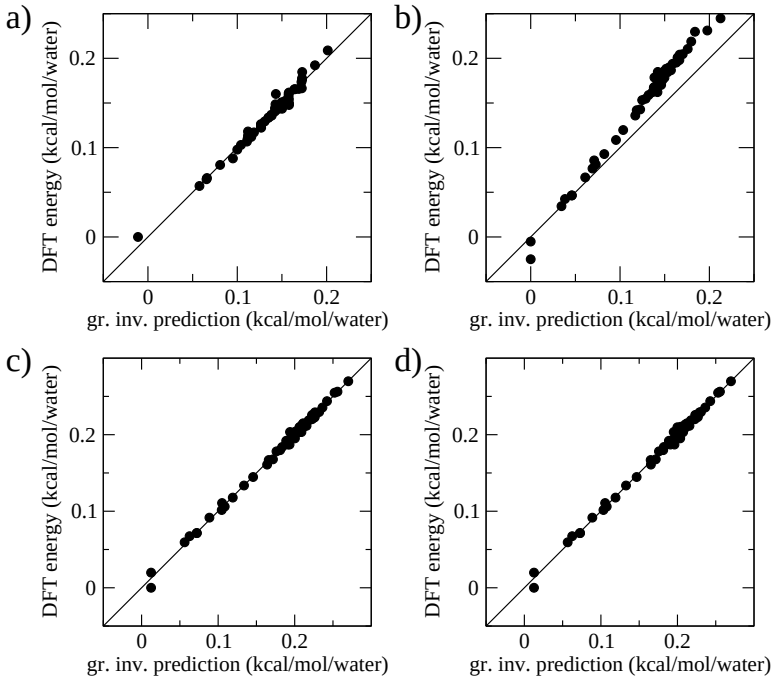

Figure 2.7: a) Graph invariant fit to the energies of the 52 H-bond isomers of a 16-water unit cell of ice VII. b) Calculated DFT energy of H-bond isomers of a 32-water ice VII cell plotted against energies predicted from graph-invariant parameters derived from the 16-water cell. c) Graph invariant fit, using second-order invariants whose generating bond pairs are farther apart than possible in the smaller 16-water unit cell, to the energies of the H-bond configurations for the 32-water unit cell. d) Same as plot (c) except only invariants whose generating bond pairs exist in the smaller 16-water unit cell were fit to the energies. A line of slope unity is shown to indicate where points would lie for perfect agreement. Invariant coefficients for each of the three fits are listed in Table 2.2.

Next, calculations were performed on a larger ice VII unit cell, measuring $2\sqrt{2} \times 2\sqrt{2} \times 2$ primitive cells on each side. As discussed above, in section 2.2, all invariants from the smaller cell were also found in the larger unit cell. All first-order invariants were algebraically zero. There were ten additional second-order graph invariants generated from bond pairs that were farther apart than possible in the smaller 16-water unit cell. DFT calculations were performed on 50 H-bond isomers chosen "semi-randomly" from the 35806 symmetry-distinct H-bond configurations possible in this unit cell [50, 51, 68]. From a prediction based on the graph-invariant parameters fit to the $2 \times 2 \times 2$ cell, we selected isomers that would cover the entire energy range, plus other isomers that would test whether the new invariants that appear for the larger $2\sqrt{2}\times2\sqrt{2}\times2$ cell are actually needed to fit the energy of the isomers for the larger cell. The energies of the 32-water unit cells are well predicted using invariant parameters obtained from calculations on the 16-water cell, shown in Fig. 2.7b. However, there is a small systematic discrepancy in which the invariant prediction overestimates the energy differences in the 32-water cell. This discrepancy is actually not a consequence of requiring more invariant parameters for the larger cell but instead arises because the conditions under which the calculation is performed changes with cell size. In the larger cell, there is more freedom for configurational relaxation and greater effective $k-$point sampling at the $\Gamma-$point. Thus, the small discrepancy is actually an indication that we are nearing convergence of the graph-invariant parameters with respect to both unit cell size and $k-$point sampling.

Of the 18 second-order invariants for the $2\sqrt{2} \times 2\sqrt{2} \times 2$ cell, eight invariants were linearly independent when evaluated for all H-bond configurations. A fit of the DFT energies incorporating invariants whose generating bond pairs were farther apart

invariant	generating bond pair	distance(Å)	same lattice?	16-water (inv. 1−3)	32-water (inv. 1−7)	32-water (inv. 1−3)
1	1,20	2.89	N	0.0155118	0.0243047	0.0192577
2	1,18	2.89	Y	−0.0471626	−0.0657520	−0.0709555
3	1,2	2.89	N	0.0907482	0.1009400	0.1093980
4	1,48	5.53	N	–	0.01063060	–
5	1,16	5.53	N	–	−0.00705523	–
6	1,15	4.72	Y	–	−0.00248413	–
7	1,37	4.72	Y	–	0.01210390	–

Table 2.2: Geometrical features and contribution to the description of the energy of H-bond isomers of the second-order graph invariants. Invariants 4−7 do not appear in the 16-water, $2 \times 2 \times 2$ unit cell of ice VII. The indices of the generating bond pair refer to Fig. 2.6. The distance associated with each bond pair is the distance between the closest vertices from each bond in an ideal structure before geometry optimization. The last three columns give the fitting coefficients for each of the invariants as used in Eq. (2.15) for the energy in units of kcal mol^{-1} per water.

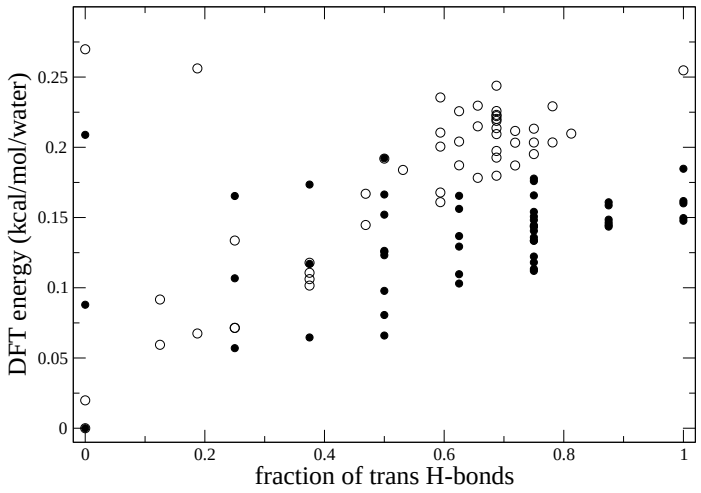

Figure 2.8: Relative DFT energy of H-bond isomers of a 16-water(●) and 32-water(○) unit cell of ice VII plotted against fraction of trans H-bonds for each isomer. The lowest and highest energy isomers for both unit cells contain no H-bonds in the trans configuration thus indicating that features of the H-bond topologies other than cis/trans H-bonds are important if physical properties are to be correctly described.

than possible in the smaller 16-water unit cell (Fig. 2.7c) yielded a fit just as good in quality as that obtained from only using invariants whose generating bond pairs existed in the smaller cell (Fig. 2.7d). We conclude that the energy of the H-bond isomers is accurately described by invariants whose generating bond pair contains vertices that are nearest neighbors. The energy plotted as a function of the percent of trans H-bonds is shown in Fig. 2.8. The fraction of trans H-bonds can be expressed as a linear combination of graph invariants,

$$\% \text{ trans H-bonds} = -\frac{3}{4}\hat{I}_{1,18} + \frac{3}{4}, \tag{2.19}$$

where $\hat{I}_{1,18}$ is one of the invariants, Table 2.2 and Fig. 2.6, used to fit the energies. For both unit cells, the ground state and highest energy configurations contain no H-bonds that are trans. If the relative number of trans H-bonds was the only feature of

the H-bond topology used to describe the energetics, those configurations would then be degenerate. Clearly, it is evident that additional features of the H-bond topology, exhibited by the graph invariants, are necessary to accurately describe the relative energetics of H-bond isomers of ice.

Using the improved invariant parameters and Eq. (2.15), we have a Hamiltonian describing the energy differences due to fluctuating H-bonds in a large simulation cell. Metropolis Monte Carlo simulations were performed on a simulation cell measuring eight primitive cells on each side containing 1024 water molecules. A series of simulations were performed for both increasing and decreasing temperatures. The initial structure for the increasing temperature simulations was that of the experimentally determined ice VIII structure.

The Monte Carlo simulations yield a prediction of a first-order phase transition near 228 K with significant hysteresis, as shown in Fig. 2.9a. The transition temperature is calculated as the point of equal free energy($\Delta A = 0$ in Eq. (2.16)) between the two phases as determined by thermodynamic integration of the low-temperature proton-ordered phase from 0 K and the high-temperature proton-disordered phase from infinite temperature. Entropy as a function of temperature is plotted in Fig. 2.9b. With decreasing temperature, 7% of the ideal entropy for a fully disordered ice phase is lost before the transition. The calculated entropy at the transition, 228 K, is 91% of the ideal configurational entropy associated with H-bond disordering compared with experimentally reported values of 83% for H_2O and 91% for D_2O [47].

Partial disordering below the transition is also observed in a plot of $\langle \mathbf{M}_\mathrm{a}.\mathbf{M}_\mathrm{b} \rangle$ as a function of temperature, as shown in Fig. 2.9c. $\mathbf{M}_\mathrm{a}$ and $\mathbf{M}_\mathrm{b}$ are the dipole moments, calculated using a bond-dipole approximation, for each of the two independent

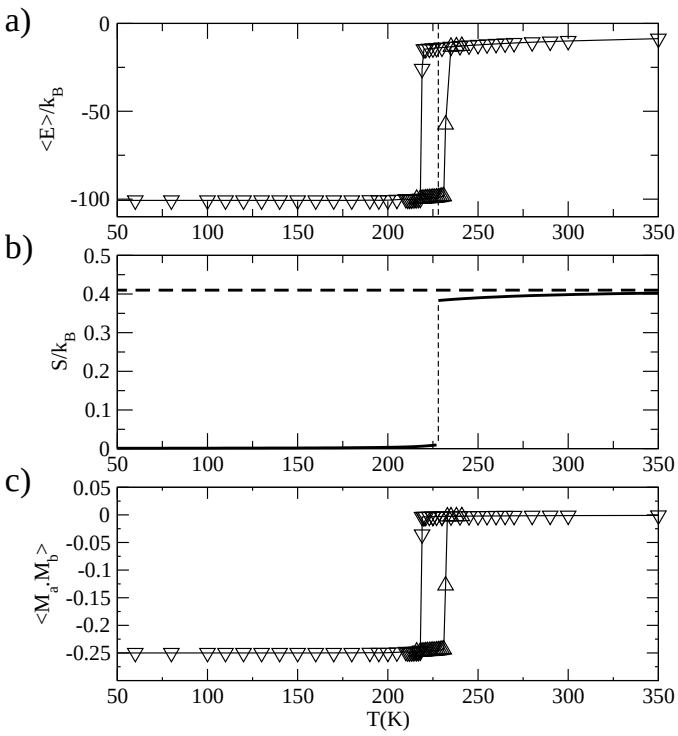

Figure 2.9: a) Average energy plotted as a function of temperature from Metropolis Monte Carlo simulations for a large simulation cell of ice VII/VIII. Data is presented for series of Metropolis Monte Carlo runs ascending($\triangle$) and descending(∇) in temperature. The vertical line is located at the calculated transition temperature near 228 K. b) Entropy plotted as a function of temperature. The horizontal line is the Pauling entropy for a fully disordered ice lattice subject to the ice rules. c) Degree of anti-ferroelectric ordering of the ice VII sub-lattices as a function of temperature. M_a and M_b are the total dipoles, in units of bond dipoles, for the two independent sub-lattices.

sub-lattices and $\langle \dots \rangle$ is an ensemble average. $\mathbf{M}_a$ and $\mathbf{M}_b$ are each normalized to $N\mu_{H_2O}$, where μ_{H_2O} is the dipole moment magnitude of one water molecule and N is the total number of waters in one system. At high temperatures, $\langle \mathbf{M}_a.\mathbf{M}_b \rangle$ is zero corresponding to fully disordered ice VII. At low temperatures, anti-ferroelectrically ordered ice VIII is the stable phase with both sub-lattices oriented oppositely so that

$$\langle \mathbf{M}_a.\mathbf{M}_b \rangle = \frac{(-\frac{N}{2}\mu_{H_2O}).(\frac{N}{2}\mu_{H_2O})}{|N\mu_{H_2O}|^2} = -\frac{1}{4}. \tag{2.20}$$

Fig. 2.9c indicates that the degree of pre-transitional alignment and post-transitional disorder in $\langle \mathbf{M}_a . \mathbf{M}_b \rangle$ is small.

Despite the challenge posed by small energy variation among H-bond isomers, our results qualitatively match the observed features of the ice VII/VIII phase transition in several respects: 1) the calculated ground state is the known ice VIII antiferroelectric structure [68], 2) the transition temperature, 228 K, is similar to the experimental transition point measured in the range 263−274 K [44, 47], 3) the detectable partial ordering above the transition and partial disordering below the transition, as measured by the entropy at the transition, is in agreement with experiment.

2.5 The Ih/XI Proton Ordering Transition

Having calibrated our methods with the ice VII/VIII transition, we now turn to ice Ih/XI, which is not as well characterized experimentally. Given the degree of controversy surrounding the Ih/XI transition and the small energy differences, we attempted to gauge how sensitive the calculated energy differences were to the level of theoretical treatment. We performed DFT calculations for ice Ih using three different combinations of density functionals and basis sets for two smaller unit cells of ice Ih, an orthorhombic unit cell containing eight water molecules [54] and a hexagonal cell with twelve waters. The lattice constants for the hexagonal unit cell were $a = 7.7808$ and $c = 7.3358$ Å and those for the orthorhombic unit cell were $a = 4.4922$, $b = 7.7808$, and $c = 7.3358$ Å. [54] The number of symmetry-distinct H-bond isomers consistent with the ice rules and lattice periodicity is 16 and 14 for the orthorhombic and hexagonal unit cells respectively [22].

Three separate methods of calculation were employed to check the consistency of DFT in describing the energetics of H-bond isomers. The CPMD [69–71] program was used as previously described. The BLYP [72,73] functional using numerical basis sets was implemented within the DMol program [75]. The CASTEP program [76] was used with the PW91 functional [77–79] and a plane wave basis. The different density functionals, basis sets, and programs agree quite well when applied to starting configurations(Fig. 2.10 for the 16-water orthorhombic unit cell and Fig. 2.11 for the 12-water hexagonal unit cell), for which the cell dimensions and molecular geometries for each isomer are exactly the same. Moreover, each method yields the $Cmc2_1$ structure as the lowest-energy isomer. The isomers are arranged in Figs. 2.10 and 2.11 in order of increasing fraction of trans H-bonds and it is once again apparent that this feature does not predict their relative energies. We can express the fraction of trans H-bonds as a linear combination of the same three graph invariants used to fit the energies,

$$\% \text{ trans H-bonds} = -\frac{3}{4}\hat{I}_{4,9} + \frac{3}{8}\hat{I}_{1,6} - \frac{3}{16}\hat{I}_{1,3} + \frac{11}{16}. \tag{2.21}$$

Comparing these coefficients to those listed for the energies in Table 2.3, we can see that the only difference, apart from a scaling factor, is the sign of the coefficient for invariant $\hat{I}_{1,3}$.

After comparing energies from different methods calculated for exactly the same geometries, we subsequently optimized geometries within the capabilities of each method. For two of the methods, CPMD and DMol, the atomic positions were optimized with cell dimensions fixed. Those two cases are in very good agreement. In the third method, CASTEP, the cell dimensions were optimized as well and, as would be expected, this case deviates further from the other two. As shown in Figs. 2.10

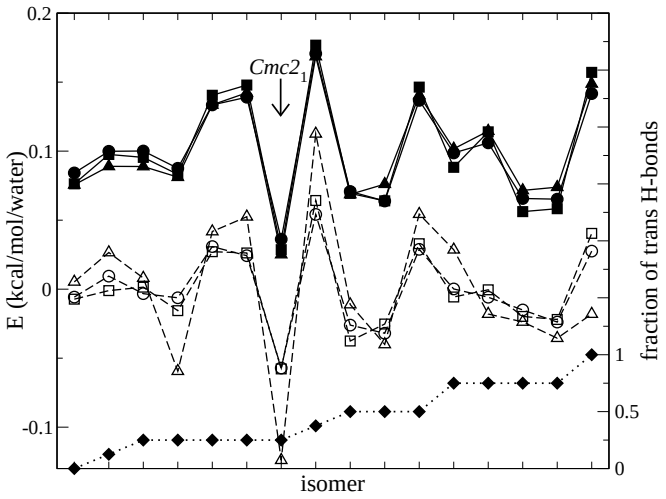

Figure 2.10: Relative energy of H-bond isomers calculated by periodic DFT methods for 16 isomers of an 8-water orthorhombic unit cell listed in order of increasing fraction of trans H-bonds. The lowest graph (dotted lines) gives the fraction of trans H-bonds associated with each isomer. The energy of the H-bond isomers were calculated using the programs CPMD(●,○), DMol(■,□), and CASTEP(▲,△). Solid lines: energy of H-bond isomers before geometry optimization. Dashed lines: energies after optimization of the molecular coordinates, and for the CASTEP results cell dimensions as well. The 6 energy data sets, optimized and unoptimized, are plotted with their average taken as the zero of energy to facilitate comparison of the relative energies of the isomers. For clarity, the $Cmc2_1$ isomer is noted and the unoptimized data sets are shifted by 0.12 kcal mol^{-1}.

and 2.11, the overall trends do not depend on the choice of density functional, or the optimization method. The lowest-energy isomer is the $Cmc2_1$ ferroelectric structure in each case. Similar comparisons from calculations using empirical water potentials indicated that the relative energetics of H-bond isomers differed by an order of magnitude among the models and none had identified the $Cmc2_1$ structure as the ground state [21]. While many commonly used empirical potentials do not give a reliable description of H-bond energetics in ice, DFT calculations provide a robust description.

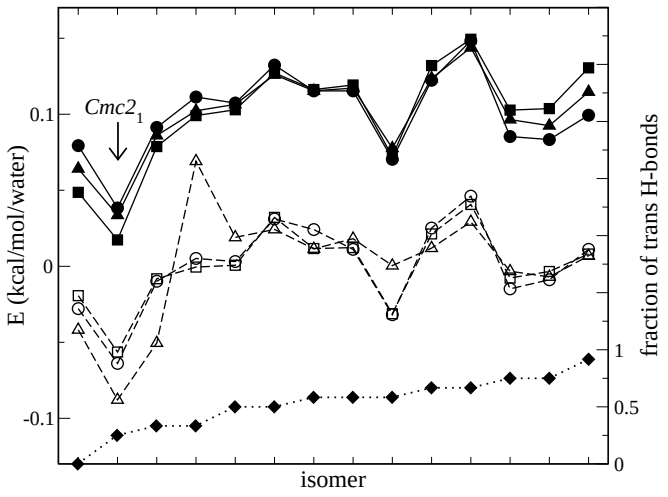

Figure 2.11: Relative energy of H-bond isomers calculated by periodic DFT methods for 14 isomers of a 12-water hexagonal unit cell listed in order of increasing fraction of trans H-bonds. The lowest graph (dotted lines) gives the fraction of trans H-bonds associated with each isomer. The energy of the H-bond isomers were calculated using the programs CPMD(●,○), DMol(■,□), and CASTEP(▲,△). Solid lines: energy of H-bond isomers before geometry optimization. Dashed lines: energies after optimization of the molecular coordinates, and for the CASTEP results cell dimensions as well. The 6 energy data sets, optimized and unoptimized, are plotted with their average taken as the zero of energy to facilitate comparison of the relative energies of the isomers. For clarity, the $Cmc2_1$ isomer is noted and the unoptimized data sets are shifted by 0.12 kcal mol^{-1}.

As discussed above, the *ab* puckered sheets of the $Cmc2_1$ structure have a net polarization. The polarization alternates from sheet to sheet making the ice XI structure anti-ferroelectric in the *ab* direction. Thus, the puckered sheets are slightly displaced in the direction of the polarization, as shown in Fig. 2.13, by a magnitude of $\epsilon/2$, where ϵ is the relative displacement of two adjacent layers. Using the optimized geometry of the 12-water $Cmc2_1$ structure, obtained using the CPMD [69–71] program as described above, we calculated the distance between the center of mass

for each of the *ab* layers. The calculated value, $\epsilon = 0.11$ Å, is in agreement with the experimentally determined value, $\epsilon = 0.12$ Å [2].

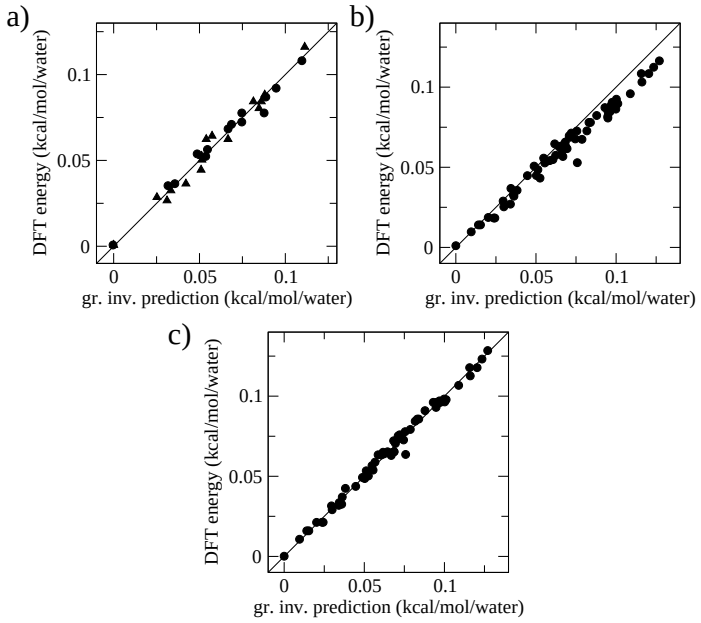

Figure 2.12: a) Graph invariant fit to the energies of the 14 H-bond isomers of a 12-water hexagonal(●) unit cell and the 16 H-bond isomers of an 8-water orthorhombic(▲) unit cell of ice Ih. b) Calculated DFT energy of H-bond isomers of a 48-water hexagonal ice Ih unit cell plotted against energies predicted from graph-invariant parameters derived from the small unit cells. c) Graph-invariant fit to the energies of the 63 "semi-randomly" chosen H-bond isomers of a 48-water hexagonal unit cell of ice Ih. A line of slope unity is shown to indicate where points would lie for perfect agreement.

Similar to ice VII, all first-order invariants for both the 12-water hexagonal and 8-water orthorhombic unit cell were identically zero. Application of the projection operator for the totally symmetric representation on bond pairs in the 12-water hexagonal unit cell resulted in thirteen second-order invariants for which five were linearly independent when evaluated for the enumerated H-bond configurations. Periodic DFT

calculations using the CPMD [69–71] program, as described above, were performed on all H-bond isomers. A good description of the energetics was obtainable using only three invariant parameters, shown in Table 2.3. The invariants listed in Table 2.3 represent a set of linearly independent invariants from among those for which the generating bond pairs are no further apart than one nearest-neighbor distance. Since linear dependencies exist among the invariants when evaluated for configurations that satisfy the ice rules, the choice of a set of independent parameters is arbitrary. Even though Table 2.3 only includes second-order invariants generated from pairs in the *ab* puckered sheets, the configuration of H-bonds in the $c-$direction is effectively included because these invariants are linearly dependent on those listed in Table 2.3.

In the case of the 8-water orthorhombic unit cell, sixteen second-order invariants exist for which six were linearly independent when evaluated for all enumerated H-bond configurations. The energy of the H-bond isomers was well described using invariants generated by the same three bond pairs as those that generated the invariants used to predict the energy of the 12-water hexagonal unit cell, Table 2.3. The generating bond pairs for the invariants used to describe the energies of H-bond isomers in both unit cells are shown in Fig. 2.13. A combined fit of the DFT energies for both types of unit cells, hexagonal and orthorhombic, plotted against the predicted values using three invariant parameters is shown in Fig. 2.12.

Next, periodic DFT calculations were performed on a larger hexagonal unit cell, containing 48 waters, measuring $2 \times 2 \times 1$ primitive cells on each side. In order to evaluate the convergence of the invariants achieved in the small unit cells, the predicted energies of 63 H-bond configurations, chosen from the 8360361 symmetry-distinct H-bond isomers possible in the larger unit cell [50, 51, 68], were compared to

invariant	generating bond pair	bond type	12-water hex-$(1 \times 1 \times 1)$	16-water orth-$(2 \times 1 \times 1)$	12 & 16-water combined fit	48-water hex-$(2 \times 2 \times 1)$
1	1,3	ab,ab	0.0288485	0.0249965	0.0267952	0.0250812
2	4,9	ab,ab	−0.0789488	−0.0775161	−0.0777339	−0.0952566
3	1,6	ab,ab	0.0346155	0.0416369	0.0359921	0.0481123

Table 2.3: Geometrical features and contribution to the description of the energy of H-bond isomers of the second-order graph invariants. The indices of the generating bond pair refer to the H-bonds shown in Fig. 2.13. The H-bonds can be described as either lying parallel, $c-$bonds, or perpendicular, $ab-$bonds, to the $c-$axis. The last four columns give the fitting coefficients for each of the invariants as used in Eq. (2.15) for the energy in units of kcal mol^{-1} per water.

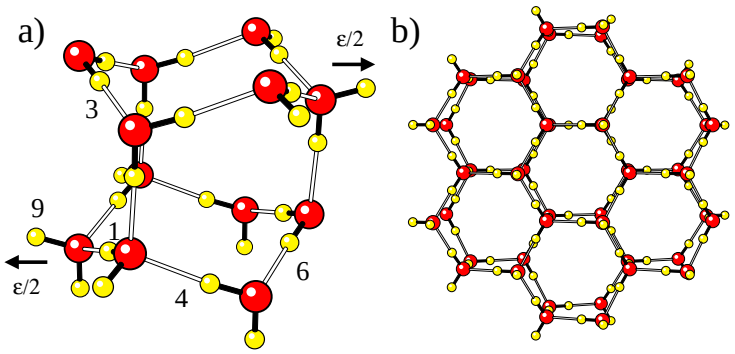

Figure 2.13: a) An H-bond isomer of a 12-water primitive unit cell of ice Ih. Bonds representative of the three 2nd-order graph invariants used to fit the DFT energies are shown, as further described in Table 2.3. All bonds used to generate second-order invariants, used to describe energy differences for H-bond fluctuations in a large simulation cell, lie perpendicular to the $c-$axis and are referred to as $ab-$bonds. b) An H-bond isomer of a 48-water unit cell of ice Ih measuring $2 \times 2 \times 1$ primitive cells on each side. Both H-bond isomers shown are the lowest-energy isomer for each unit cell in agreement with the experimentally proposed ferroelectric, space group $Cmc2_1$, ice XI structure. Arrows indicate direction of the relative displacement, $\epsilon/2$, of the ab layers which are oppositely polarized.

the actual DFT energy, shown in Fig. 2.12. The 63 configurations for the $2 \times 2 \times 1$ cell were "semi-randomly" chosen, as described in section 2.4, to provide coverage of the entire range of energies and test whether new invariants arising from the larger cell were required to describe the energetics. The prediction from the small cells does a good job at predicting the energies of the large-cell isomers, even better than the small cell predictions of ice VII described above. Again, the small deviation can be accounted for by the additional freedom for geometrical relaxation and more effective $k-$point sampling at the $\Gamma-$point in the larger cell. As with ice VII, we only require graph invariants generated by nearest-neighbor bond pairs to describe the energy differences due to the numerous H-bond configurations in a large simulation

cell. By refitting the invariant coefficients to the large cell energies, we are able to, with Eq. (2.15), calculate the energy differences arising from the various H-bond configurations in Metropolis Monte Carlo simulations of a large ice Ih system.

Monte Carlo simulations of ice Ih were performed, following the same procedure for that of the ice VII simulations, using an orthorhombic cell measuring $7\times4\times4$ primitive cells on each side containing 896 water molecules. Average energy as a function of temperature indicates that a first-order transition to the low-temperature proton-ordered structure occurs near 98 K. The structure of the low-temperature phase is that of the experimentally proposed ferroelectric $Cmc2_1$ structure, shown in Fig. 2.14. The system exhibits negligible hysteresis, unlike that observed in the VII/VIII transition. The entropy as a function of temperature, shown in Fig. 2.14, indicates that as ice Ih is cooled, the system loses 11% of it configurational entropy before the transition, in agreement with pre-transitional effects seen calorimetrically [17] and in diffraction studies [5]. Only 1% of the configurational entropy for an ideal ice phase is lost below the transition resulting in 88% of the ideal entropy lost at the transition.

2.6 Discussion

In this work, we have presented the results of statistical simulations used to predict the proton order/disorder phase transition for two different ice systems, ices Ih/XI and VII/VIII. Using an analytic technique, graph invariants, we have illustrated how features of the H-bond topology can be linked to scalar physical properties, in this case energy, and used to extrapolate data taken from calculations on small units cells to calculate properties for simulation cells large enough to approach the thermodynamic

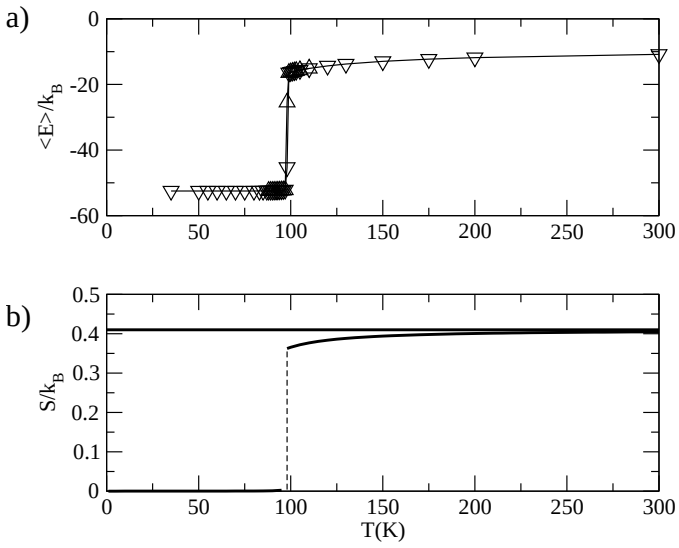

Figure 2.14: a) Average energy plotted as a function of temperature from Metropolis Monte Carlo simulations of a large simulation cell of ice Ih. Data is presented for series of Metropolis Monte Carlo runs ascending($\triangle$) and descending($\triangledown$) in temperature. b) Entropy plotted as a function of temperature. The horizontal line is the Pauling entropy for a fully disordered ice lattice.

limit. Our results indicate that invariants generated by pairs of bonds, whose closest-lying vertices are nearest neighbors, are appropriate to describing the energies of the numerous H-bond isomers possible in a large unit cell.

The energy differences between the H-bond isomers in proton-disordered phases of ice are quite small, indicating that careful checking of our theoretical methods is needed. We have shown that DFT methods are capable of describing the subtle energy differences between the various H-bond isomers possible in a given unit cell. We first validated our methods by predicting the proton ordering phase transition for the ice VII/VIII system. Our results yielded a transition to H-bond ordered ice VIII near 228 K which is in qualitative agreement with the experimental transition temperatures 263−274 K [44, 47]. We then reported on results from simulations of the ice Ih/XI

phase which predicted that a transition should occur near 98 K to the proposed ground state. This is in good agreement with the observed transition at 72 K(76 K) for samples of $H_2O(D_2O)$. The functionals and optimization methods explored in this work correctly identified the ice VIII ground state from among the configurations possible in ice VII. The fact that our calculations yield a transition temperature close to the experimental results indicates that the energy spectrum of the H-bond isomers, not just the ground state, is described by our methods. The quality of the results for ice VII/VIII provides some calibration of our calculations for ice Ih/XI. In this case, three different combinations of electronic density functionals, basis sets, and optimization methods yielded similar energy spectra of the isomers. Our results for ice Ih/XI provide support for the interpretation of experimental observations as a transition to a ferroelectric $Cmc2_1$ structure. However, better experimental characterization of the low-temperature phase and close comparison with theory are certainly needed in the future.

CHAPTER 3

PREDICTION OF A PHASE TRANSITION TO A HYDROGEN BOND ORDERED FORM OF ICE VI

3.1 Introduction

In the phase diagram of water, the liquid phase is surrounded by a series of H-bond-disordered ice phases. Ice-Ih (ordinary hexagonal ice) is the H-bond-disordered solid phase adjacent to the liquid at low pressures. Then, in order of appearance with increasing pressure, ice-III, ice V, ice VI and then ice VII are adjacent to the liquid phase. Several of these phases give way to an H-bond-ordered version of themselves at lower temperatures. Ice Ih, when suitably doped with hydroxide, transforms to what is thought to be a ferroelectric phase, ice XI, near 72 K for H_2O and 76 K for D_2O. [17, 34, 80–82] The oxygen atom positions in ice XI are very close to those of ice-Ih, [2–5] and the transition principally involves selection of one particular H-bond arrangement in the low-temperature phase. Ice III, when cooled at about 1 K per minute or faster, transforms to a metastable H-bond-ordered version known as ice-IX. [9,14,83–85] In the 2.1−12 GPa range, the H-bond-ordered form of ice VII, known as ice VIII, appears near 0°C. [44, 47]

At low temperature, the H-bond-ordered form of ice VI has not been clearly identified, although some experiments, as described below, give some preliminary

indications of low-temperature, fully ordered phases. The purpose of this work is to predict the structure of a low-temperature, H-bond-ordered form of ice VI, and the temperature at which the transformation should be found. In accordance with past practice, this new phase should be granted a roman numeral of its own, but for now, following Kamb, [86, 87] we use primes to distinguish the H-bond-ordered phase and call this phase ice VI′.[2] Our predictions are based on a method we have developed that enables us to use data from electronic structure calculations from small unit cells to parametrize a Hamiltonian for a cell large enough for statistical simulations. [19, 22, 51] The energy difference between various H-bond isomers of ice is known to be rather small. [1] However, we have shown in chapter 2 that periodic DFT successfully predicts the low-temperature structure and location of the phase transition for ice-Ih/XI and ice VII/VIII. [19]

There is partial experimental evidence for the transformation of ice VI to an H-bond-ordered form, but complete diffraction data that would identify the H-bond-ordered version of ice VI is not available. In 1965, Kamb noticed an X-ray reflection at 77 K that was incompatible with the $P4_2/nmc$ space group of ice VI and could have signaled the formation of an H-bond-ordered version of ice VI. [86] Later, he reported neutron diffraction data taken at 100 K on a sample previously equilibrated at high pressure and 77 K which indicated anti-ferroelectric ordering. [87] In 1976, Johari and Whalley predicted an ordering transition at 47 K to a ferroelectrically ordered state in ice VI based on observed Curie-Weiss behavior of the low-frequency dielectric constant. [88] Later, they concluded that the high frequency permittivity of ice VI at 0.9 GPa indicated that a very slow phase transition occurs in the temperature

[2]Actually, Kamb uses VI′ to indicate a partially ordered phase, and VI″ to denote the fully ordered form of ice VI.

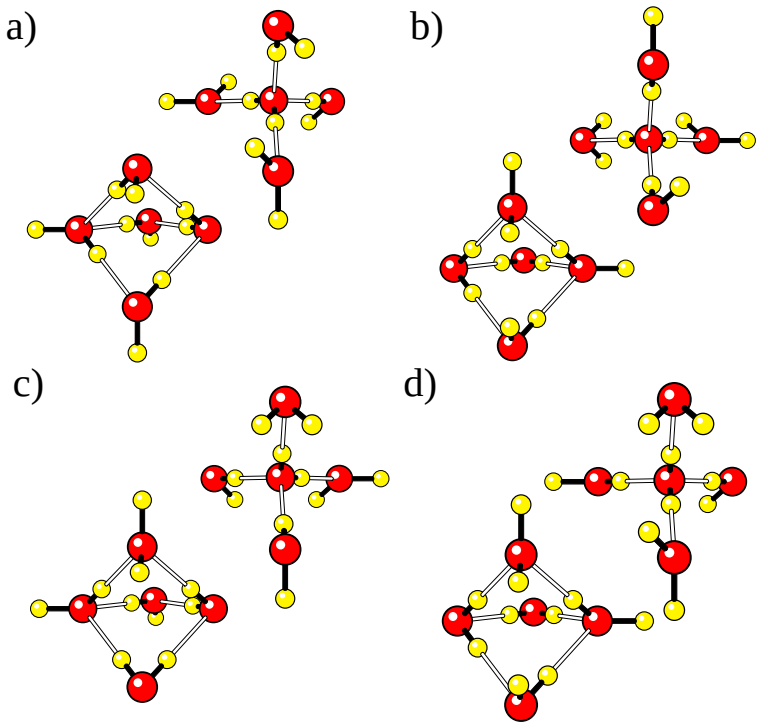

Figure 3.1: Examples of different H-bond topologies possible for a 10-water unit cell of ice VI. After the cell is periodically replicated, each water molecule is hydrogen-bonded to four others, and the oxygen atoms are in nearly the same positions. The black bonds are covalent, and the white bonds are hydrogen bonds.

range 123−128 K, but these experiments did not reveal the structure of the low-temperature phase. Kuhs *et al.* [44] obtained neutron diffraction data on ice VI under temperature and pressure conditions where ice VI is stable, unlike earlier diffraction experiments where the diffraction experiments were performed at ambient pressure on samples recovered from high-pressure cells. Their data, taken at 225, 125, and 8 K, was not sufficient to fully determine the structure. They found no evidence of the transformation observed by Johari and Whalley, [89] although the transition might be too slow compared to their experimental time scales.

In this chapter, we report periodic DFT calculations for many H-bond isomers of ice VI, and the prediction of the low-temperature phase transition that results from those calculations. Our calculations predict that H-bond-disordered ice VI should give way to H-bond-ordered ice VI′ near 108 K. At this point, ice VI′ should be more stable than ice VI, and at least be a metastable, if not the globally stable, phase. Factors that might affect global stability are discussed in section 3.4. In section 3.2, we discuss graph invariants as applied to proton-disordered ice VI. The periodic DFT [69, 71] results are presented in section 3.3, and our predictions for the thermodynamic limit are developed there.

3.2 Graph invariant theory for ice VI

The smallest unit cell we examined was the primitive unit cell containing 10 water molecules (Fig. 3.2a). The projection operator for the totally symmetric representation, when applied to some of the bonds in Fig. 3.2a, $\hat{G}(b_r)$, did not always yield zero, indicating that, algebraically, some first-order invariants exist. However, all the first-order invariants vanished when evaluated for bond configurations allowed by periodicity and the ice rules. Applying the projection operator to bond pairs, $\hat{G}(b_r b_s)$, we find 22 linearly independent second-order invariants. Some of them, as is obvious for those generated from projection on the square of one bond, $\hat{G}(b_r b_r)$, evaluate to constants. The remaining second-order invariants could be sorted into groups based on the geometrical features of the generating bond pairs, such as whether the generating bond pair both lay in the same sub-lattice, and distance between the two bonds of the generating pair. We found that only invariants generated by proximate bonds had significant weight in the energy fit, and were the only invariants necessary to

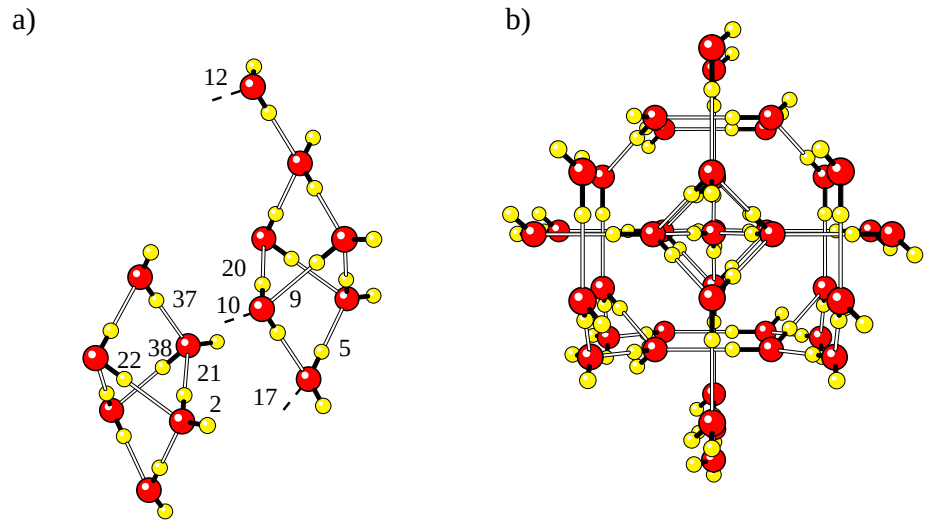

Figure 3.2: a) A fragment of ice VI, as viewed perpendicular to the $c-$axis, depicting the 10-water primitive unit cell of ice VI, and some additional waters that help clarify the bonding pattern. Labels for the bonds used to generate the graph invariants, as described in Table 3.1, are indicated in the figure. The dashed lines represent H-bonds emanating from waters not explicitly shown in the figure. b) A larger unit cell, measuring $\sqrt{2} \times \sqrt{2} \times 2$ primitive cells on each side, containing 40 water molecules as viewed down the $c-$axis. The lowest-energy isomer, that of the ice VI$'$ phase, is shown. It consists of two interpenetrating, but not interconnected lattices. Bonds which appear horizontal in the figure all point to the left, while bonds that are vertical all point downward.

achieve acceptable accuracy in fitting energy as a function of H-bond topology, as in Eq. (2.15). The invariants which were significant are given in Table 3.1, where the generating bond pairs are defined with reference to Fig. 3.2a. One main result, as discussed in the previous chapter, is that invariants for a small unit cell are also invariants for a larger unit cell. A larger unit cell will, in general, also contain additional invariants which are generated by projection on bond pairs $b_r b_s$ which are separated further than possible in the smaller cell. At some point, we expect that addition of further invariants involving bond pairs far from each other will make no improvement

invariant	generating bond pair	distance(Å)	same sub-lattice?	10-water (Γ only)	10-water ($2 \times 2 \times 2$)	40-water (Γ only)
1	5,37	3.56	N	0.0484750	0.0467906	0.0469840
2	2,17	3.29	N	0.0128617	0.0224267	0.0161480
3	10,21	3.29	N	0.0502166	0.0552413	0.0451664
4	22,38	2.77	Y	−0.0103455	−0.0105270	−0.0143332
5	9,20	0.00	Y	−0.0088294	−0.0451725	−0.0367145
6	9,21	3.29	N	−0.0328446	−0.0391773	−0.0383506
7	10,12	5.70	Y	−	−	−0.0049708

Table 3.1: Geometrical features and contribution to the description of the energy of H-bond isomers of the second-order graph invariants. Invariant 7 does not appear as a linearly independent invariant in the 10-water, primitive $1 \times 1 \times 1$ cell The indices of the generating bond pair refer to Fig. 3.2. The distance associated with each bond pair is the distance between the closest vertices from each bond in an ideal structure before geometry optimization. The last three columns give the fitting coefficients for each of the invariants as used in Eq. (2.15) for the energy in units of kcal mol^{-1} per water.

in the energy [Eq. (2.15)]. At that point, the invariant expansion is converged and electronic structure calculations on larger cells are no longer necessary. Furthermore, even within a small unit cell we only require bond pairs that either share a common vertex, or for whom b_r and b_s contain vertices that are nearest neighbors. This is confirmed below for ice VI. Therefore, the expansion for which second-order graph invariants provide the leading term appears to converge quite rapidly.

Once the coefficients α_{rs} have been determined from electronic structure calculations, the energy expression in Eq. (2.15) serves as the Hamiltonian for what is effectively a spin-lattice model. While it is possible to derive analytic approximations to solve this model, we have simply used relatively inexpensive Metropolis Monte Carlo simulations to obtain predictions without introducing further approximations. Extrapolation of electronic structure calculations to large cells using graph invariants is essential. For example, Kuo and Klein [68] predicted that the ice VII/VIII transition should occur at 150 K based on energetics of a cell consisting of 16 water molecules. Using similar energetics as input to the graph invariant theory, a transition temperature of 228 K was calculated, in better agreement with experimental reports of 274 K [47] and 263 K [44].

3.3 Results

Ice VI consists of two interpenetrating, but not interconnected lattices with a tetragonal unit cell. The space group is $P4_2/nmc$. The lattice constants used in the following calculations were $a = 6.181$ Å and $c = 5.698$ Å as determined by diffraction experiments [44] in the region of stability of ice VI, at 1.1 GPa and 225 K. Kuhs *et al.* report that the $a-$ and $c-$axis lattice constants change by -0.15 Å(-2.4%) and

0.10 Å(+1.8%), respectively, upon decreasing the temperature from 225 to 8 K at 1.1 GPa. [44] The smallest unit cell we examined was the primitive unit cell containing 10 water molecules. The 45 symmetry-distinct H-bond isomers possible in this unit cell were enumerated, using previously described methods [50, 51, 68]. Geometry optimizations were performed on all 45 H-bond isomers using the CPMD [69–71] program with periodic boundary conditions. We employed the BLYP gradient correction [72,73] to the local density approximation, Troullier-Martins norm-conserving pseudopotentials [74], and a planewave cutoff 70 Ry in the DFT calculations. Sampling of the Brillouin zone was either restricted to the Γ point, or sampling was extended by way of a $2 \times 2 \times 2$ $k-$point grid using the Monkhorst-Pack scheme. [90]

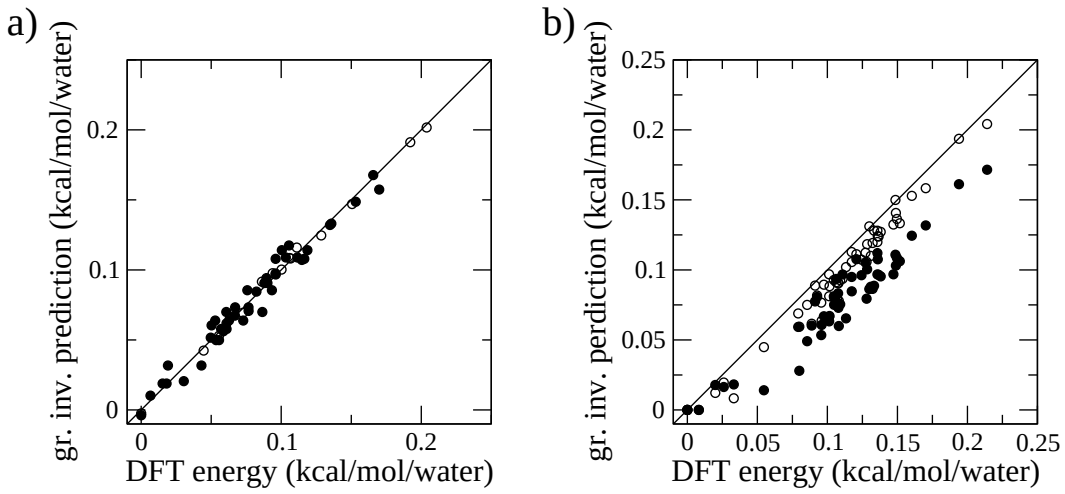

Figure 3.3: a) Test of the ability of the graph invariant expansion, Eq. (2.15), to fit the energies of the 45 H-bond isomers of a 10-water unit cell of ice VI. The filled symbols are the energies calculated using only the $\Gamma-$point, and the open symbols are a fit to the energies of 15 isomers calculated with $2 \times 2 \times 2$ $k-$point sampling. b) Test of the ability of graph invariant parameters derived from the 10-water cell to predict energies of a larger 40-water cell. The filled symbols are a comparison for parameters derived from $\Gamma-$point calculations for the 10-water cell. The open symbols are a similar prediction using extended $2 \times 2 \times 2$ $k-$point sampling. In both plots, a line of slope unity is shown to indicate where points would lie for perfect agreement.

The ability of the expansion of Eq. (2.15), using invariants 1−6 of Table 3.1, to fit the energies of the isomers of the 10-water unit cell is evaluated in Fig. 3.3a. The fitted value is plotted as a function of the actual DFT energy. If a perfect fit was achieved, all the points would lie on the diagonal. As can be seen from the figure, even though the energy difference between isomers is quite small, the typical error fitting Γ-point energies of the 45 symmetry-distinct isomers is a small fraction of the energy range. Furthermore, we recalculated some of the energies using $2 \times 2 \times 2$ $k-$point sampling and, among those isomers, the fit was even better.

As mentioned in section 3.2, any invariant present in a small unit cell is also an invariant for a larger unit cell whose cell vectors are multiples of those of the smaller cell. Fig. 3.3b shows that by the time we move beyond the 10-water cell, we are very close to the point where the additional invariants that arise from larger cells are not important in describing the energy of the H-bond isomers. We performed DFT calculations for 54 isomers of a 40-water cell measuring $\sqrt{2} \times \sqrt{2} \times 2$ primitive cells on each side. The 40-water cell energies predicted using invariant functions from the smaller 10-water cell with the coefficients determined from the smaller cell calculation are compared with the calculated energies for the 40-water cell in Fig. 3.3b. Using the coefficients from the Γ−point calculation for the small cell, we find that the prediction from the small cell has the correct trend, but the prediction underestimates the range of energies in the larger cell. Actually, this effect does not a indicate lack of convergence of the invariant expansion, but rather the inadequacy of taking only the Γ−point for the small cell. Coefficients determined by $2 \times 2 \times 2$ $k-$point sampling of the small cell, the open symbols in Fig. 3.3, yield an excellent prediction of the energies in the 40-water cell. The larger cell, even though calculated at the Γ−point,

effectively includes more $k-$point sampling than a $\Gamma-$point calculation for the small cell. Therefore, the small-cell coefficients obtained with extended $k-$point sampling do a better job predicting the energetics of the large cell. Ideally, one needs to converge the energies with respect to $k-$point sampling for each cell size.

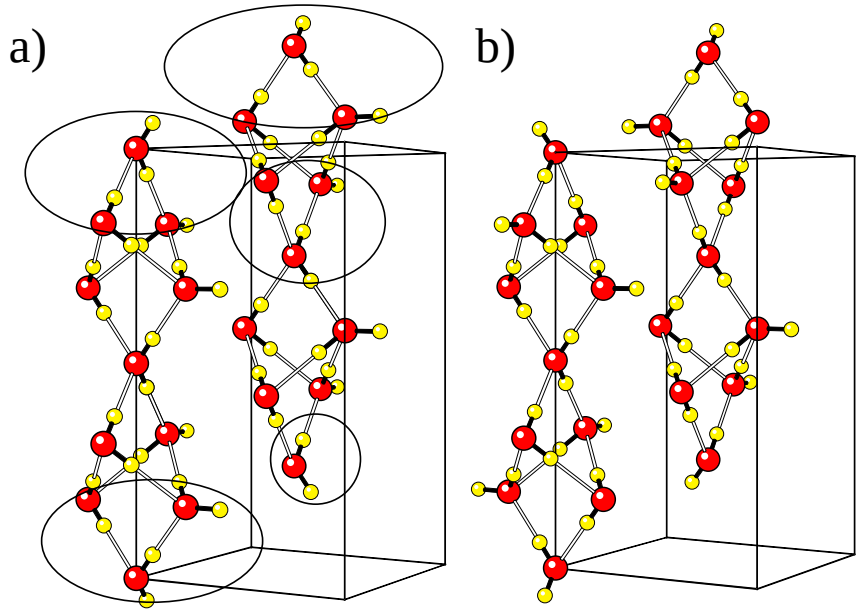

Figure 3.4: H-bond orientations of the ferroelectric ground state(a) and second lowest-energy anti-ferroelectric structure(b) indicating the smallest repeating unit for each of the independent lattices that generate the second lowest-energy isomer, as determined from DFT calculations on a 40-water unit cell of ice VI, viewed perpendicular to the $c-$axis. The H-bonds, in orientation (b), are anti-ferroelectrically oriented for each lattice making the overall structure anti-ferroelectric. This arrangement of H-bonds has tetragonal symmetry and is assigned the space group $P2_12_12_1$ as determined using the FINDSYM [8] program. The H-bonds parallel to the a$-$ and b$-$axes point in a counter-clockwise fashion as one looks down the $c-$axis. The bonds that must be reversed to interconvert the two structures are circled on the left.

Among the new invariants possible for the larger 40-water cell that are not present in the 10-water cell, all the first-order invariants evaluated to zero for configurations allowed by periodicity and the ice rules, just as they did for the smaller cell. We included one of the new second-order invariants, invariant 7 in Table 3.1, for the following reason. In the large unit cell, the two lowest-energy H-bond isomers, shown in Fig. 3.4, are nearly degenerate. Invariant functions $1-6$ in Table 3.1 have exactly the same value for these two isomers. We therefore included a new second-order invariant from the 40-water cell that broke the degeneracy between these isomers. As can be seen from the last column in Table 3.1, the coefficient of this invariant is quite small.

The lowest-energy structure of the 10-water unit cell was a ferroelectric structure (Fig. 3.2 and Fig. 3.4a) whose space group is Cc, as confirmed using the FINDSYM program. [8] We attempted to identify alternative low-energy structures for the larger 40-water cell using Monte Carlo sampling based on invariants obtained from the 10-water cell, much like the Monte Carlo simulations described below. Of the low energy structures identified in this way, the ferroelectric Cc structure was still the ground state. The energy of an anti-ferroelectric structure of $P2_12_12_1$ symmetry (right side of Fig. 3.4) was only 4 K per water molecules higher in energy, as determined from DFT calculations on the 40-water unit cell. The two structures actually have many H-bonds oriented in the same way. Those bonds that must be reversed to go from the ferroelectric to anti-ferroelectric structures are circled in Fig. 3.4. While the electronic structure methodology we use has proved to be remarkably accurate for the ice VII/VIII and Ih/XI transitions, the very small energy difference between the two structures in Fig. 3.4 implies that both structures should be considered as

candidates for the ground state of ice VI′. We explored the effect of reversing the energetic ordering of the two structures shown in Fig. 3.4 by artificially changing the sign of the coefficient of invariant 7 in Table 3.1, and report those results below.

Using the invariant parameters obtained from the 40-water unit cell and Eq. (2.15) for the energy, we have an effective Hamiltonian describing H-bond fluctuations. In essence, we have turned the H-bond order/disorder problem into a spin lattice model. Metropolis Monte Carlo simulations were performed on a simulation cell measuring five primitive unit cells on each side containing 1250 waters. The seven invariant coefficients obtained from the 40-water unit cell were used to evaluate Eq. (2.15) for the simulation cell. A series of simulations were performed for both decreasing and increasing temperature. The lowest-energy isomer, as determined from DFT calculations, was the starting configuration for the initial low-temperature simulation. The final H-bond configuration in a preceding simulation was always the initial configuration in the next simulation. A highly disordered configuration obtained from simulation at an extremely large temperature ($\sim 10^7$ K) was used to initialize the sequence of simulations descending in temperature. The simulations predict a first-order phase transition near 108 K to the ferroelectric ground state identified from calculations on the 10 and 40-water unit cells. As shown in Fig. 3.5, negligible hysteresis, 1−2 degrees, is observed from the series of simulations with decreasing and increasing temperature. The predicted proton ordering transition temperature is located in a region of the phase diagram where the ice II−VI and VI−VIII extrapolated phase boundaries have not intersected. Partial H-bond ordering above the transition and disordering below the transition is observed. Shown in Fig. 3.5b is $\langle \cos \theta_{ab} \rangle$, the average cosine between unit vectors in the direction of the total dipole for each

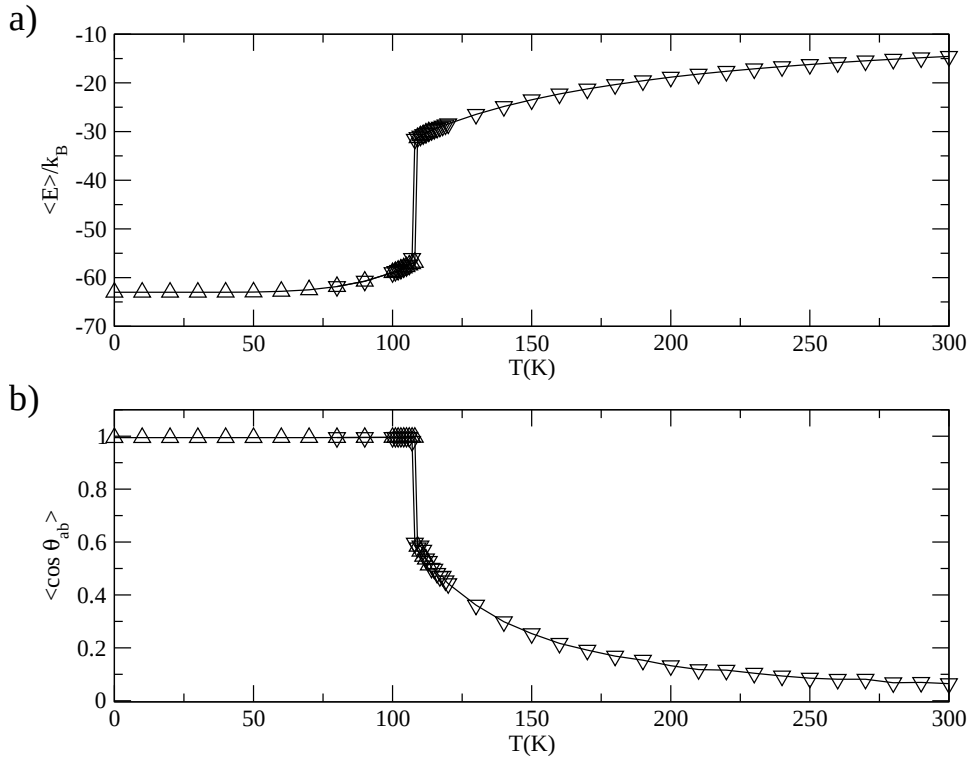

Figure 3.5: a) Average energy plotted as a function of temperature from Metropolis Monte Carlo simulations for a simulation cell of ice VI containing 1250 waters. b) Ferroelectric ordering of the ice VI lattices as a function of temperature. Data is presented for series of Metropolis Monte Carlo runs ascending($\triangle$) and descending(∇) in temperature.

sub-lattice of the ice VI structure.

$$\langle \cos\theta_{ab} \rangle = \left\langle \frac{\mathbf{M}_a \cdot \mathbf{M}_b}{|\mathbf{M}_a||\mathbf{M}_b|} \right\rangle \tag{3.1}$$

In the above equation, $\mathbf{M}_a$ and $\mathbf{M}_b$ are the total dipole moments of the two sub-lattices of the ice VI lattice calculated using a bond dipole approximation. Ferroelectric ordering of the H-bonds takes place over a wide temperature range gradually starting from above 300 K.

Even though the low-energy ferroelectric and anti-ferroelectric configurations shown in Fig. 3.4 are quite close in energy, the simulations rapidly convert to the ferroelectric configuration at all temperatures below the transition temperature. We found no evidence of a barrier to this conversion. Given that the lowest-energy ferroelectric and next-lowest-energy anti-ferroelectric structures are quite close in energy, we sought to determine the effect of reversing the energetic ordering of these two structures. We could accomplish this conveniently by changing the sign of the small coefficient of invariant 7 in Table 3.1, the one added to distinguish the energy of these two structures. After this change, the energies of the other configurations are barely shifted. We find that reversing the energetic order of the two low-energy structures causes ice VI′ to be anti-ferroelectric, but the transition occurs within 2 K of the transition to the ferroelectric phase found with the original parameters.

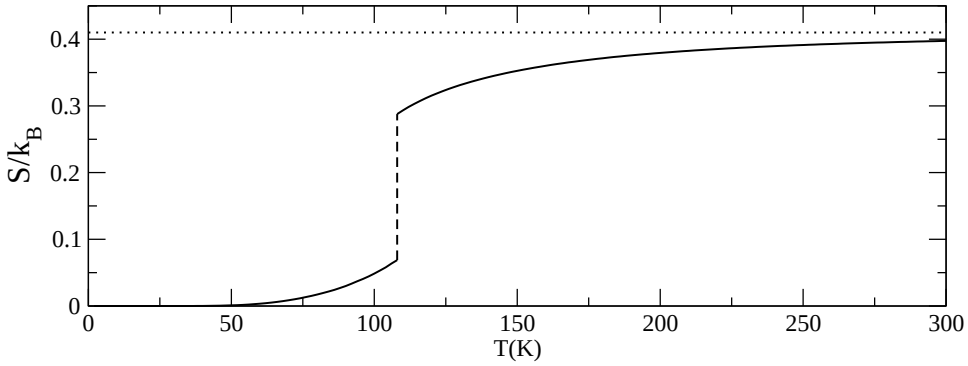

Figure 3.6: Entropy plotted as a function of temperature calculated from Metropolis Monte Carlo simulations on a 1250-water simulation cell. The horizontal line is the Pauling entropy for a fully disordered ice lattice. With decreasing temperature, 29.8% is lost before the transition, 45.5% at the transition, and 24.7% is lost as the ferroelectric ground state is formed.

Entropy as a function of temperature is shown in Fig. 3.6. The entropy of the low-temperature phase was calculated by thermodynamic integration from 0 K and that of the high-temperature phase from infinite temperature. The entropy at infinite temperature is taken to be the Pauling entropy for a fully disordered arrangement of H-bonds in ice. With decreasing temperature, 29.8% of entropy is lost before the transition while 24.7% is lost after the transition. The calculated entropy at the transition is 45.5% of the ideal value for a fully disordered ice phase.

3.4 Discussion

In this work, we have presented the results of DFT calculations on H-bond isomers for two unit cells of ice VI. The lowest-energy H-bond isomer in each case was ferroelectric, space group Cc. From calculations on a larger unit cell, an anti-ferroelectric H-bond isomer was identified lying 4 K per molecule higher in energy. This configuration was assigned the space group $P2_12_12_1$.

From application of graph invariants and DFT calculations on small unit cells, the energy differences in H-bond fluctuations for a large simulation cell, containing 1250 waters, could be calculated. A first-order phase transition to the proton-ordered ferroelectric ground state (Fig. 3.4a) was observed near 108 K. We note that an anti-ferroelectric structure (Fig. 3.4b) lies very close to the ferroelectric structure in energy. If more accurate electronic structure calculations would indicate that the anti-ferroelectric structure is actually lower in energy, our explorations with the anti-ferroelectric structure as the ground state reported in section 3.3 suggest that we would find a transition at almost the same temperature, but to an anti-ferroelectrically ordered phase.

We have shown that H-bond-disordered ice VI gives way to a proton-ordered phase near 108 K. While we have shown that the ordered phase is more stable than ice VI, establishing this phase as the global minimum in this portion of the phase diagram is another, and more difficult matter. To establish whether ice VI′ is globally stable we would have to determine whether there exists another phase with a different underlying oxygen lattice that supersedes ice VI′ as the stable phase in this region. In fact, this scenario does occur in the case of ice III, which can order into metastable ice IX which is superseded by the more stable ice II. There is also a possibility that ice VI might give way to either ice II or ice VIII at low temperatures. In the phase diagram of ice, the range of pressure where ice VI is stable seems to shrink as temperature is lowered, as the ice II and VIII regions expand. If the ice II and VIII regions would expand and meet at low temperature, providing a lower bound to the ice VI phase, then our ice VI′ phase would be metastable with respect to either ice II or VIII. At our calculated transition temperature of 108 K, ices II and VIII are typically drawn as separate, [1] but the phase diagram is not well characterized in this region. In summary, we cannot exclude another phase intervening and rendering ice VI′ only metastable. However, even in such a case (like ice III/IX) experimental evidence for the metastable phase may be obtained.

In our calculations, significant proton ordering was observed above the transition over a wide temperature range. This should be observable in calorimetric experiments provided that H-bond arrangements can equilibrate on an experimental time scale. (The H-bonds in phases such as ices VII and VIII seem to reach equilibrium on an experimental time scale, while those in ices Ih and XI do not.) Even below the transition, the degree of residual proton disorder is much larger than we found in ice XI or

ice VIII. We were somewhat surprised that, despite the near degeneracy of ferroelectric and anti-ferroelectric structures, fluctuations to anti-ferroelectric configurations do not persist to lower temperatures. Simulations initialized with the H-bond configuration of the second lowest-energy anti-ferroelectric isomer rapidly transformed to the ferroelectric ground state, indicating that factors beside energetics (i.e. entropic factors) seem to also favor the ferroelectric state. In Fig. 3.5b, we see that the dipole moment of the sub-lattices have nearly complete ferroelectric order at all temperatures below the transition. In conclusion, we have predicted that ice VI will transform into an H-bond-ordered phase near 108 K, and have identified the likely low-temperature phase as ferroelectric with an anti-ferroelectric structure close by in energy.

CHAPTER 4

A REEXAMINATION OF THE ICE III/IX HYDROGEN BOND ORDERING PHASE TRANSITION

4.1 Introduction

The phase diagram of ice contains numerous stable and metastable phases over a range of pressures and temperatures. A number of these phases are hydrogen bond (H-bond) disordered, and when cooled to lower temperatures, under appropriate conditions, they transform to proton-ordered crystals. At low pressures, these H-bond ordering transitions occur via molecular rearrangements of the water molecules. At atmospheric pressure, proton-disordered ice Ih transforms to what is believed to be ferroelectric ice XI near 72 K for H_2O and 76 K for D_2O in the limit of vanishing hydroxide dopant [17,34,80–82]. When cooled faster than 1 K per minute, ice III transforms to metastable proton-ordered ice IX, which exists in the stability region of ice II. [83–85,91] Ice VII transforms to its proton-ordered counterpart, anti-ferroelectric ice VIII, between 2.1−12 GPa at constant temperature. At still higher pressures, the transition temperature abruptly decreases as the mechanism of transformation changes from molecular rearrangement to proton tunneling across the shortened H-bond.

The stability region of ice III occupies a small portion of the phase diagram, in comparison to the other stable phases, extending from 240−260 K and 0.2−0.4 GPa. The unit cell, first identified by Tammann in 1900 [92], is described by a tetragonal arrangement of oxygen atoms, space group $P4_12_12$, as determined by X-ray [83,93,94] and neutron [12, 14, 95] diffraction experiments. Proton order was suggested by infrared spectra [96] near 100 K, and later confirmed when dielectric experiments [84] indicated that a progressive ordering takes place as the temperature is lowered from 210 to 165 K. Ice III, when cooled at about 1 K per minute or faster, transforms to a metastable H-bond-ordered version known as ice IX which has the same symmetry as its proton-disordered counterpart. [9, 14, 83–85] Subsequent warming of ice IX back across the transition results in the formation of ice II, the stable phase in this region of the phase diagram. The space group $P4_12_12$ allows for the possibility that the H-bonds may be partially ordered or disordered in ices III and IX respectively. La Placa *et al.* [9] identified one of four possible H-bond arrangements possessing the appropriate symmetry, configuration (d) in Fig 4.1, to be the structure of ice IX, in agreement with earlier suggestions [83, 84]. The error in their refinement was acceptable only after deuterons were allowed to fractionally occupy sites other than those of the dominant H-bond arrangement. They proposed that this disagreement with dielectric experiments [84], which suggested a fully ordered structure, may have resulted either from the rate of cooling or as a feature of the ice IX structure. Calculations reported by Handa *et al.* [97] also suggested that ice IX is fully ordered, but their calculated heat of transition is almost twice that measured by Nishibata and Whalley [85]. This discrepancy has yet to be resolved.

Using a differential calorimetric technique, Nishibata and Whalley [85] measured the heat of transition, -56 cal mol^{-1}, for the ice III$-$IX phase transition. The measured change in entropy, -0.32 cal K^{-1} mol^{-1}, is nearly 40% of the expected value if ice III is fully disordered and ice IX fully ordered. This suggests that to some degree, ice IX is partially disordered and ice III partially ordered. Neutron diffraction experiments are able to determine occupational probabilities for deuteron sites. The symmetry of the ice III/IX structures permits the probabilities of protons residing in one of two possible sites along a given H-bond to be summarized by two occupancy probabilities, α or β, as shown in Fig 4.1. For the ice IX structure, Londono *et al.* [14] determined that α and β were 2.9 and 5.6% respectively, in agreement with earlier reported values of $\alpha = 3.4\%$ and $\beta = 5.1\%$. [9] For partially ordered ice III, Londono *et al.* [14] determined that α and β were 33 and 41% respectively. With samples of higher quality and a more flexible refinement, Lobban *et al.* [12] determined that $\alpha = 35\%$ and $\beta = 50\%$. Mean field statistical mechanical models have been developed to approximate the configurational entropy of partially ordered structures using these occupational probabilities as input. [11, 87, 98, 99] The most recent of which is able to account for multiple occupational parameters which is necessary in ices III and V. [100] Lobban *et al.* [12] have discussed how their diffraction data used in conjunction with these models imply changes in entropy at the ice III/IX transition significantly different than that reported by Nishibata and Whalley. [85] Our results from statistical simulations, as discussed below, may provide insight into this discrepancy.

In this chapter, we report results from periodic DFT calculations for many H-bond isomers of ice III, extended to a full statistical mechanical theory of the ice III/IX phase transition using graph invariants. [19,22,23,51] Our calculations indicate

that proton-disordered ice III is partially ordered before transforming to partially disordered ice IX, near 126 K, which becomes fully ordered at lower temperatures. In section 4.2, we present a brief review, from section 2.2, of the graph invariant theory by which we calculate energy differences among H-bond isomers in a large simulation cell using data extrapolated from DFT [69, 71] calculations on small systems. The results of periodic DFT calculations are presented in section 4.3 where we discuss the necessity of a converged $k-$point sampling if the ground state is to be correctly identified. We then report the results from statistical simulations on a large unit cell of ice III comparing our results to available experimental data and mean field models in section 4.4. We conclude with a discussion of our results and their implications.

4.2 Graph Invariants for Ice III

Hydrogen bonds are directional, with the convention taken that H-bonds point from the covalently bonded hydrogen of a donor molecule to the lone pair on oxygen of an acceptor molecule. In all but the highest pressure phases of ice, each water molecule donates two hydrogen bonds with nearest-neighbor acceptor molecules and accepts two H-bonds from nearest-neighbor donor molecules. There can be many H-bond arrangements which satisfy these so-called "ice rules" [101], leading to the existence of several H-bond-disordered phases of ice. The small entropy differences among these H-bond isomers lead to transitions to ordered phases at lower temperatures. As shown in chapter 2, the H-bond network can be summarized mathematically as vertices, oxygen atoms, connected by directed lines, H-bonds. The oriented graph representing an H-bond isomer of an ice lattice is specified by a set of bond variables, b_r for the rth bond, which take the values ± 1 depending on whether the H-bond points along, or opposite

to, an arbitrarily defined canonical orientation. The oxygen atoms, or vertices in this representation, essentially remain stationary during the proton ordering transition. The transformation of ice Ih to ice XI results in a compression along the $a-$ and $c-$axes of only -0.75% and -0.36% respectively, and an elongation of the $b-$axis of 0.84%. [5] Similar changes are observed in the proton ordering transformation of ice VII in which the $a-$ and $c-$axes differ by -1.0% and 2.0% respectively. The lattice constants change by $+0.4\%$ and -3.3% for a and c respectively when ice III is cooled from 250 to 165 K to form ice IX. [14] In the discussion section, we estimate the effect that the volume change might have on the ice III/IX transition.

In our work to date on proton ordering transitions in ice, we have obtained good agreement with available experiments assuming that $A_{vib,i}$, the vibrational free energy in each of the H-bond isomers, is approximately the same: $A_{vib,i} \approx \overline{A}_{vib}$. Then the problem reduces to estimating the energy E_i of each of the symmetry-distinct isomers. We determine the E_i's by expressing them as a sum of first- and second-order graph invariants.

$$E(b_1, b_2, \ldots) = E_0 + \sum_r \alpha_r I_r(b_1, b_2, \ldots) + \sum_{rs} \alpha_{rs} I_{rs}(b_1, b_2, \ldots) \tag{4.1}$$

In the above equation, E_0 is an overall constant for the energy, and the sums are over first- and second-order invariant functions of the bond variables, $I_r(b_1, b_2, \ldots)$ and $I_{rs}(b_1, b_2, \ldots)$ respectively. We identify the first-order invariants with a single subscript "r" to indicate the bond from which the invariant is generated by action of the projection operator. Obviously, several bonds can generate the same invariant so the notation is not unique. Second-order invariants are denoted with a double subscript "rs" to indicate the bond pair $b_r b_s$ that is projected. Typically, the first-order invariants, in Eq. (4.1) vanish either because of symmetry or the constraints of the

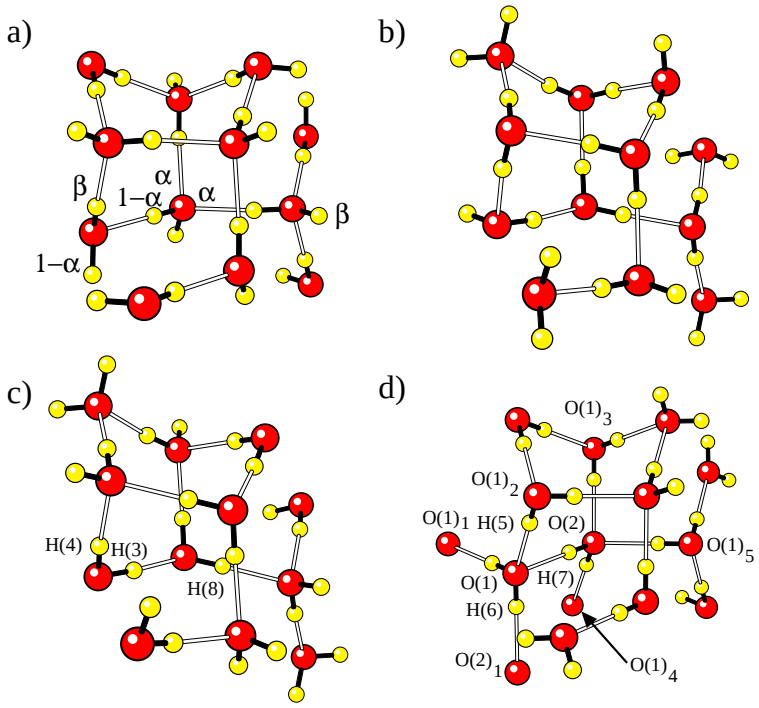

Figure 4.1: Examples of H-bond configurations of the primitive unit cell of ice III which have $P4_12_12$ symmetry and obey periodic boundary conditions. After the cell is periodically replicated, each water molecule is hydrogen bonded to four others. The black bonds are covalent and the white bonds are hydrogen bonds. The space group $P4_12_12$ allows for two occupational probabilities, α and β, to describe the H-bond topology. If one site of an H-bond has a probability of being occupied of α, then the other site, within the same H-bond, has a probability of $(1-\alpha)$. All proton sites related by symmetry have the same occupational probability. The configurations are labeled (a,b,c,d) corresponding to those configurations considered in Ref. [9], with configuration (d) representing the fully ordered ice IX structure where α and β equal zero. Configurations (c) and (d) differ in that all H-bonds are reversed. Oxygen atoms found in adjacent unit cells are shown for identification of structural data found in Tables 4.2 and 4.3. $O(1)_i$ and $O(2)_i$ identify two families of symmetry-related oxygen atoms in the unit cell of ice III. Oxygen atom $O(1)_4$ is hydrogen bonded to H(7)−O(2) as indicated by the arrow.

ice rules. The two exceptions to date are ices III and V where first-order invariants provide the leading dependence in our expression for energy. The coefficients α_{rs} are determined by fitting to the results of periodic DFT calculations. If the approximation $A_{vib,i} \approx \overline{A}_{vib}$ would break down, then an alternative would be to fit the $A_{vib,i}$ to invariants with an expression similar to the energy expansion in Eq. (4.1). The smallest unit cell we examined was the primitive unit cell containing 12 water molecules (Fig. 4.2).

The bonds in the unit cell of ice III belong to one of three sets (orbits) of symmetry-related bonds. The projection operator for the totally symmetric representation, when applied to the bonds in Fig. 4.2, $\hat{G}(b_r)$, yielded three unique, linearly-independent first-order invariants. Applying the projection operator to bond pairs, $\hat{G}(b_r b_s)$, we find 45 unique, linearly independent second-order invariants. Some of them, as is obvious for the three generated from projection on the square of one bond, $\hat{G}(b_r b_r)$, evaluate to constants for pure water ice with no defects. Their effect is included by the constant E_0 in Eq. (4.1). The remaining second-order invariants could be sorted into groups based on geometrical features of the generating bond pairs, such as the distance between the two bonds of the generating pair. We found that energy as a function of the H-bond topology could be fit with acceptable accuracy using only invariants generated by proximate bonds. The invariants which were significant are given in Table 4.1, where the generating bond pairs are defined in reference to Fig. 4.2a.

One main result from the previous chapters is that invariants for a small unit cell are also invariants for a larger unit cell. A larger unit cell will, in general, also contain additional invariants which are generated by projection on bond pairs $b_r b_s$

invariant	generating bonds	distance(Å)	occupancy parameter	12-water (Γ only)	12-water ($2 \times 2 \times 2$)	48-water (Γ only)
1	2,3	2.73	α,α	−0.0189300	−0.0355877	−0.0319170
2	1,4	3.45	α,α	−0.0048711	0.0312539	−0.0186354
3	1,3	2.73	α,α	−0.0213581	0.0173227	−0.0554111
4	4,9	2.98	α,β	−0.0153386	−0.0383516	−0.0125568
5	8,17	2.73	α,α	0.1087494	0.0599093	0.1050547
6	3,17	0.00	α,α	0.0942803	0.0990837	0.1047808
7	15,17	2.73	β,α	−0.1012657	−0.0717686	−0.0923311
8	17,18	2.73	α,α	−0.1087226	−0.1222358	−0.0597738
9	9	–	β	0.0697125	−0.0079468	−0.0091154

Table 4.1: Geometrical features and contribution to the description of the energy of H-bond isomers of the first- and second-order graph invariants. The indices of the generating bond pair refer to Fig. 4.2. The distance associated with each bond pair is the distance between the closest vertices from each bond in an ideal structure before geometry optimization. The occupancy parameters to which each H-bond contributes are identified. The last three columns give the fitting coefficients for each of the invariants as used in Eq. (4.1) for the energy in units of kcal mol^{-1} per water.

which are separated further than possible in the smaller cell. At some point, we expect that addition of further invariants involving bond pairs far from each other will make no improvement in the energy [Eq. (4.1)]. At that point, the invariant expansion is converged and electronic structure calculations on larger cells are no longer necessary. In practice, we have found that calculations on relatively small unit cells are sufficient, provided convergence with respect to $k-$point sampling has been reached. Furthermore, even within a small unit cell we only require bond pairs that either share a common vertex, or for whom b_r and b_s contain vertices that are nearest-neighbors. This is confirmed below for ice III. Therefore, the expansion for which Eq. (4.1) is the leading term appears to converge quite rapidly.

Once the coefficients α_{rs} have been determined from electronic structure calculations, the energy expression in Eq. (4.1) serves as the Hamiltonian for what is effectively a spin-lattice model. While it is possible to derive analytic approximations to solve this model, we have simply used relatively inexpensive Metropolis Monte Carlo simulations to obtain predictions without introducing further approximations. Extrapolation of electronic structure calculations to large cells using graph invariants is essential. For example, Kuo and Klein [68] predicted that the ice VII/VIII transition should occur at 150 K based on energetics of a cell consisting of 16 water molecules. Using similar energetics as input to the graph-invariant theory, a transition temperature of 228 K was calculated, in better agreement with experimental reports of 274 K [47] and 263 K [44]. Furthermore, some extrapolation procedure like graph invariants is required for a full statistical mechanical theory, without which one cannot obtain predictions of fractional occupancies for comparison with diffraction experiments or thermodynamic quantities for comparison with calorimetry. Using

only small unit cells without extrapolation [102], one obtains diffuse heat capacity peaks shifted from the ultimate thermodynamic limit and unreliable occupancies.

4.3 Periodic DFT and Parametrization of Graph Invariants

The lattice constants used in the following calculations were $a = 6.666$ Å and $c = 6.936$ Å as determined by diffraction experiments [14] in the region of stability of ice III, at 0.28 GPa and 250 K. The smallest unit cell we examined was the primitive unit cell containing 12 water molecules. The 102 symmetry-distinct H-bond isomers possible in this unit cell were enumerated, using previously described methods [50, 51, 68]. Geometry optimizations were performed on all 102 H-bond isomers, using the CPMD [69–71] program with periodic boundary conditions. We employed the BLYP gradient correction [72, 73] to the local density approximation, Troullier-Martins norm-conserving pseudopotentials [74], and a plane wave cutoff of 70 Ry in the DFT calculations. Sampling of the Brillouin zone was either restricted to the $\Gamma-$point or extended by way of a $2 \times 2 \times 2$ $k-$point grid, using the Monkhorst-Pack scheme. [90]

The ability of this level of electronic structure theory to describe the small energy differences among H-bond isomers of ice has been addressed in chapter 2. This methodology identifies the correct low-temperature phase of the ice Ih/XI, VII/VIII, [19] and, in this chapter, III/IX [24] systems. Furthermore, because the transition temperatures are in qualitative agreement with experiment we have some confidence that the energies of higher-lying isomers are adequately described. For ice Ih, we have calculated the energies of the H-bond isomers using different combinations of density functionals and basis sets, finding good agreement. [19] This contrasts with

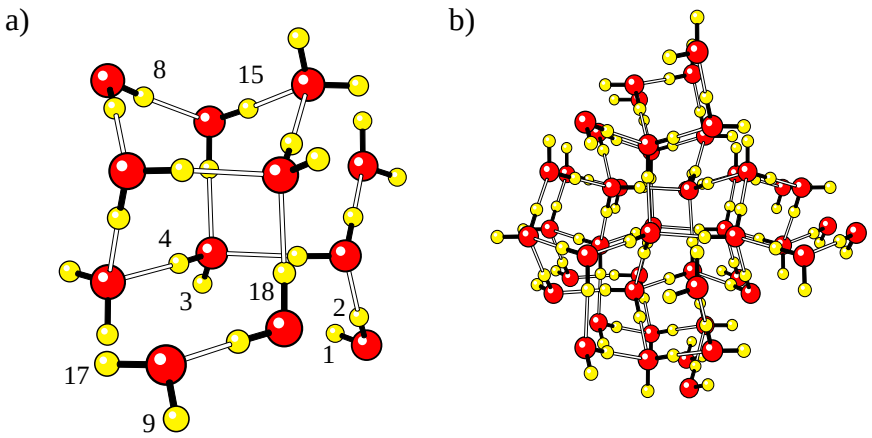

Figure 4.2: (a) A 12-water primitive unit cell of ice III, as viewed down the $c-$axis, which defines the canonical orientation with all bond variables, b_r, equal to $+1$. The labels indicate which bonds were used to generate the graph invariants, as described in Table 4.1. (b) A larger unit cell, measuring $\sqrt{2} \times \sqrt{2} \times 2$ primitive cells on each side, containing 48 water molecules as viewed down the $c-$axis. The lowest-energy isomer, corresponding to the experimentally determined ice IX structure, is shown for both cases. The lowest-energy isomer of the 12-water unit cell only agreed with experiment when sufficient $k-$point sampling was achieved.

the situation for commonly used empirical potentials which can differ in their predictions of energy differences among H-bond isomers by an order of magnitude and fail to identify the correct ground state. [21] Finally, structural features like sub-lattice shifts in ice XI and ice VIII [68] are in agreement with experimentally observed values. The ability of the expansion of Eq. (4.1), using invariants $1-9$ of Table 4.1, to fit the energies of the isomers of the 12-water unit cell is evaluated in Figure 4.3a. The fitted value is plotted as a function of the actual DFT energy. If a perfect fit was achieved, all the points would lie on the diagonal. As can be seen from the figure, even though the energy difference between isomers is quite small, the typical error fitting $\Gamma-$point energies of the 102 symmetry-distinct isomers is a small fraction of

the range of energy differences. The lowest $\Gamma-$point energy structure of the 12-water cell was configuration (c) of Fig. 4.2 in which all bonds are reversed compared to the experimentally determined structure, configuration (d) of Fig. 4.2. This ground state calculated using $\Gamma-$point sampling, which we will eventually show is inadequate for the $1 \times 1 \times 1$ cell, is found 43 K per molecule below the dominant H-bond configuration found experimentally for ice IX. Our results are consistent with another set of recent calculations limited to the $\Gamma-$point [102] where it was shown that the relative energies between this structure and the ice IX structure were insensitive to the method of calculation or changes in lattice constants. However, when we recalculated the energies using an extended $k-$point sampling, the experimental ice IX structure was now the ground-state H-bond isomer, with the other configuration lying 11 and 14 K per molecule higher in energy with a $2 \times 2 \times 2$ and $4 \times 4 \times 4$ $k-$point sampling, respectively.

We next calculated the DFT energies of 50 isomers of a 48-water cell measuring $\sqrt{2} \times \sqrt{2} \times 2$ primitive cells on each side. Using $\Gamma-$point sampling, the ground-state isomer for this unit cell was that of the fully ordered version of ice IX. The energy difference between this structure and the H-bond isomer with all bonds reversed was 13 K per molecule. This value is in good agreement with the energies calculated using extended $k-$point sampling for the smaller cell, reflecting that moving to the larger unit cell increases the effective $k-$point sampling. Calculations extended with a $2 \times 2 \times 2$ $k-$point sampling also yielded an energy difference of 13 K per molecule thus indicating we have reached convergence with respect to $k-$point sampling. The 48-water cell energies predicted by using invariant functions from the smaller 12-water cell with the coefficients determined from the smaller cell calculations are compared

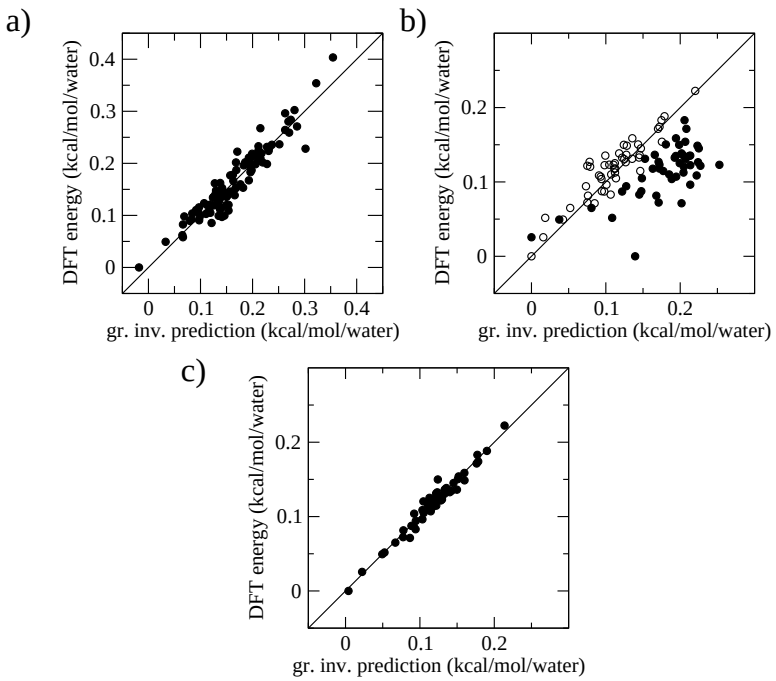

Figure 4.3: (a) Test of the ability of the graph-invariant expansion, Eq. (4.1), to fit the $\Gamma-$point energies of the 102 symmetry-distinct H-bond isomers of a 12-water unit cell of ice III. (b) Test of the ability of graph-invariant parameters derived from the 12-water cell to predict energies of a larger 48-water cell. The filled symbols are a comparison for parameters derived from $\Gamma-$point calculations for the 12-water cell. The open symbols are a similar prediction with extended $2 \times 2 \times 2$ $k-$point sampling. In both plots, a line of slope unity is shown to indicate where points would lie for perfect agreement.

with the calculated energies for the 48-water cell in Fig.4.3b. As mentioned in section 4.2, any invariant present in a small unit cell is also an invariant for a larger unit cell whose cell vectors are multiples of those of the smaller cell. Using the coefficients from the $\Gamma-$point calculations for the small cell, we find that the prediction from the small cell is not adequate to predict the energies of the larger cell. Actually, this does not indicate lack of convergence of the invariant expansion, but rather the inadequacy of taking only the $\Gamma-$point for the small cell. Coefficients determined

by extended $k-$point sampling of the small cell, the open circles in Fig. 4.3b, yield an excellent prediction of the energies in the 48-water cell. The larger cell, even though calculated at the $\Gamma-$point, effectively includes more $k-$point sampling than a $\Gamma-$point calculation for the small cell. Therefore, the small-cell coefficients obtained with extended $k-$point sampling do a better job predicting the energetics of the larger cell. Ideally, one needs to converge the energetics with respect to $k-$point sampling for each cell size. Our previous work was based on invariants derived from larger unit cells and should be close to convergence with respect to $k-$point sampling.

We re-optimized the ground state and second lowest-energy H-bond isomers, configurations (d) and (c) in Fig. 4.1 respectively, increasing the plane-wave cutoff to 90 Ry. Geometric data, such as bond lengths and angles, from these structures are reported in Tables 4.2 and 4.3. The structural data obtained from the calculations are in general agreement with the trends observed in diffraction experiments. [9, 14] Differences are observed when comparing data from the second lowest-energy isomer with the experimental and calculated structures of ice IX. Notable deviations between configuration (c) and experiment are $\angle$O(1)$_1$-H(6)- - -O(2), $\angle$O(2)-H(7)- - -O(1)$_2$, $\angle$O(1)$_3$-O(2)-O(1)$_5$, $\angle$O(1)$_1$-O(1)-O(2)$_1$, and $\angle$O(1)$_1$-O(2)-O(1)$_3$ with differences reaching as large as 11°. Optimization of the ground-state isomer using ice IX lattice constants brings the calculated structural data into closer agreement with experiment.

4.4 Statistical Mechanical Results

Using the invariant parameters obtained from the 48-water unit cell and Eq. (4.1) for the energy, we have an effective Hamiltonian for a spin-lattice model describing

	config. (d) vol.=ice III	config. (d) vol.=ice IX	config. (c) vol.=ice III	ice XI [9] 0.0 kbar,110 K	ice XI [14] 0.0 kbar, 30 K
O(1)-H(5)	0.993	0.993	0.993	0.977	0.991
$O(1)_1$-H(6)	0.992	0.992	0.994	0.972	0.983
O(2)-H(7)	0.994	0.994	0.993	0.979	0.940
H(5)- - -$O(1)_1$	1.702	1.734	1.721	1.789	1.759
H(6)- - -O(2)	1.781	1.765	1.700	1.813	1.839
H(7)- - -$O(1)_2$	1.717	1.761	1.763	1.821	1.832
O(1)-H(5)- - -$O(1)_1$	2.684	2.713	2.695	2.750	2.738
$O(1)_1$-H(6)- - -O(2)	2.756	2.737	2.683	2.763	2.802
O(2)-H(7)- - -$O(1)_2$	2.700	2.751	2.738	2.793	2.768

Table 4.2: Average molecular distances for ice IX obtained from neutron diffraction experiments [9, 14] and the present DFT calculations on a unit cell containing 48 water molecules with the cutoff for the plane wave expansion increased to 90 Ry to converge bond distances and angles. Further increasing the plane wave cutoff to 120 Ry did not significantly alter the geometry. The first two columns are the lowest-energy isomer, corresponding to fully ordered ice IX, with unit cell volumes corresponding to ices III and IX respectively. Data for configuration (c), the isomer where all H-bonds are reversed compared to ice IX, is included for comparison. It should be noted that the hydrogen positions listed in the first column refer to the structure of ice IX, configuration (d). The hydrogen positions for both configurations are defined in Fig. 4.1. Experimental values, using partially ordered models, are shown in the last column. Distances are reported in units of Ångströms(Å).

	config. (d) vol.=ice III	config. (d) vol.=ice IX	config. (c) vol.=ice III	ice XI [9] 0.0 kbar,110 K	ice XI [14] 0.0 kbar, 30 K
∠H(5)-O(1)-H(6)	105.7	105.7	105.3	106.0	106.7
∠H(7)-O(2)-H(7)	104.8	104.7	105.9	104.7	110.1
∠O(1)-H(5)-$O(1)_1$	168.5	168.1	166.9	167.2	168.7
∠$O(1)_1$-H(6)-O(2)	166.9	165.8	170.6	165.0	165.5
∠O(2)-H(7)-$O(1)_2$	170.3	173.4	166.6	174.6	173.3
∠$O(1)_2$-O(1)-$O(1)_1$	114.1	112.6	113.7	112.7	112.6
∠$O(1)_3$-O(2)-$O(1)_5$	93.1	93.1	102.8	90.9	89.4
∠$O(1)_2$-O(1)-$O(2)_1$	141.4	144.4	143.4	143.7	143.7
∠$O(1)_1$-O(1)-$O(2)_1$	98.2	98.1	90.4	98.2	97.8
∠O(1)-O(2)-$O(1)_3$	103.7	105.6	100.9	106.1	–
∠O(2)-O(1)-$O(2)_1$	101.5	101.0	105.9	99.2	97.6
∠O(2)-O(1)-$O(1)_1$	92.2	93.1	93.6	91.9	91.4
∠O(1)-O(2)-$O(1)_5$	130.7	129.3	128.7	128.1	127.4
∠O(2)-O(1)-$O(1)_2$	97.9	96.3	99.9	96.9	99.6
∠O(1)-O(2)-$O(1)_4$	99.4	99.0	98.6	100.8	106.1

Table 4.3: Average molecular angles for ice IX obtained from neutron diffraction experiments [9, 14] and the present DFT calculations. The table is organized similar to Table 4.2 with angles reported in units of degrees(°).

H-bond fluctuations. Metropolis Monte Carlo simulations were performed on a simulation cell measuring five primitive unit cells on each side containing 1250 waters. The nine invariant coefficients obtained from the 48-water unit cell were used to evaluate Eq. (4.1) for the simulation cell. A series of simulations were performed for both decreasing and increasing temperature. The lowest-energy isomer, as determined from DFT calculations, was the starting configuration for the initial low-temperature simulation. The final H-bond configuration in a preceding simulation was always the initial configuration in the next simulation. A highly disordered configuration obtained from simulation at an extremely large temperature ($\sim 10^7$ K) was used to initialize the sequence of simulations descending in temperature. Comparison of the ascending and descending temperature sequences exhibited negligible hysteresis, suggesting that the simulations were adequately equilibrated. The simulations predict a first-order phase transition near 126 K to the anti-ferroelectric ground state identified from calculations on the 12- and 48-water unit cells with $2 \times 2 \times 2$ and $\Gamma-$point sampling respectively.

Entropy as a function of temperature is shown in Figure 4.4b. The entropy of the low-temperature phase was calculated by thermodynamic integration from 0 K, and that of the high-temperature phase integrating from infinite temperature. The entropy at infinite temperature is taken to be Nagle's result for the Pauling entropy for a fully disordered arrangement of H-bonds in ice [10]. With decreasing temperature, 29.7% of the entropy is lost before the transition while 2.6% is lost after the transition. The calculated entropy at the transition is 67.7% of the ideal value for a fully disordered ice phase which is larger than the experimentally observed change in entropy, 40% [85]. In the discussion section, we explain how taking the lattice

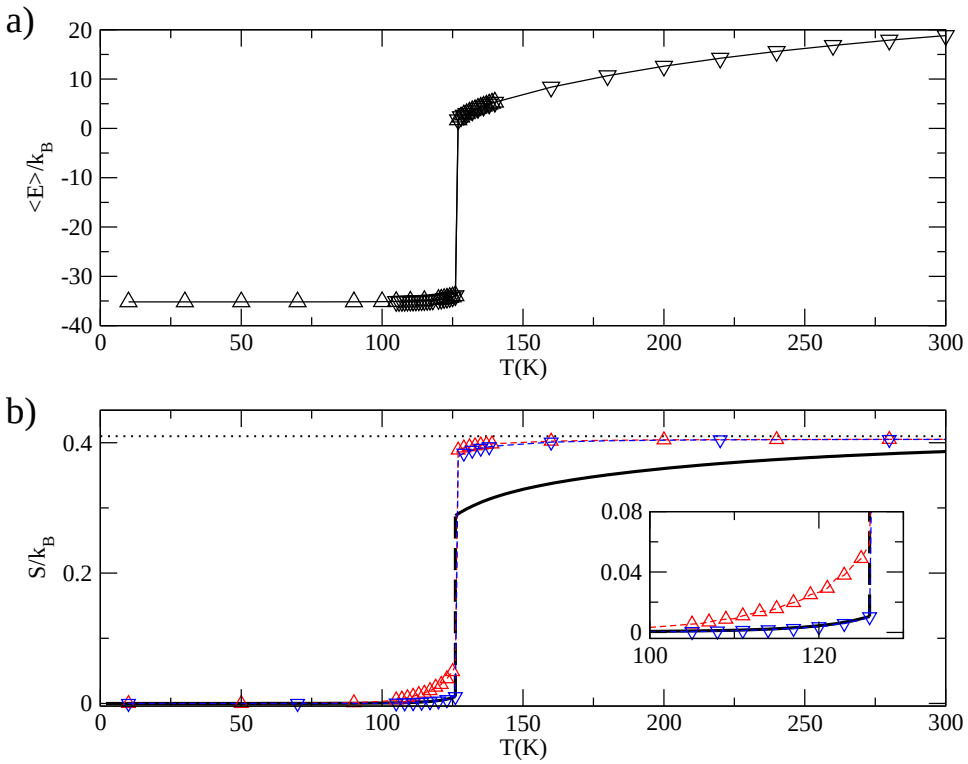

Figure 4.4: (a) Average energy plotted as a function of temperature from Metropolis Monte Carlo simulations for a simulation cell of ice III containing 1500 waters. Energies are presented for a series of Metropolis Monte Carlo runs ascending($\triangle$) and descending(∇) in temperature. (b) Entropy from the present work (thick solid line) plotted as a function of temperature where the horizontal line is the Pauling entropy for a fully disordered ice lattice. With decreasing temperature, 29.7% is lost before the transition, 67.7% at the transition, and 2.6% as the fully ordered ice IX structure is formed. In addition, entropy as a function of temperature calculated using the occupational probabilities, α and β obtained from our simulations, is plotted using the one parameter expressions of Nagle($\triangle$) [10] and Howe and Whitworth(∇) [11].

distortion that accompanies the phase transition into account would further lower the transition entropy. Also plotted in Figure 4.4b is predicted entropy as a function of temperature calculated using various mean-field theories with the occupational probabilities, α and β, obtained from our simulations as input. The occupational parameter α is shown in Fig. 4.5. Our value for α, 38%, at the transition is close to the experimental values, 33% [14] and 35% [12]. Our β, 38%, is close to the value extracted from one diffraction experiment, 41% [14], but rather low compared to a more recent report, 50% [12].

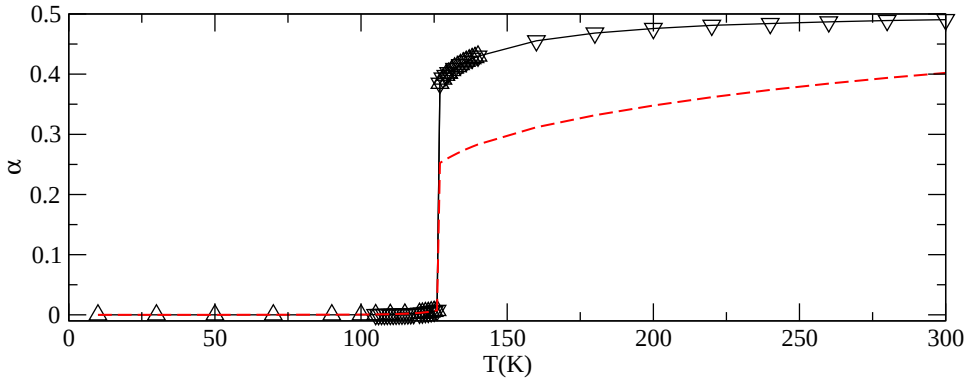

Figure 4.5: Occupational probability, α, plotted as a function of temperature. In the fully disordered ice III and fully ordered ice IX phases, the occupational probabilities are $\alpha = 50\%$ and 0% respectively. From our simulations, $\alpha \approx \beta$ at all temperatures, so only α is shown. Data are presented for a series of Metropolis Monte Carlo runs ascending and descending in temperature. The dashed line corresponds to the occupational parameter as a function of temperature obtained from the model of Howe and Whitworth [11] using entropies from our simulations as input.

In our simulations, the value of β never significantly differed from α, so we could effectively model the system with a one parameter theory for partially disordered ice systems. Using the average of α and β as the single occupational probability for

each temperature, predicted entropy is plotted as a function of temperature obtained from the expressions by Nagle($\triangle$) [98] and Howe and Whitworth(∇) [11] in Fig. 4.4. Application of the two parameter expression by MacDowell *et al.* [100], with α and β from our simulations as input, yielded entropy as a function of temperature that was quantitatively the same as that obtained using the one parameter expression of Howe and Whitworth [11], because our model predicts that α and β are very close to each other. Howe and Whitworth's expression was used by Lobban *et al.* to determine the thermodynamic implications of their diffraction data. As seen from the inset, the entropy of the low-temperature ice IX phase calculated from our simulations is in very good agreement with the entropy predicted from Howe and Whitworth's expression. Nagle's expression overestimates the entropy for partially disordered ice IX in agreement with previous analysis. [11] Both models, however, when asked to estimate the entropy of partially ordered ice III based on occupational probabilities α and β, significantly overestimate the configurational entropy. This test of the mean-field theories does not depend on the quality of our effective Hamiltonian, unless our model is somehow grossly atypical of the true Hamiltonian for this system (and we would argue, based on its agreement with experiment, it is at least qualitatively accurate). The mean-field theories are given the exact occupational probabilities for the model and should return a value close to the exact simulations, if accurate. We can also run the comparison in the opposite direction. Using the entropy calculated from our simulations, we use the Howe and Whitworth's expression to determine the occupational probability as a function of temperature. As shown in Fig. 4.5, α would have to be 25%, significantly lower than the results of our simulations, $\alpha = 38\%$, and experiment [12, 14] to yield the true entropy.

4.5 Discussion

A statistical mechanical theory of the ice III/IX transition is developed in this chapter. The structure of the low-energy phase and the transition temperature are both in qualitative agreement with experiment. Structural parameters, such as the bond distance and angles are in very good agreement with observed values. Our theoretical methodology has been previously shown to provide an accurate description of the ice VII/VIII phase transition and the ice Ih/XI transition. [19] It has also been used to predict the low-temperature fully-ordered form of ice VI [23].

The ice III/IX transition was recently treated by Kuo [102], who concludes based on methodology identical to ours that the previously reported ice IX structure is not the lowest H-bond isomer for this system. Unfortunately, this conclusion is based on failure to converge the calculations and to extrapolate to the infinite-system limit. Kuo only considered the $\Gamma-$point energy of a small unit cell. In this work we have shown that using either a larger unit cell or extended $k-$point sampling of the small unit cell reverses Kuo's conclusion. We find that the previously observed ice IX structure [9, 14] is the lowest-energy structure when calculations are properly converged. However, it must be realized that these calculations are dependent on the accuracy of the BLYP density functional, albeit one that has been remarkably successful in predicting the properties of other ice phases [19, 68, 103]. Therefore, while using higher order methods might affect the results, we can definitely say that Kuo's conclusion concerning the ground state using the BLYP functional was an artifact of only using the $\Gamma-$point of a small unit cell. Finally, we note that using only a small unit cell only gives a hint of the true thermal properties of the system, for example, a rounded heat capacity peak that extends to room temperature [102]. Extrapolation to the

thermodynamic limit using graph invariants is needed to reveal the character of the phase transition, the partial order in the high-temperature phase and partial disorder in the low-temperature phase.

Besides developing a theory that can reproduce observed behavior, this work also suggests a resolution of an apparent discrepancy between diffraction [9, 12, 14] and calorimetric [85] experiments. Thermodynamic data has been inferred from diffraction data using mean-field theories [11, 87, 98–100] that relate the system entropy to hydrogen-site occupations. Because we have a full statistical mechanical model of ice III and ice IX, we can compare the exact entropy from this model with the entropy that would be predicted on the basis of these mean-field theories. We find that all existing mean-field theories significantly overestimate the entropy of the disordered ice III phase. When used to interpret diffraction data [12, 14], they imply a value for the transition entropy that is too large. The transition entropy obtained from our calculation is in better agreement with the value reported from the calorimetric experiments of Nishibata and Whalley [85]. Further correcting our calculations for the change in unit cell dimensions should bring the results in closer agreement with experiment. We assumed that the unit cell does not change from ice III to ice IX. Since ice IX is actually more dense than ice III, we underestimate the Gibbs free energy of our ice IX phase. Correcting for this will destabilize the low-temperature phase and consequently reduce the transition temperature. As can be seen from Fig. 4b, this will further narrow the entropy gap between the two phases at the transition.

In conclusion, from application of graph invariants and DFT calculations on small unit cells, the energy differences in H-bond fluctuations for a large simulation cell could be calculated. A first-order phase transition to the proton-ordered

anti-ferroelectric ground state (Figure 4.2) was observed near 126 K. Partial H-bond ordering was observed over a range of temperatures above the transition with the occupational probabilities, α and β, reaching 38% before the transition. The low-temperature structure, partially disordered near the transition, transformed to fully ordered ice IX at lower temperatures.

CHAPTER 5

HYDROGEN BOND ORDERING IN ICE V AND THE TRANSITION TO ICE XIII

5.1 Introduction

Most of the currently known phases of ice can be grouped into pairs. [1] The subject of this chapter is one of the latest pairs to be discovered, ice V and ice XIII. [25, 104, 105] In each pair of ice phases, the oxygen atoms sit at virtually the same position. The orientation of the water molecules, while constrained to tetrahedral bonding directions, are disordered in the high-temperature member of the pairs because there are six ways that the two hydrogens of each water can be placed along four tetrahedral directions. In the low-temperature counterpart, the system condenses into one hydrogen bonding arrangement. The known order-disorder pairs of ice phases are ice Ih and XI [2–7,11,17,34,80,106], ice VII and VIII [42,44–49], ice III and IX [14,84,85], and, most recently, ice V and XIII and ice XII and XIV [25,104,105]. The complexity of the phase diagram of water, as evident in the continuing discovery of new phases of ice, results from the interplay between hydrogen bonding interactions and the tendency to pack efficiently in the crystal. Besides the need to understand the properties of water on earth and other planets, understanding of the behavior

of ice provides insight into forces between water molecules that can be applied in a variety of materials and biological applications.

In 2006, the proton-ordered version of ice V, ice XIII, was first reported by Salzmann *et al.* [25] Unlike the ice Ih/XI transformation [17,34,80–82], where doping with hydroxide enables formation of ice XI near 72 (76)K for H_2O (D_2O), ice V reversibly transforms to ordered ice XIII in the presence of excess protons in the form of HCl dopant [25, 104, 105]. In both cases, dopants presumably facilitate hydrogen bond rearrangements enabling a phase transition that otherwise has prohibitive activation barriers. No ordering of ice V was observed when pure ice or samples doped with hydroxide were cooled. Using Raman spectroscopy and monitoring the change in lattice parameters, the ordering transition was found to be reversible. [25, 104, 105] When cooling samples of ice V, the beginning of the ordering transition occurred near 117 K and upon heating ice XIII, it started near 108 K. [104] The unit cell of ice V, containing 28 water molecules, is monoclinic, space group A2/a, as determined by X-ray and neutron diffraction techniques. [12, 107, 108] The unit cell of ice XIII, also containing 28 water molecules, is monoclinic with space group $P2_1/a$, a reduction in symmetry from the ice V space group.

The region of stability for proton-disordered ice V is 210−270 K and 3.4−6.3 kbar. [12] Similar to ice III [12, 14, 85], there exists some degree of partial ordering of the protons in ice V. Results from infrared [96] and dielectric [109] studies were only able to indicate that ice V was proton disordered, not the degree of the disorder. A neutron diffraction study on single crystals of ice V, recovered to ambient pressure, indicated some proton sites had larger probabilities of being occupied than others at 110 K. [108] Recently, neutron diffraction experiments on ice V conducted in its region

of stability has shed light onto the degree of partial order. [12] Lobban, Finney, and Kuhs have measured lattice constants and occupation probabilities from 100−254 K at 5 kbar. [12] They found no evidence of a transition to an ordered structure with $P2_1/a$ symmetry which was first proposed by Kamb and LaPlaca [91] and later supported with calorimetric evidence by Handa, Klug and Whalley [110]. (The ordered phase eventually characterized by Salzmann *et al.* does indeed possess $P2_1/a$ symmetry.) In their work, Lobban *et al.* only observed a gradual ordering of the protons, not a change in the space group which is necessary for a transition to an ordered H-bond configuration. Johari and Whalley discussed these results in the context of dielectric studies on ice V and agreed that partial anti-ferroelectric ordering occurs as the temperature of ice V is lowered. [111]

Due to the size and symmetry of the ice V unit cell (Fig. 5.1), there are a large number of possible H-bond configurations. There are 69380 symmetry-distinct H-bond configurations possible for the 28-water unit cell. There are even 35 symmetry-distinct possibilities possessing the same space group as the experimental ground state. The complexity of the ice V and XIII structures makes analysis and prediction of ordering and partial ordering a daunting task. Lobban *et al.* [12] have remarked that, "the factors responsible for the partial order cannot be easily identified for such a complicated structure." Salzmann *et al.* have stated [25], "It would be a challenging test of the ability of modern day computational methods to reproduce our experimentally found lowest energy state." While not reducing the behavior of ice V and XIII to any simple rule, we demonstrate in this work that theoretical methods can indeed describe partial ordering of ice V and the transformation to ice XIII. We find that among the numerous, nearly degenerate, low-lying H-bond isomers of the

ice V unit cell, calculated using periodic DFT, that the ground-state configuration corresponds to that of the experimental ice XIII structure. In section 5.2, we discuss results of applying the graph-invariant approach to the ice V unit cell. Periodic DFT calculations are described in section 5.3 for H-bond configurations in two unit cells of ice V containing 28 and 112 water molecules respectively. In section 5.4, we discuss results from statistical mechanical calculations on a simulation cell containing 6048 water molecules. Besides calculation of the transition to fully ordered ice XIII, we observe a subtle second-order transition to a partially ordered phase that would be difficult to observe in experiments. We also calculate occupation probabilities (order parameters) that quantify the degree of partial ordering in ice V and compare these calculated quantities to experimental data.

5.2 Graph Invariants for Ice V

In phases of ice where water molecules are hydrogen-bonded to four others in a tetrahedral arrangement, there are six ways that a water molecule can be oriented at each lattice site. [15] Once one molecule is fixed, the possible arrangement of its neighbors is restricted by the Bernal-Fowler ice rules [101], which simply require that each water simultaneously donate two hydrogen bonds and accept two hydrogen bonds. Pauling [15] produced a remarkably accurate estimate for the number of H-bond arrangements available in ice Ih after imposition of the ice rules, $\left(\frac{3}{2}\right)^N$, where N is the number of water molecules. The exact result is $(1.5069)^N$ [10, 112]. The number of H-bond arrangements in ice V is given by the same expression.

The H-bond arrangements in ice are separated by only $\sim$0.1 kcal mol^{-1} per water in the ice phases (see Fig. 5.3 for ice V), leading to almost complete disordering

at the high-temperature stability edge of the solid. Depending on the ice phase, partial ordering can occur as the temperature is lowered. Also, of all the known high-temperature phases that coexist with liquid water − Ih, III, V, VI and VII in order of increasing pressure − a transition from an H-bond-disordered phase to a fully ordered phase has been discovered for all except ice VI [23] as the temperature is lowered.

To date, we have found that including up to second-order graph invariants constructed from bonds that are either neighbors or next-nearest neighbors is sufficient to parametrize the subtle energetics of ice lattices. In the previous chapters, this method has been used to successfully calculate H-bond ordering and phase transitions in ice Ih/XI [19, 20], ice VII/VIII [19, 20], ice III/IX [24], and to make a prediction of the H-bond-ordered phase derived from ice VI [23]. To fix the overall constant E_0 and the coefficients of the graph-invariant functions, $\{\alpha_r, \alpha_{rs}\}, \ldots$, we require the energies of some H-bond configurations as input. We have used relatively modest periodic DFT calculations, such as those using the BLYP functional [72, 73], as input. We have documented that the small energy differences in ice are not sensitive to the density functional or basis set used in the calculations. [19, 20, 113] Tribello and Slater [114] have provided insight into why relatively modest levels of DFT are successful in describing the energetics of H-bond arrangements in ice. They showed that the energy differences were insensitive to the choice of gradient-corrected functional because the energy differences between H-bond isomers largely depended on electrostatic interactions. Ideally, Eq. (4.1) should be a *free* energy expansion that incorporates the vibrational free energy of each H-bond arrangement. In all of our work to date, we have made the assumption, evidently justified by comparison with experiment, that

the vibrational free energies of the H-bond isomers are nearly the same and can therefore be neglected. The same assumption seems to be justified for ice V/XIII, as shown in section 5.4.

There are eight sets (orbits) of bonds related by symmetry in the unit cell of ice V. Application of the projection operator $\hat{G}$ to members of the same orbit will necessarily generate the same invariant. Thus a maximum of eight first-order invariants is possible by application of the projection operator. Application of the projection operator onto two of the bond orbits gives zero, leaving six non-trivial first-order invariant functions. Application of the projection operator onto bond pairs, $\hat{G}(b_r b_s)$, generates 226 unique, linearly-independent second-order invariants. The number of unique invariants generated for the ice V primitive cell is substantially larger than for any other system studied to date. The runner up is the primitive cell of ice III, 12 water molecules with space group $P4_12_12$, only possessing 45 second-order invariants.

When evaluated for values of the bond variables allowed by the ice rules, some of these invariants have values which are linearly dependent on other invariants. A simple example of this arises when the projection operator acts on the square of one bond, $\hat{G}(b_r b_r)$. This generates invariants which are the sum of squared bond variables for each orbit. These invariants could be used to count the number of defects (e.g. D- or L-defect) if such configurations were considered, but for ice without such defects these invariants evaluate to the number of bonds within an orbit for all configurations. Their contribution to the expansion in Eq. (4.1) is equivalent to the constant E_0. We speak of "eliminating linearly-dependent invariants" when, more precisely, we are eliminating invariants which are dependent on others over the restricted set of configurations allowed by the ice rules. When evaluated for 94 H-bond configurations

in the 28-water cell of ice V, 165 graph invariants were linearly dependent leaving 3 first-order and 57 second-order linearly independent invariants to describe scalar physical quantities. Invariants which evaluated to a constant were removed while the remaining invariants were sorted into groups based on bond types and distance between the generating bond pair. In previous studies, we have found that a good fit of the H-bond topology to energy only required those invariants generated by nearest-neighbor bonds. Next, invariants from the linearly independent set were eliminated if their contribution to the energy fit was negligible. For ice V, we found that an overall good fit to the energy was achievable using approximately 10 invariants. However, the predicted ordering of the low-energy isomers was a difficult property to converge without using more invariants, as discussed in the next section. Those invariants which were significant are given in Tables 5.1 and 5.2. We report coefficients for two models for reasons discussed in the next two sections.

The space group symmetry of the ice V structure permits the use of five occupation probabilities, or order parameters, that describe the probability of protons being on one or the other side of a particular hydrogen bond (Fig. 5.1). The order parameters have traditionally been designated by the first five Greek letters, α, β, γ, δ, and ϵ, and range from 0 to 1 in an obvious way where $\frac{1}{2}$ indicates equal probability of the H-bond pointing in two possible directions. As might be expected, the occupation probabilities are strongly related to some of the graph invariants. Due to the symmetry of the ice V phase, the H-bonds described by the ϵ parameter are forced to be fully disordered, i.e. $\epsilon = \frac{1}{2}$. Thus the two first-order invariants generated by ϵ type bonds are the ones that were found to be identically zero using the full symmetry group of the high-temperature ice V phase. The invariants associated with

ϵ bonds assume non-zero values below the phase transition where the ice V symmetry is broken. Naturally, these invariants do not contribute to the Hamiltonian, which must have the full symmetry of the ice V system. Bonds of the α and γ type are each associated with two first-order invariants (and hence the notation α_1, α_2 and γ_1, γ_2 in the next section, where further discussion is given), while β and δ are each described by a single first-order invariant.

5.3 Periodic DFT and Parametrization of Graph Invariants

Investigating the degree of proton disorder in ice V, Lobban, Finney and Kuhs measured lattice constants over a wide temperature range, observing changes of $\sim$0.02$-$0.03 Å and $\sim$0.1° at temperatures above 200 K. Lattice constants used in the present calculations were taken from data at 5.0 kbar and 198.9 K: a=9.0847, b = 7.5099, c = 10.2328 Å, and β = 109.19°. [12] Geometry optimizations were performed on H-bond isomers for unit cells containing 28 and 112 water molecules using the CPMD [69–71] program with periodic boundary conditions. We employed the BLYP gradient correction [72, 73] to the local density approximation, Troullier-Martins norm-conserving pseudopotentials [74], and plane wave cutoffs ranging from 70$-$150 Ry in the DFT calculations. Sampling of the Brillouin zone was restricted to the $\Gamma-$point, which we have shown in previous chapters is sufficient for systems containing more than $\sim$30 water molecules.

As discussed above, the symmetry of the ice V unit cell permits the degree of proton order to be captured by five occupation probabilities. The parameters α, γ, and ϵ are each described by bonds which belong to two separate orbits, thus there are two contributions. When the ice rules are strictly obeyed, the two contributions

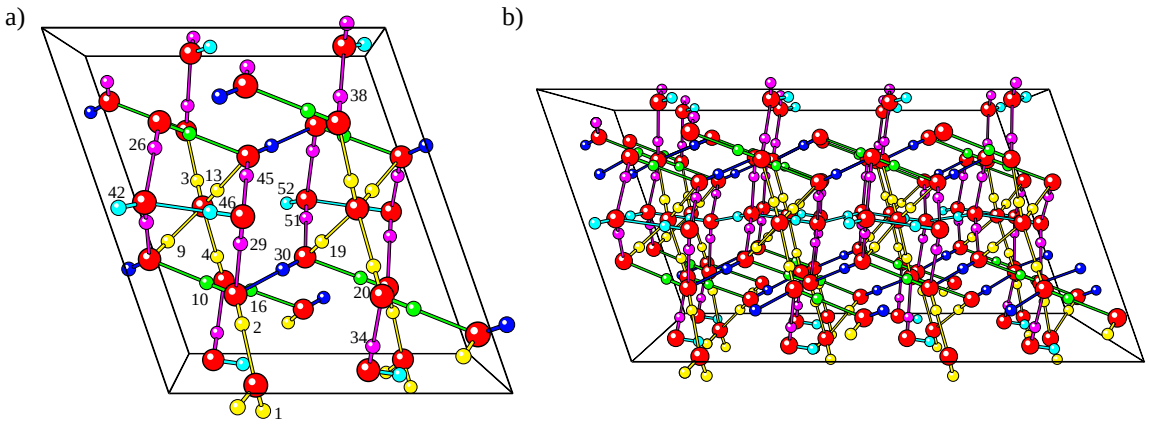

Figure 5.1: H-bond configurations of two unit cells, as viewed down the $b-$axis, used in periodic DFT calculations, discussed in section 5.3, containing 28 and 112 waters respectively. The larger atoms are oxygens and the smaller atoms are hydrogens. Hydrogens related by symmetry and thus contributing to the same order parameter are similarly colored: α (yellow), β (green), δ (blue), γ (violet), and ϵ (turquoise). The configuration shown here is the ground state at a plane wave cutoff of 90 Ry or higher, which corresponds to the experimentally determined proton-ordered ice XIII. The labels in (a) identify those bonds used to generate graph invariants as described in Tables 5.1 and 5.2. The thin black lines outline the monoclinic cell.

to α are always identical, and similarly for γ. The two parameters that contribute to ϵ, which we label ϵ_1 and ϵ_2, however, can differ and they in fact do so as discussed in the next section. When labeling the bond types for the generating bond pairs in Tables 5.1 and 5.2, we signify the bond type with a subscript identifying which orbit to which those bonds belong. Since the two first-order invariants that contribute to α and γ have the same values for all configurations in which the ice rules are obeyed, the first-order invariants arising from projecting onto bonds 19 or 45 in Tables 5.1 and 5.2 are listed as contributing to either order parameter.

There are 69380 symmetry-distinct H-bond configurations possible in the primitive unit cell of ice V, enumerated using previously described methods. [50, 51, 68] There

are 35 symmetry-distinct configurations which have the same space group $P2_1/a$ as proton-ordered ice XIII, determined using the FINDSYM [8] program. Since it is not realistic to perform periodic DFT calculations on all of these realizations, we "semi-randomly" selected isomers for geometry optimization. We first performed calculations on a handful of configurations, parametrized a graph-invariant expression for the energy, and then using the predicted energies, chose additional configurations for further calculations. This procedure of selecting additional H-bond isomers was then continued until a thorough sampling of the energy range was obtained and the coefficients of the invariants in Eq. (4.1) did not change upon adding more configurations to the fit used to determine those coefficients. We also included all low-energy configurations to identify the ground state H-bond configuration. As shown in the plots of Fig. 5.3, a number of configurations lie very close in energy to the ground state.

The ground-state configuration obtained using a plane wave cutoff of 70 Ry does not agree with the experimental structure. The configuration corresponding to ice XIII was the fifth lowest-energy configuration lying 2.3 K (4.6×10^{-3} kcal mol^{-1}) per water above the ground state, Fig. 5.2d. However, increasing the plane wave cutoff switched the energetic order of the low-lying isomers bringing the ground state configuration into agreement with experiment. The previous ground state configuration was now the second lowest-energy configuration lying 1.2 K per water higher in energy. The ice XIII configuration remained the lowest-energy isomer when the plane wave cutoff was increased to 120 and 150 Ry, although there were some changes in the energetic ordering of the low-lying configurations. Regardless of the plane wave cutoff, the same group of $\sim$20 H-bond configurations appeared within 10 K per water

of the ground state. Increasing the plane wave cutoff changed the order of these configurations, but did not bring other higher-lying configurations into this group. We also performed preliminary tests with the PBE [115] and revPBE [116] density functionals. Again, the group of energetically low-lying isomers remained intact, although the ordering within the group was sensitive to the functional. The ice XIII structure was the ground state using the PBE functional when the calculation was adequately converged (cutoff $>$ 120 Ry). Using the revPBE functional, the ice XIII structure was 0.9 K per water above the lowest-energy isomer. For other ice systems studied to date, no more than two configurations were identified lying within that energy range above their corresponding ground state. For the case of ice VI, for which an ordered version has yet to be identified experimentally, the ground state energy gaps for the 2nd and 3rd lowest configurations were 4 and 10 K per water respectively. [23]

The energetically low-lying configurations shown in Fig. 5.2 are obtained from the ground state by flipping several closed loops of H-bonds, the same operation used to generate trial moves in the Monte Carlo algorithm discussed below. Bonds of the ground state configuration that are conserved in all the energetically low-lying configurations are shaded in blue in Fig. 5.2a (see caption). Configuration (c) is obtained after flipping four loops consisting of five bonds each. In Fig. 5.2c, two of the loops are entirely contained in the middle of the unit cell while the other two loops are split across the cell boundary where periodic boundary conditions are enforced. These 5-membered loops each contain two bonds that contribute to the α order parameter, two to the γ order parameter, and one to ϵ. They occur in the sequence $\alpha_2 - \alpha_2 - \gamma_2 - \epsilon_1 - \gamma_2$. In the ice XIII structure, the two α bonds in this loop have opposing contributions to the α order parameter. Hence, flipping this loop to go

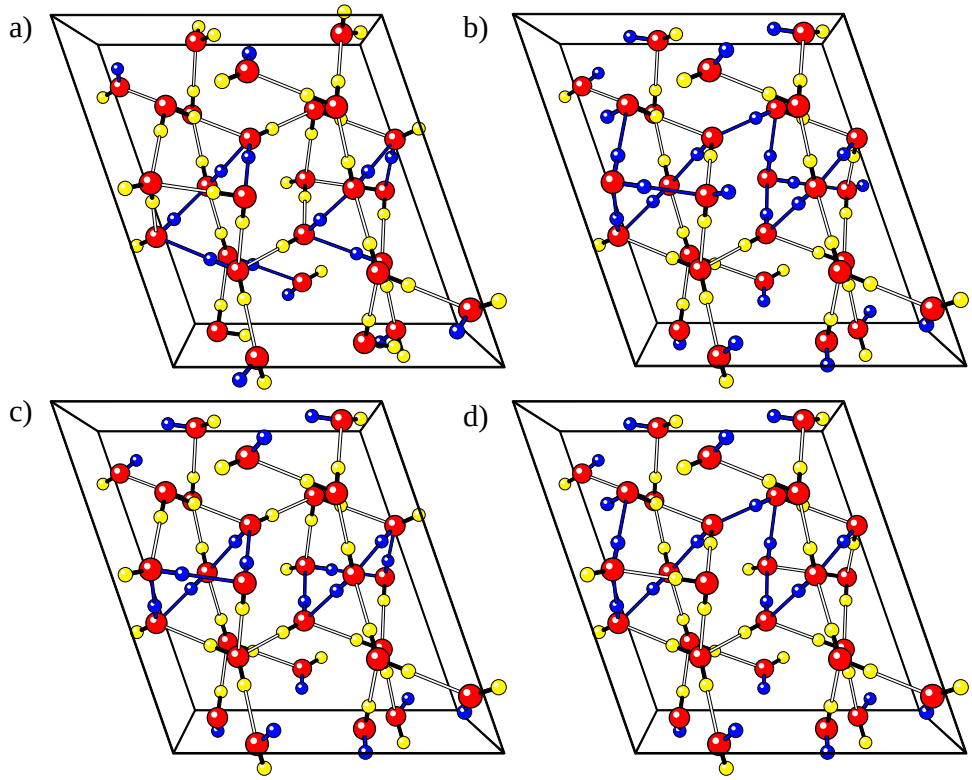

Figure 5.2: Four lowest-energy H-bond configurations of the 28-water unit cell of ice V determined by calculations at plane wave cutoffs of 90 and 120 Ry using the BLYP density functional. The larger atoms are oxygens and the smaller atoms are hydrogens. In panel (a), H-bonds whose orientation is conserved in all the energetically low-lying isomers are shaded in blue. To some extent, this is arbitrary because, in general, several symmetry-equivalent versions of each configuration may be compared with the ground state. The shaded bonds in panel (a) are based on choosing excited configurations that maximize the number of conserved bonds relative to the ground state, not always the configuration shown in panels (b,c,d). In panels (b,c,d), H-bonds that are flipped with respect to the ground state configuration (a) are shaded in blue. Panels (b,c,d) show the configurations lying 2.3, 2.5, and 2.6 K per water, respectively, above the ground state with a plane wave cutoff of 120 Ry. The corresponding energies from calculations at 90 Ry are 1.7, 2.1, and 1.2 K per water.

from the configuration of Fig. 5.2a to Fig. 5.2c does not change the value of α. The same is true for the two γ bonds and the γ order parameter. Hence, only the ϵ order parameter is altered. In principle, this could be used as an experimental signature of this excitation. However, we find that the population of such excitations is quite small in the ice XIII phase. Configurations (b) and (d) are each obtained by flipping two loops of this sequence as well as several other bonds. In configuration (b), two loops of type $\alpha_2 - \alpha_2 - \delta - \gamma_1 - \epsilon_1 - \epsilon_2 - \gamma_2$ are flipped while for configuration (d) a single loop of $\alpha_2 - \alpha_2 - \delta - \gamma_1 - \gamma_2 - \alpha_2 - \alpha_2 - \delta - \gamma_1 - \gamma_2$ is flipped. In configurations (b) and (d), changes in the γ, δ, and ϵ occupation parameters occur. Although $\alpha-$type bonds were flipped, all of the low-lying configurations had the same value for the α order parameter as the ground state by the same mechanism described in connection with the configuration in Fig. 5.2c. Reversal of β bonds was relatively rare in the $\sim$20 low-lying configurations. Only three low-lying configurations were obtained after flipping β bonds which resulted in a change of that order parameter.

The ability of the graph-invariant expansion in Eq. (4.1), using those invariants listed in Table 5.1, to fit the energies of the isomers of the primitive unit cell is evaluated in the left column of Fig. 5.3 for two different models. If a perfect fit was achieved, all points would lie on the diagonal. As can be seen from the figure, the typical errors in fitting the energies is a small fraction of the energy range. However, these differences become important when trying to describe the nearly degenerate set of isomers which lie close in energy to the ground state. An overall good fit to the energy required only 10 invariants, but in order to sufficiently describe the energetic ordering of low-lying isomers, additional invariants were necessary. Thus, half of the coefficients used in the models had magnitudes in the range $0.001-0.01$ kcal mol^{-1} per

Generating bonds	Distance(Å)	Occupancy parameter	model 1		model 2	
			90 Ry	120 Ry	90 Ry	120 Ry
2,19	2.76	α_1,α_2	0.0120385	0.0117782	0.00644397	0.00619219
9,19	3.55	α_2,α_2	−0.0021314	−0.0021849	−0.00526965	−0.0052024
10,19	3.55	β,α_2	0.0154397	0.0150414	–	–
1,30	2.77	α_1,δ	0.0142382	0.0146183	0.0134419	0.0137168
2,34	3.51	α_1,γ_1	−0.0149567	−0.0154769	−0.0118619	−0.0129105
10,52	2.80	β ,ϵ_1	0.0139424	0.0141327	–	–
3,51	3.51	α_1,γ_2	0.0078866	0.0077727	0.00456332	0.00459766
13,51	3.51	α_2,γ_2	0.0105991	0.0112825	0.0110774	0.0119336
16,51	3.33	β ,γ_2	−0.0079029	−0.0079268	–	–
10,45	3.90	β,γ_2	0.0050779	0.0053086	0.0110158	0.0110525
46,51	2.78	ϵ_2,γ_2	0.0133983	0.0139472	0.0106671	0.0104636
4,29	3.14	α_1,γ_1	–	–	−0.00014175	0.00014839
10,29	0.00	β,γ_1	–	–	0.0121478	0.0116609
20,52	2.82	β,ϵ_1	–	–	−0.0181417	−0.0185411
26,52	2.71	γ_1,ϵ_1	–	–	0.0076593	0.0079862
38,52	3.14	γ_1,ϵ_1	–	–	−0.00318216	−0.00263071
42,52	2.71	ϵ_1,ϵ_1	–	–	−0.00034917	−0.00046292
9,51	3.51	α_2,γ_2	–	–	0.00499258	0.00491852
45,46	0.00	γ_2,ϵ_2	–	–	−0.00762639	−0.00664159
19	–	α_1 or α_2	0.0427572	0.0428228	0.0400461	0.0402459
10	–	β	0.0418449	0.0419556	0.0415911	0.041752
45	–	γ_1 or γ_2	0.0154168	0.0133746	0.0198209	0.0177913

Table 5.1: Geometrical features and contributions to the description of the energy of H-bond isomers in the primitive unit cell containing 28 water molecules. The indices of the generating bond pair refer to Fig. 5.1. The distance associated with each bond pair is the distance between the closest vertices from each bond in an idealized structure before geometry optimization. The occupancy parameters to which each bond contributes are identified. The next two columns give the fitting coefficients for each invariant used in Eq. (4.1) for the energy, in units of kcal mol^{-1} per water, for the first model for plane wave cutoffs of 90 and 120 Ry. The last two columns contain similar data for the second model.

Generating bonds	Distance(Å)	Occupancy parameter	model 1		model 2	
			90 Ry	120 Ry	90 Ry	120 Ry
2,19	2.76	α_1,α_2	0.00873907	0.00855733	0.00618326	0.00648071
9,19	3.55	α_2,α_2	−0.00868823	−0.00893164	−0.00944809	−0.0104118
10,19	3.55	β,α_2	0.00419561	0.00430824	–	–
1,30	2.77	α_1,δ	0.0150852	0.014914	0.0197974	0.0194143
2,34	3.51	α_1,γ_1	−0.00797234	−0.00856979	−0.00732364	−0.00767692
10,52	2.80	β ,ϵ_1	0.00614274	0.00477601	–	–
3,51	3.51	α_1,γ_2	0.00784255	0.00786155	0.00573805	0.00571859
13,51	3.51	α_2,γ_2	0.00869924	0.00929597	0.0120731	0.0131678
16,51	3.33	β ,γ_2	0.00581676	0.00582805	–	–
10,45	3.90	β,γ_2	0.0125182	0.0120234	0.012123	0.0112275
46,51	2.78	ϵ_2,γ_2	0.0120792	0.0115931	0.0126021	0.0114718
4,29	3.14	α_1,γ_1	–	–	−0.00368077	−0.00437427
10,29	0.00	β,γ_1	–	–	0.00691887	0.00668232
20,52	2.82	β,ϵ_1	–	–	−0.0133792	−0.0119001
26,52	2.71	γ_1,ϵ_1	–	–	0.0164779	0.0150925
38,52	3.14	γ_1,ϵ_1	–	–	0.00432525	0.00419826
42,52	2.71	ϵ_1,ϵ_1	–	–	0.00500769	0.00518427
9,51	3.51	α_2,γ_2	–	–	0.00652325	0.00721475
45,46	0.00	γ_2,ϵ_2	–	–	−0.0164089	−0.0141192
19	–	α_1 or α_2	0.0387347	0.0388697	0.0446275	0.0443862
10	–	β	0.0439473	0.0446142	0.0436782	0.0444514
45	–	γ_1 or γ_2	0.0185417	0.016885	0.012622	0.0110797

Table 5.2: Geometrical features and contributions to the description of the energy of H-bond isomers in a unit cell, measuring $2 \times 2 \times 1$ primitive cells on each side, containing 112 water molecules. A description of the columns and their contents is identical to that given in Table 5.1.

water, ten times smaller than typical in ice systems. We used two models, differing in their description of the low-lying isomers, to test the sensitivity of the predicted thermodynamic properties to the graph-invariant expression. As seen in the Tables 5.1 and 5.2, the models have a number of common invariants between them with model 2 possessing more invariants generated by ϵ type bonds.

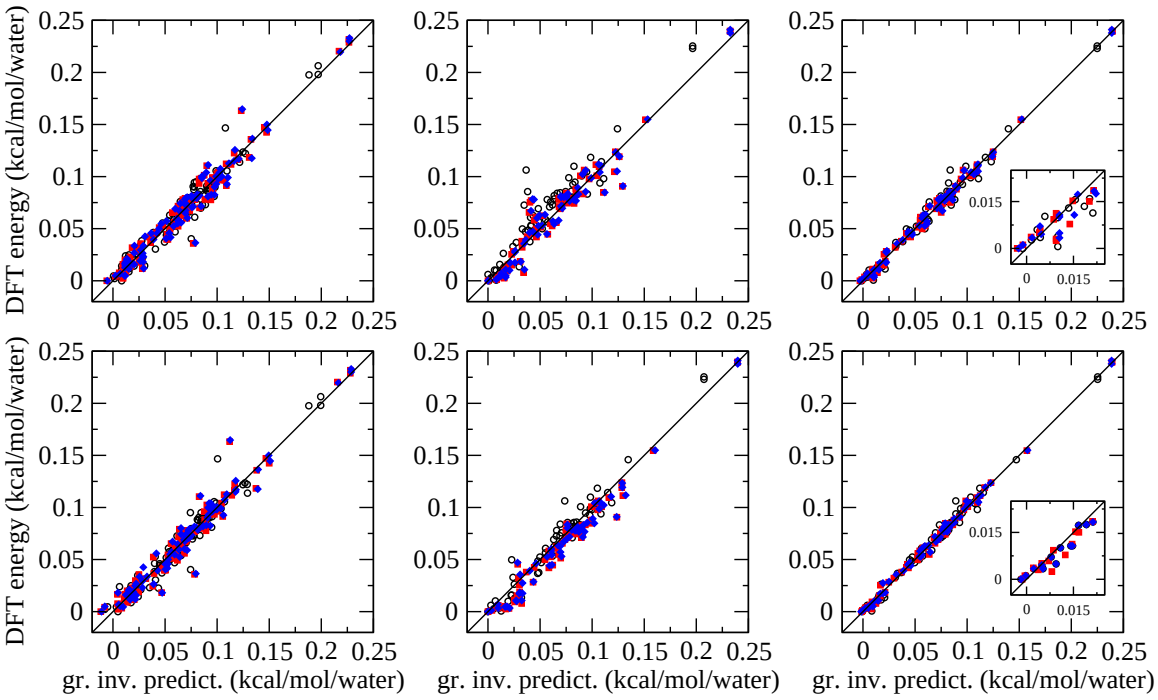

Figure 5.3: Test of the ability of the graph invariant expansion, Eq. (4.1), to fit the energies of H-bond isomers of ice V at various plane wave cutoffs: 70 Ry(○), 90 Ry(■), and 120 Ry(♦). The top row shows results using model 1 while the bottom row shows results for model 2, as defined in Tables 5.1 and 5.2. The left column shows the fit of energies for 94 H-bond configurations in the 28-water unit cell. The middle column shows the ability of parameters derived from the 28-water cell to predict the energies of 61 H-bond configurations in the 112-water cell at the same plane wave cutoff. The right column shows the fit of energies to the 112-water cell. The insets show the performance of the graph invariant fit for the lowest-energy configurations. In all plots, a line of slope unity is shown to indicate where points would lie for perfect agreement.

We next calculated the DFT energies for 61 isomers, chosen "semi-randomly" using a similar procedure as described above, for a larger 112-water cell measuring $2 \times 2 \times 1$ primitive cells on each side. Similar to the small cell calculations, the ground-state configuration only agreed with the experimental structure at plane wave cutoffs of 90 Ry and higher. The second lowest-energy configuration in the large cell, corresponding to Fig. 5.2c from the small cell, was now found to lie 0.58 (0.57) K per water above the ground state at a plane wave cutoff of 90 (120) Ry. We can test the performance of Eq. (4.1) by using the coefficients from the 28-water cell to predict the energies of the 112-water cell, as shown in the middle column of Fig. 5.3. As shown in the figure, the coefficients from the small cell do a good job of predicting the energies. In our previous calculations for the ice Ih/XI system, small systematic deviations were observed when we predicted energies of a larger cell based on invariant coefficients derived from a small unit cell. [19,20] In that case, the small deviations are attributed to insufficient $k-$point sampling because only the $\Gamma-$point was employed for the smallest unit cell. No such deviations using only the $\Gamma-$point are observed here, suggesting we have probably already reached convergence with respect to $k-$point sampling because our smallest cell is already fairly large. Overall, both models provide a good description of the energetics, but model 2, which includes more invariants, gives a better prediction of the low-lying isomers. Reparametrizing the graph-invariant expression using coefficients obtained from the 112-water cell leads to an effective Hamiltonian for describing H-bond fluctuations in a large simulation cell, as discussed in the next section.

5.4 Statistical Mechanical Results

Metropolis Monte Carlo simulations were performed on a simulation cell measuring six primitive unit cells on each side, containing 6048 water molecules. The invariant coefficients, shown in Table 5.2, obtained from the 112-water unit cell at a plane wave cutoff of 120 Ry were used to evaluate Eq. (4.1) for both models. Simulations were performed for both decreasing and increasing temperature. Trial moves were generated using the algorithm of Rahman and Stillinger [66] by reversing bond loops in which H-bonds point in the same direction that either close upon themselves in the same unit cell or in a periodic replica. The lowest-energy isomer, corresponding to the experimental ground state, was the starting configuration for the initial low-temperature simulation. The final H-bond configuration in a preceding simulation was always the initial configuration in the next simulation. A highly disordered configuration obtained from simulation at an extremely large temperature (10^7 K) was used to initialize the sequence of simulations decreasing in temperature.

Simulations of model 1 (columns 5 and 6 of Table 5.2) with decreasing temperature leads to a configuration very similar to the ground state, but higher in energy, with a transition temperature near 62 K. The precise transition temperature for model 1 was found by thermodynamic integration [20] which, as expected, places the transition in the middle of the very small hysteresis loop visible in Fig. 5.4. The configuration obtained would be the ground-state configuration if a single loop of 42 H-bonds were flipped. Flipping this loop is possible in our simulations, but such a trial move has an extremely small probability of being attempted and did not occur. Model 2 (columns 7 and 8 of Table 5.2) does freeze to the ground-state configuration near 69 K, 3 degrees below the thermodynamic transition temperature for model 2 as determined by

thermodynamic integration. The increasing and decreasing temperature sequences of simulations form a hysteresis loop of width 1 K for model 1 and 4 K for model 2, as shown in Fig. 5.4a. At temperatures above 100 K, both models closely resemble one another. Deviations between the models are most noticeable at temperatures below 100 K. Besides the first-order transition at 62 K, model 1 undergoes a minor second-order phase transition at 96.1 K associated with the ϵ order parameter. Probability distributions of the occupation parameters as a function of temperature provide insight into the additional second-order phase transition and is discussed below. Model 2 also goes through the same second-order phase transition, but at the lower temperature of 82.1 K and its effect on energy and entropy is not as evident as in model 1.

In Fig. 5.4b, the entropy is plotted as a function of temperature using data from model 2. The entropy of the low-temperature phase was calculated by thermodynamic integration from 0 K, and that of the high-temperature phase was integrated from infinite temperature. The entropy at infinite temperature is taken to be Nagle's result for the Pauling entropy for a fully disordered arrangement of H bonds in ice. [10] With decreasing temperature, 53% of configurational entropy is lost before the transition, 45% at the transition, and 2% after the transition. Recent calorimetric experiments have measured the change in configurational entropy at the transition to be 66% of the Pauling entropy. [117]

From the simulations, we can calculate occupation probabilities for each model. In Fig. 5.5, occupation probabilities as a function of temperature are compared with data obtained from the neutron diffraction studies of Lobban, Finney, and Kuhs. [12] At temperatures above 100 K, the order parameters from models 1 and 2 are

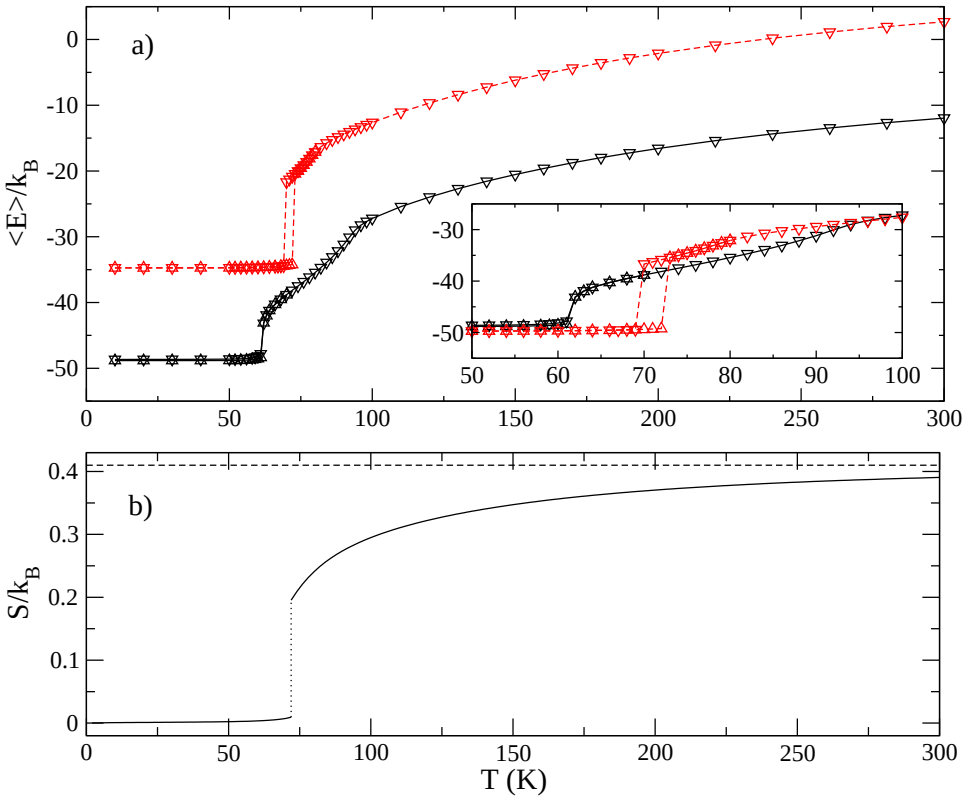

Figure 5.4: a) Average energy plotted as a function of temperature from Metropolis Monte Carlo simulations for a simulation cell of ice V containing 6048 water molecules. The solid curves are for model 1, and the dashed curves, shifted upward by 15 K for clarity, are for model 2. Energies are presented for a series of runs ascending and descending in temperature for both models, indicated by the upward and downward-pointing triangles, respectively. As can be seen, both models are very similar at temperatures above 100 K. The inset, where there is no shift in the data sets, focuses on the transition region for both models. b) Entropy plotted as a function of temperature obtained from simulations using model 2. The horizontal dashed line is the Pauling entropy for a fully disordered ice lattice. With decreasing temperature, 53% of the entropy is lost before the transition, 45% at the transition, and 2% after the transition.

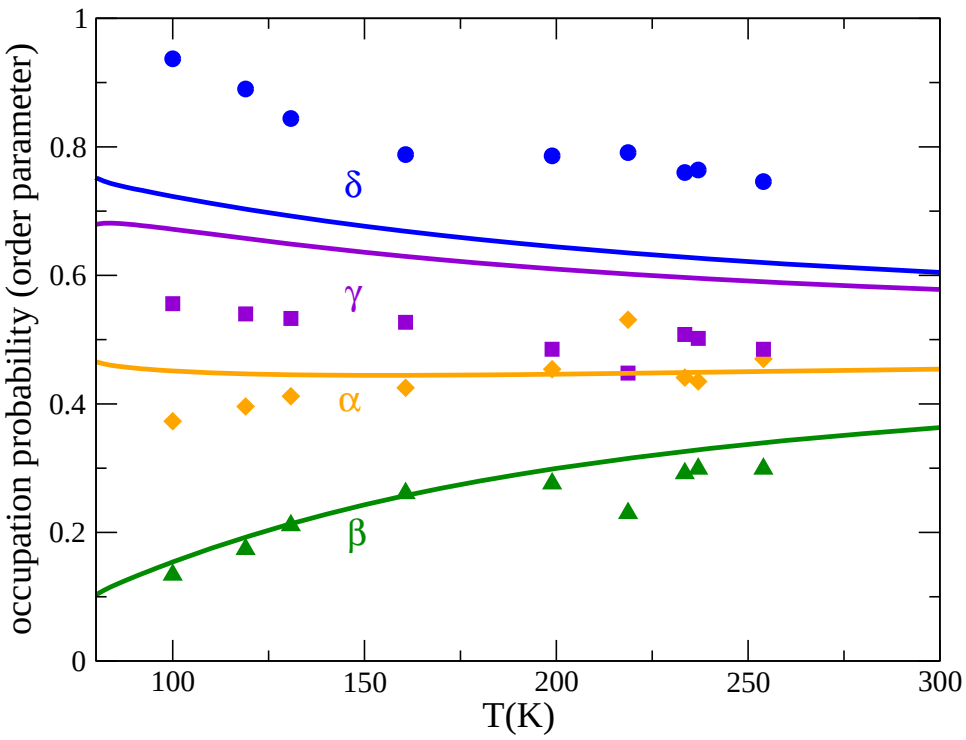

Figure 5.5: Occupation probabilities plotted as a function of temperature. The solid lines are data obtained from statistical mechanical calculations and the symbols are data taken from the neutron diffraction data of Lobban, Finney, and Kuhs. [12] The occupation probabilities from top to bottom are δ(●), γ(■), α(♦), and β(▲). Data from both models are nearly superimposable at temperatures above 100 K, thus only the data from model 2 is shown for clarity. The ϵ type bonds, also not shown, are fully disordered ($\epsilon = 0.5$) above 100 K, identical to experiment.

nearly superimposable. At high temperatures, all order parameters take the value $\frac{1}{2}$, corresponding to a fully disordered structure. The ϵ bonds, similar to experiment, remain fully disordered until the system approaches the transition temperature below 100 K. The ground-state configuration, fully ordered ice XIII, is described by the following occupation parameters: $\delta = \epsilon = 1$, $\alpha = \gamma = \frac{1}{2}$, and $\beta = 0$. (Actually, there are two symmetry-related configurations corresponding to the ground state in which $\epsilon = 0$ or 1 while all other parameters remain the same.) As discussed in section 5.3,

there are two orbits that contribute to α, γ, and ϵ respectively. Strict adherence to the ice rules, as done in the simulations, forces the contributions to α to be identical, and similarly for γ. However, the two contributions to ϵ, which must average to zero in the ice V phase, differ at lower temperatures where the ice V symmetry is broken. For both models, bonds of type ϵ_1 remain fully disordered until the transition to the ice XIII phase. Bonds of type ϵ_2, break ice V symmetry above the transition to ice XIII in the second-order phase transition.

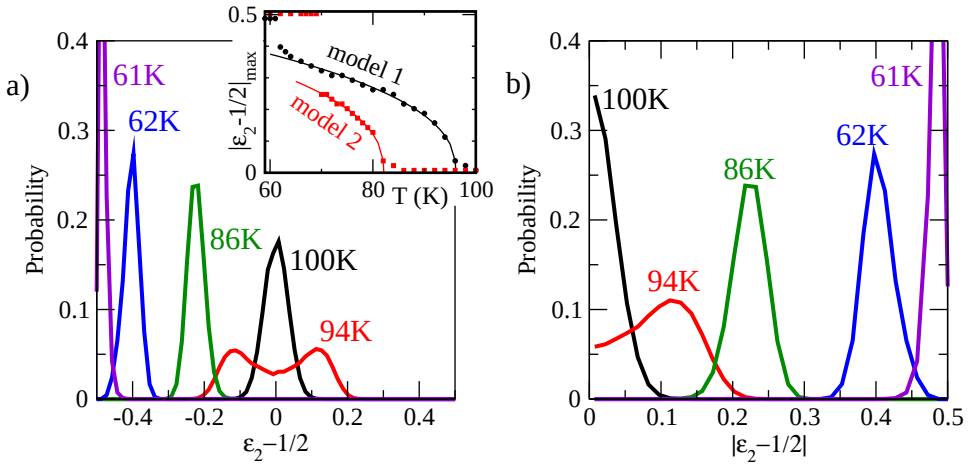

Figure 5.6: Probability distributions for a) $(\epsilon - \frac{1}{2})$ and b) $|\epsilon - \frac{1}{2}|$ for a series of temperatures, taken from simulations using model 1. In this series of simulations, the center of the probability distributions approach -0.5 and 0.5 respectively as temperature is decreased. The symbols in the inset show the peak probability locations as a function of temperature. The smooth lines are fits to that data using the scaling form of the order parameter given in Eq. (5.1).

The continuous nature of the phase transition associated with ϵ_2 is demonstrated in the probability distributions for $\epsilon - \frac{1}{2}$ in Fig. 5.6. Data for model 1 is shown, and model 2 exhibits similar behavior. Above the second-order transition temperature the parameter $\epsilon - \frac{1}{2}$ fluctuates about zero, as shown by the distribution for 100 K

in Fig. 5.6. Slightly below the transition, as depicted by the data in Fig. 5.6 for 94 K, the distribution in $\epsilon - \frac{1}{2}$ becomes bimodal and symmetric. The point where the probability distribution becomes bimodal, and the Landau free energy surface turns from single- to double-welled, is the critical temperature for the second-order phase transition [118, 119]. At 86 K and 62 K, the system has not yet condensed into the ice XIII phase, but the free energy as a function of $\epsilon - \frac{1}{2}$ is developing deeper and further-separated wells. In principle, the probability distribution in Fig. 5.6a at these temperatures should remain bimodal. However, the free energy barrier separating the wells at $\pm(\epsilon - \frac{1}{2}\ )$ is now too large to be surmounted for our simulation system and only a single peak is apparent. Of course, it is only because of the finite size of our simulation cell that the bimodal nature of the probability distribution could be seen in 94 K. In the thermodynamic limit, the system would be trapped in one of the wells at all temperatures below the critical point, constituting the mechanism of symmetry breaking of the second-order transition.

Further evidence for the second-order nature of the phase transition comes from the behavior of $\left|\epsilon - \frac{1}{2}\right|_{max}$, the location of the peaks of the probability as a function of temperature. $\left|\epsilon - \frac{1}{2}\right|_{max}$ is the equilibrium value of the order parameter in the thermodynamic limit ($N \to \infty$). Near a critical point, $\left|\epsilon - \frac{1}{2}\right|_{max}$ is expected to obey a scaling relation [118, 120],

$$\left|\epsilon - \frac{1}{2}\right|_{max} \propto |T - T_c|^{\beta} \ . \tag{5.1}$$

The inset near Fig. 5.6a shows $\left|\epsilon - \frac{1}{2}\right|_{max}$ as a function of temperature for models 1 and 2, and a fit to the data using the form in Eq. (5.1). The fit yields T_c values of 96.1 and 82.1 K for models 1 and 2, respectively. The critical exponent β, as determined by fitting Eq. (5.1) to the data, is 0.4104 and 0.4112 for models 1 and 2,

respectively. The similarity of the β values between the two models suggests that the models exhibit an identical mechanism for the phase transition.

5.5 Discussion

Judging by the size of the unit cell, the ice V/XIII system is the most complex of all the phases of ice. Despite the challenging nature of this system, using graph-invariant techniques [19, 20, 22–24, 51, 113] we have been able to construct a Hamiltonian for hydrogen bond fluctuations in ice V and XIII that successfully predicts the ordered phase and the nature of H-bond fluctuations in ice V.

Because of the size and complexity of the ice V and XIII crystal structures, relatively many parameters were needed to describe the dependence of energy on H-bond topology. The large set of parameters, established using periodic DFT calculations, are listed in Tables 5.1 and 5.2. (In contrast, a description of the energy differences of H-bond isomers in the ice Ih/XI system required only 3 parameters [19,20].) Because the description of H-bond energetics for ice V was so intricate, we investigated the properties that resulted from two different parameter sets. In this way, we attempted to provide some "error bars" on the predictions from our methods. Model 1 gave the correct ground state, but did not give the right energy ordering of configurations lying close to the ground state. Model 2 was more extensive and gave a representation of the low-lying configurations that was faithful to the DFT results.

The good news was that the energy and entropy (Fig. 5.4) and order parameters in the ice V phase (Fig. 5.5) were largely insensitive to the parametrization of the invariant coefficients in Eq. (4.1). The continuous phase transition that preceded the

first-order phase transition to ice XIII was found in both models 1 and 2. Quantitatively, the transition to ice XIII occurred 10 K lower in model 1. Also, a sequence of decreasing temperature simulations of model 1 became kinetically trapped in a configuration very close to the ground state while model 2 was able to find its way to the perfect ice XIII structure.

Perhaps the most gratifying comparison between theory and experiment in this work is contained in Fig. 5.5 where predicted and measured order parameters are plotted. Given the relatively modest BLYP level of DFT which was practical to use to parametrize our graph-invariant Hamiltonian, the very small energy differences that are at play here, and the assumptions made in our calculations (i.e. equal vibrational free energy of all the H-bond isomers), additional evidence that the graph-invariant Hamiltonian for H-bond fluctuations is meaningful is welcome. Fig. 5.5 shows that the H-bond energetics predicted by our model are at least qualitatively correct. Another source of confidence is the fact that our methods also make correct predictions for ice Ih/XI, III/IX, and VII/VIII. Experimentally, the ice V/XIII transition occurs between 108 and 117 K, 50 K higher than our theoretical predictions. Again, given the approximations and sources of error in the calculation of very subtle energetics, discrepancies of this magnitude are not surprising.

In our model of the ice V/XIII system, a second-order transition to a phase partially ordered with respect to the ϵ order parameter intervenes before ice V transforms to ice XIII. We describe the nature of this second-order transition to provide a complete description of our model, but it would be somewhat fortuitous if this transition would actually be observed in experiments. The effect of the phase transition on the average energy and entropy in Fig. 5.4 is barely noticeable. In fact, the reader

will note that many data points in Fig. 5.4 near the transition point were required to capture this effect. The phase that intervenes between ice V and ice XIII is the thermodynamically stable phase in our model over a very limited range of roughly 10 K. Since this behavior is controlled by extremely small energy differences, this behavior could easily be revised by, say, more accurate energy calculations. Perhaps it is most appropriate to take our calculations as a suggestion to look for enhanced fluctuations of the ϵ order parameter in the vicinity of the ice V/XIII transition.

The calculations presented in this work only concern equilibrium properties, not the dynamics of H-bond ordering. The mechanism by which defects promote the ordering transitions in ice is not yet understood, and this is the problem we investigate in the next chapter.

CHAPTER 6

STUDY OF A HYDROXIDE ION AND L-DEFECT IN A PROTON-DISORDERED Ih LATTICE

6.1 Introduction

One of the most difficult and intriguing aspects of ice physics is the behavior of defects. [1] Although defects have little effect on the statics of phase transitions, they are the key to understanding the dynamics and mechanism of phase transitions. For example, ice-Ih must be doped with hydroxide to catalyze the transition to ice-XI. [2–5, 17, 34, 80–82] The mechanism by which hydroxide (OH^-) catalyzes the ice-Ih/XI transition is not understood. [18, 121, 122] In fact, it is not even clear that hydroxide defects have significant mobility in this temperature range near 70 K. The structure and transport properties of defects is relevant to problems in environmental and atmospheric science [123] and glaciology. [1] In this work, we introduce techniques applicable to the study of ionic defects, H^+ and OH^-, and neutral defects, such as the OH radical, in ice. There is general agreement that ionic defects are immobilized on an accessible experimental time scale somewhere between 100 and 200 K. Beyond that, there is considerable disagreement, and seeming contradiction in the literature. Devlin and co-workers doped D_2O impurities into H_2O ice, or D_2O

impurities into H_2O ice. [27, 124–126] For the case of D_2O impurities in H_2O, passage of an ionic defect through the location of the impurity will lead to the formation of HOD molecules. Ionic defects diffusing through a D_2O molecule split that molecule into two neighboring HOD molecules, [27, 124–126] designated as $(HOD)_2$ in the Devlin group's work. Both Bjerrum and ionic defects are needed for further diffusion of the deuterium contained in the $(HOD)_2$ pair, ultimately leading to isolated HOD molecules. $D_2O, (HOD)_2$ and isolated HOD molecules are spectroscopically identifiable as separate species. Devlin's group spectroscopically monitors the formation of HOD as a functional of temperature, providing information on the mobility of ionic impurities as a function of temperature. They observe that excess protons begin to actively diffuse at temperatures above 120 K, while hydroxide diffusion seems to be much slower.

The results of the Devlin group raise several issues. Recall that the ice-Ih/XI phase transition at 72 K is catalyzed by hydroxide. [2–5, 17, 34, 80–82] However, it appears that *no* ionic defects are actively diffusing at 72 K. Furthermore, even though hydroxide, not protons, catalyze this phase transition, the results of Devlin's group indicate that protons are initially the most active diffusing species as temperature is raised. Hence, the results of the Devlin group call out for a better understanding of the behavior of ionic defects in ice, and in particular, the mechanism by which hydroxide catalyzes the Ih/XI phase transition.

There are further gaps in our understanding of ionic defects in ice. Cowin and co-workers probed the diffusion of protons by a different method, by gently landing hydronium ions on the surface of a layer of ice and subsequently observing the electric potential set up by the ionic layer. [28] In contrast to the Devlin group experiments,

they found that the excess protons did not diffuse into the ice until the temperature reached 190 K. The difference between the Cowin and Devlin group experiments may originate from the fact that the former probes long-range movement of the excess protons, while the latter may be more sensitive to local motions. Clearly, there is ample room for theoretical methods to make an impact on this field. However, this is a challenging system. Since ice-Ih is an H-bond-disordered substance, it is incorrect to picture ionic defects as diffusing in a periodic potential. The H-bond disorder sets up a *random* medium, with potential traps for both ionic and Bjerrum defects in the disordered material. Characterizing the statistical properties of this random medium, particularly with interest in characterizing the passage of ionic defects, is one of the goals of this work.

We have shown in the previous chapters that periodic DFT is capable of describing the delicate energy differences between H-bond isomers in ice phases. At this stage, we have accumulated a body of evidence for several different H-bond order/disorder phase transitions (Ih−XI, VII−VIII, III−IX, V−XIII) that confirm that DFT for small unit cells, combined with an analytic method we call *graph invariants* [22,51] to extrapolate to the bulk limit for statistical mechanical systems, can accurately describe H-bond order-disorder phenomena in ice phases. The methodology is not as well tested for charged defects. Whereas, in the previous chapters, we have verified that H-bond energetics in pure ice were rather insensitive to the DFT functional and basis set,it is known that hydroxide in liquid water is more sensitive to the DFT method. [127–133] Therefore, we regard the results presented here for hydroxide ion in ice as a first step in the process of building a reliable model of charged defects in ice. We first present results on the structure of hydroxide and L-defects in section 6.2. Next, in section

6.3, we extend the graph-invariant theory presented in section 2.2 to describe the presence of defects. We then report preliminary results from Metropolis Monte Carlo simulations of a hydroxide ion in a proton-disordered ice Ih lattice. In section 6.4, we investigate the proton transfer between a hydroxide ion and neighboring water molecule before concluding with a discussion of future studies.

6.2 Structure of Hydroxides and L-defects in an Ice Ih Lattice

An ionic defect cannot be studied in isolation in a periodic system. For example, removal of a proton from one water molecule creates a hydroxide and L-defect pair, which can diffuse away from each other, as shown schematically in Fig. 6.1. Alternatively, a hydroxide/hydronium pair can be created. We used the process shown in Fig. 6.1, removing a proton and rearranging H-bonds in a unit cell containing 96 water molecules, to generate configurations with variable distance between the ionic and Bjerrum defects. The structural parameters given here are obtained from DFT calculations using the BLYP functional [72,73], Troullier-Martins pseudopotentials [74], and a plane wave cutoff of 70 Ry.

Strong hydrogen bonds are characterized by a shortening of the distance between donor and acceptor oxygens, and a lengthening of the oxygen-hydrogen distance of the donor bond. Based on this criterion, the hydroxide ion in ice-Ih forms strong H-bonds as an acceptor, and weak H-bonds as a donor. The local structure near a hydroxide ion shows little variation depending on the hydrogen bonding arrangement of the water surrounding the defect, and even depends little on whether the hydroxide points along the $c-$axis or lies within an ab layer. A generic local geometry near a hydroxide is shown in Fig. 6.2a. Unlike interstitial-pointing hydroxide ions, discussed

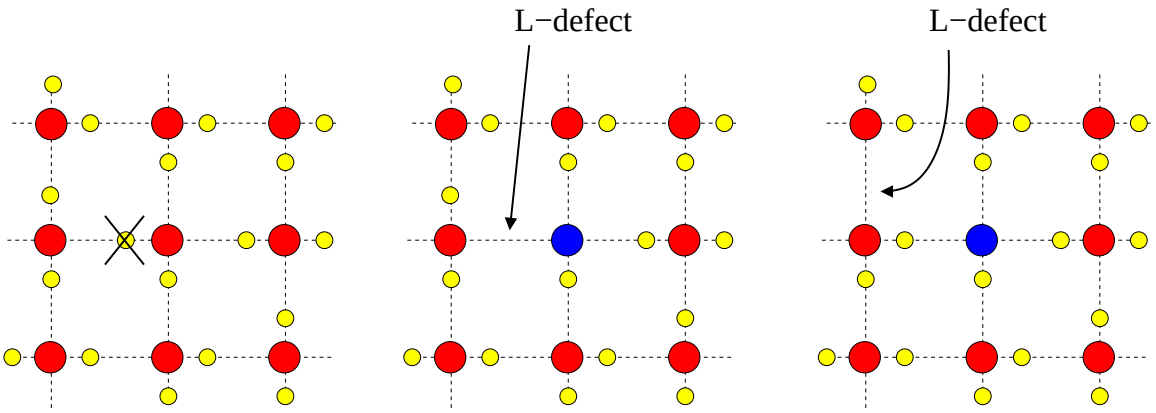

Figure 6.1: Creation of a hydroxide (OH^-) defect is shown schematically in the left panel. The result, center panel, is the creation of neighboring L and hydroxide defects, which can diffuse away from each other as shown in the right panel.

below, these hydroxide ions accept three H-bonds and donate a single H-bond. Bond-length variations from site to site are on the order of 0.01 Å and bond-angle variations are typically a degree or less. Compared to normal H-bonded oxygen-oxygen distances in ice, the distance from the oxygens of water molecules that donate to the hydroxide is shortened to about 2.56 Å, while the distance from the hydroxide oxygen to the oxygen of the water that accepts an H-bond from the hydroxide is lengthened to 2.99 Å. The bond lengths are the only structural feature that deviate strongly from bulk ice. The H-bonds donating to the hydroxide are all within 3 degrees of being linear and the water angles are close to 106°, both typical of bulk ice. Also shown in Fig 6.2 is the local geometry near a typical L-defect. The water molecules of an L-defect donate two H-bonds and accept one. Due to the missing H-bond, the increased electrostatic repulsion displaces the oxygen atoms away from the perfect lattice sites. The observed oxygen-oxygen distance of 3.49 Å is similar to that seen in molecular dynamics simulations with an empirical polarizable potential. [134] The

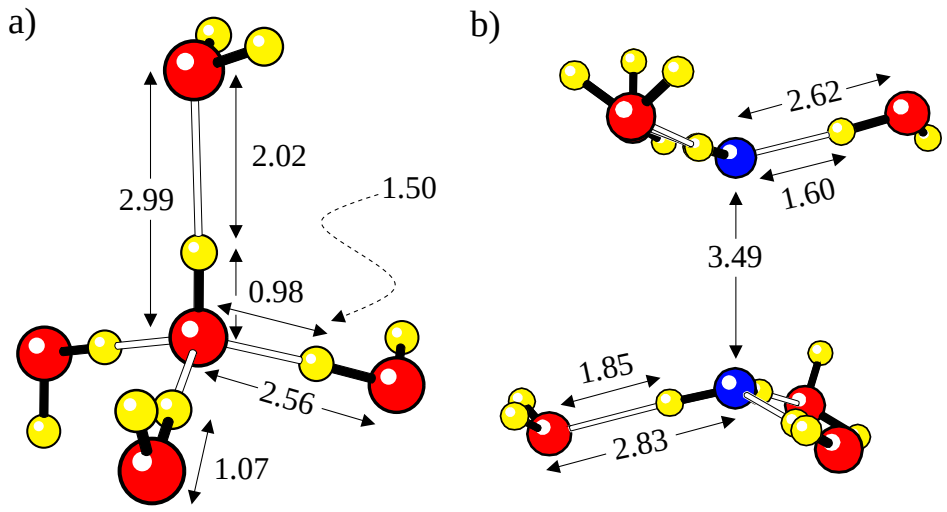

Figure 6.2: Local geometries near a hydroxide(a) and L-defect(b) averaged over 110 H-bond configurations in a 96-water unit cell. All lengths are in units of Ångström.

waters in an L-defect are strong H-bond acceptors and weak H-bond donors with typical oxygen-oxygen separations of 2.62 and 2.83 Å respectively.

A second type of hydroxide defect can be created if the water molecule that accepts an H-bond from the hydroxide were to rotate, so that one of its H-bonds were directed towards the hydroxide. This would push the hydroxide H-bond off of the lattice as well as create a second L-defect. This hydroxide is referred to as an interstitial-pointing hydroxide, OH_I^-, and was first identified in the work of Cwiklik and Buch. [135] This mechanism for the creation of an OH_I^- is shown in Fig. 6.3a. The hydroxide ion, which now accepts four H-bonds, has its H-bond pointing into the interstitial space. The oxygen atom of this defect is five-coordinated with roughly trigonal bypyramidal coordination. An example of the local geometry near an interstitial-pointing hydroxide is shown in Fig 6.3b. To date, we have only examined two configurations involving

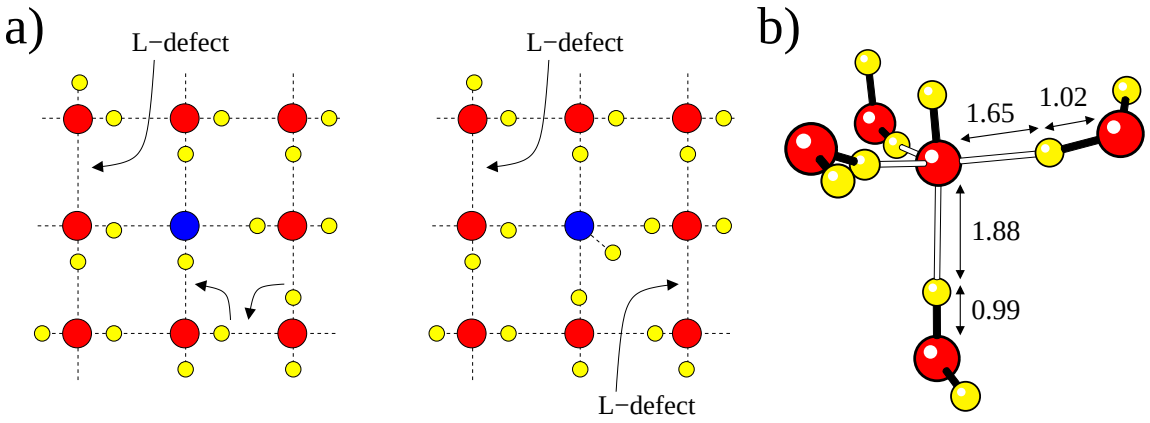

Figure 6.3: a) Creation of an interstitial-pointing hydroxide via rotation of nearby water molecules. Rotation of the water next to the hydroxide creates a DL defect pair. The hydroxide and D-defect combine to form an interstitial-pointing hydroxide. b) Local geometry near an interstitial-pointing hydroxide taken from a single H-bond configuration. All lengths are in units of Ångström.

interstitial-pointing hydroxides and found the change in energy for the creation of this defect to be ∼15 kcal mol^{-1}. Using this energy and the formation energy for a D+L defect pair (a D-defect is an H-bond with two hydrogen atoms), we can estimate the change in energy when a D-defect and hydroxide ion combine to form an interstitial-pointing hydroxide to be −11.7 kcal mol^{-1}.

$$DL \rightarrow D + L \qquad \Delta E = 26.6 \text{ kcal mol}^{-1} \tag{6.1}$$

$$L + OH^- \rightarrow 2L + OH_I^- \qquad \Delta E = 14.9 \text{ kcal mol}^{-1} \tag{6.2}$$

$$D + OH^- \rightarrow OH_I^- \qquad \Delta E = -11.7 \text{ kcal mol}^{-1} \tag{6.3}$$

The energy of reaction (6.3) is obtained by summing the energy of reaction (6.2) with the reverse of reaction (6.1). The symbol DL on the left of reaction (6.1) signifies a recombined D- and L-defect, the absence of a defect. The DL formation energy was obtained by de Koning *et al.* using periodic DFT calculations. [136] The OH_I^-

formation energy would suggest that when hydroxide ions come across D-defects, they readily combine to form interstitial-pointing hydroxides. In this deep trap, hydroxide ion mobility would be significantly decreased because of the increased barrier for proton transfer. This result may explain why the effectiveness of hydroxide doping on the ice Ih/XI ordering transition is concentration dependent. A sufficient amount of hydroxide needs to be added to titrate all of the D-defects. In the configurations we examined, the oxygen-oxygen separation for H-bonds within the trigonal plane were only slightly shorter, $\sim$2.6$-$2.7 Å, than typical separations in ice. The fourth H-bond, perpendicular to the trigonal plane, had an oxygen-oxygen separation of $\sim$2.9 Å. The H-bonds donating to the hydroxide parallel to the trigonal plane are roughly 170° while the fourth H-bond remains linear. The tetrahedral hydrogen bonding of the four water molecules that donate H-bonds to this hydroxide ion is not significantly disturbed. We have not yet included interstitial-pointing hydroxides in the statistical mechanical models developed below.

We now turn to the interaction between the hydroxide ion and the surrounding random H-bond-disordered medium. To illustrate the effect, two configurations of a 96-water (95 waters and a hydroxide) unit cell are shown in Fig. 6.4. The hydroxide and L-defects in Fig. 6.4 are at the same lattice positions. The H-bond arrangement of the other water molecules differs, while, except for the defects, still maintaining the ice rules [101] (each water donates two H-bonds and accepts two other H-bonds).

With the help of the graph-invariant theory described in section 6.3, we were able to identify the most stable H-bond configurations surrounding the defect pair. In pure water ice, the $Cmc2_1$ arrangement of ice XI proposed on the basis of diffraction data [2–5] is calculated to be the lowest-energy arrangement. Now the question

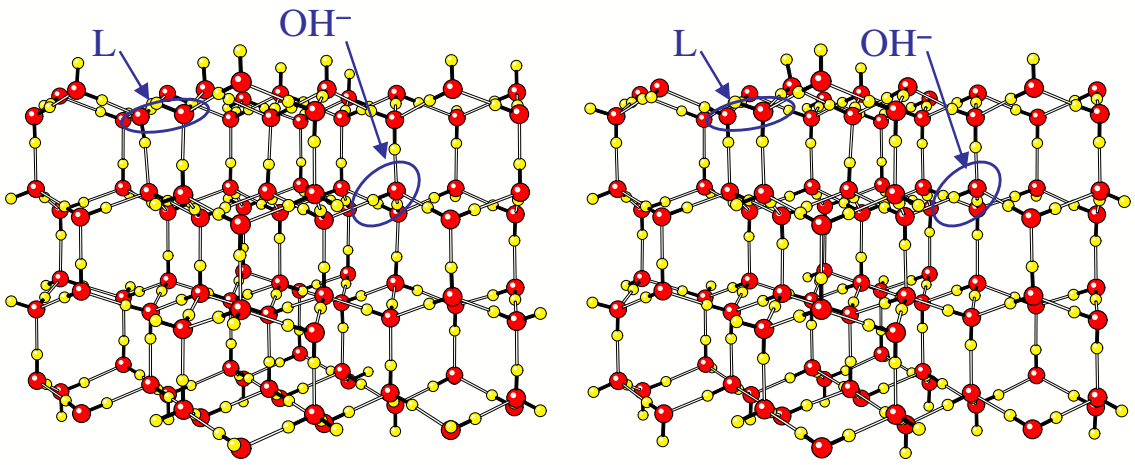

Figure 6.4: Two different H-bond arrangements for 95 waters and a hydroxide. The H-bonds adjacent to the defects are the same in both configurations. The L-defect, originally created when a proton was removed from the system, has diffused away from the hydroxide ion by a distance of roughly 8.5 Å.

arises as to the degree to which these defects disrupt the lowest-energy pure water arrangements. The answer is that the disruption is minimal: a hydroxide prefers to be surrounded by an ice XI structure. Of course, neither a hydroxide nor an L-defect is compatible with a perfect ice XI structure. At least one of the surrounding bonds must be reversed. The family of low-energy H-bond arrangements preferred in our unit cell contains a path of bonds reversed from the ice XI structure that connects the two defects. The lowest-energy structure located to date is shown in Fig. 6.5. In the $Cmc2_1$ ice XI structure, all $c-$axis H-bonds point in the same direction. The H-bonds in each ice XI *ab* layer are aligned in a direction that alternates from layer to layer. The H-bonds in Fig. 6.5 are all in the ice XI structure except for a path of reversed H-bonds leading from the L-defect to the hydroxide. The reversed H-bonds are shown as thicker and colored purple in the figure. Because of periodic boundary

conditions (pbc's), the chain of reversed H-bonds leaves the unit cell at the top of Fig. 6.5 and then re-emerges at the bottom to point into the hydroxide defect. These results are significant because they indicate that the hydroxide defect and the ice XI structure are highly compatible, and that the ice XI structure is disturbed only to the extent necessary to maintain full hydrogen bonding. In the next section, we will quickly review the graph-invariant theory, presented in section 2.2, before discussing how we extend graph invariants to account for the presence of defects.

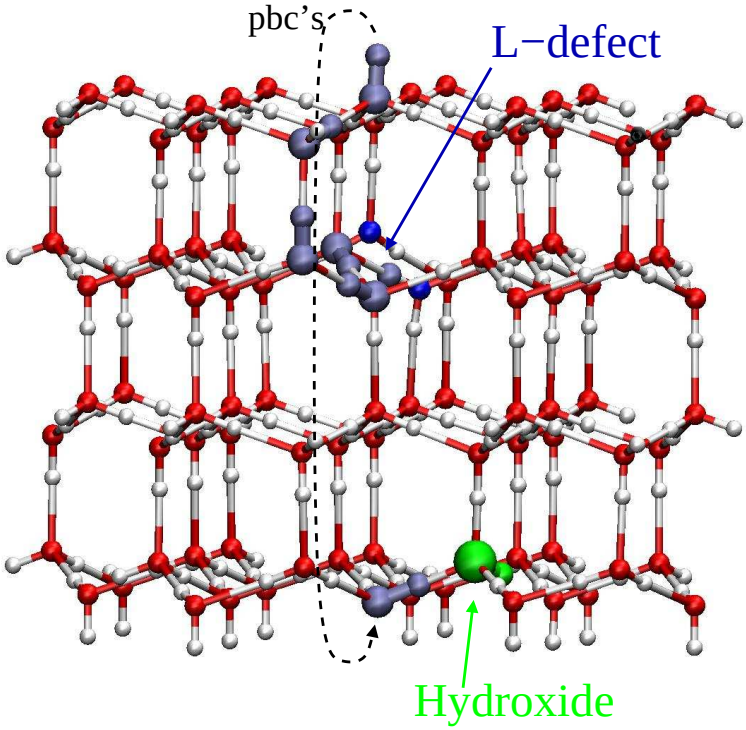

Figure 6.5: The most stable H-bond arrangement in a 96-water unit cell containing a hydroxide ion and an L-defect.

6.3 Graph-Invariant Theory

It would not currently be practical to use electronic structure calculations to search through the billions of possible H-bond arrangements possible for the unit cell pictured in Figs. 6.4 and 6.5. Nor would it be possible to use only electronic structure methods to describe the statistical mechanics of the H-bond-disordered ice lattice. To sift through, or thermally average over H-bond fluctuations, we first link the energy to the H-bond topology. The configuration of H-bonds is described by a set of bond variables. In pure water ice the bond variable b_r takes the values $+1$ or -1 depending on the orientation of the H-bond at bond position r. *If* the energy, or any other scalar physical quantity, can be linked to the H-bond topology (and this is indeed a significant "if" because the topology contains less information than the full set of atomic position coordinates), then it must depend upon combinations of the full set of bond variables $\{b_r\}$ in special combinations that, like the energy, are invariant to symmetry operations. We refer to these combinations, polynomials in the bond variables, as *graph invariants*. Linear polynomials in the $\{b_r\}$ are *first-order graph invariants*, quadratic polynomials are *second-order graph invariants*, and so on. For most ice lattices, there are no invariant linear functions of the $\{b_r\}$ and the leading-order basis functions used to link energy to H-bond topology are the second-order graph invariants. The ability of graph invariants to capture the energetic trends among H-bond arrangements in ice phases, and to predict H-bond ordering phase transitions between ice phases, is documented in the previous chapters. Here we are concerned with the extension to systems with defects.

To describe a system containing both a hydroxide ion and an L-defect, as pictured in Figs. 6.4 or 6.5, the bond variables are also allowed to take the value of 0, which

signifies the absence of a hydrogen bond. In addition to the $b-$variables, we introduce a variable c_r for each bond indexed by r. The c's are zero except at the hydroxide site where the $c-$variable takes the value ± 1 to describe the orientation of the hydroxide ion. This scheme is not unique, but it is sufficient to capture all possible H-bond arrangements in the system pictured in Figs. 6.4 or 6.5. Following the discussion in section 2.2, polynomials in the $b-$ and $c-$variables invariant to symmetry operations are generated using the projection operator for the totally symmetry representation of the appropriate symmetry group for the system under study. [19, 20, 22–24, 51] For ice lattices, this is the crystal space group [22] while for finite water clusters it is the point group. [51] Because there are usually no invariant linear polynomials (first-order graph invariants) and higher-order polynomials have, to date, never been needed, the most important of these polynomials are the quadratic ones (second-order graph invariants). Second-order graph invariants involving only $b-$variables,

$$I_{rs} = \frac{1}{|G|} \sum_{\alpha=1}^{|G|} g_\alpha (b_r b_s) \,, \tag{6.4}$$

are used to describe pure water ice. In this equation, $|G|$ is the order of the symmetry group and the sum is over the members of the symmetry group. The invariant is labeled by the bond pair, r and s, from which it is generated by the projection operator. With a single hydroxide ion present, second-order graph invariants of the form

$$I_{rs,c} = \frac{1}{|G|} \sum_{\alpha=1}^{|G|} g_\alpha (b_r c_s) \,, \tag{6.5}$$

involving a $b-$ and a $c-$variable are also needed to describe interactions between the hydroxide and surrounding water molecules. In principle, if several hydroxides were present and interacting with each other, invariants involving two $c-$variables

would be required. We have previously shown how this formalism can be applied to a hydroxyl radical defect in a water cluster. [52]

Using expressions like Eqs. (6.4−6.5) we can generate a complete set of invariant functions to parametrize the dependence of energy on the H-bond topology in the following form.

$$E(b_1, b_2, \ldots, c_1, c_2, \ldots) = \underbrace{\sum_r \alpha_r I_r(b_1, b_2, \ldots, c_1, c_2, \ldots)}_{\text{sum over 1st-order invariants}} + \underbrace{\sum_{rs} \alpha_{rs} I_{rs}(b_1, b_2, \ldots, c_1, c_2, \ldots)}_{\text{sum over 2nd-order invariants}} + \underbrace{\ldots}_{\text{negligible}} \tag{6.6}$$

In practice, the $\alpha-$coefficients are determined for small unit cells for which electronic structure calculations are feasible. Since we have shown that invariants for a small unit cell are automatically invariants for larger cells, the formalism provides a means to extrapolate an expression for the energy to unit cells large enough to be a simulation cell for statistical mechanical calculations. In practice, the expansion is truncated at second order, as indicated in Eq. (6.6).

To date, for pure water ice phases, second-order invariants generated by projection on a small number of nearby bond pairs were sufficient. Kuo *et al.* have shown that the existence of a graph element that takes one bond into minus itself is a necessary and sufficient condition for there to be no first-order invariants. [51] This is the usual case for ice structures, and first-order invariants only appear for the ice III/IX and ice V/XIII systems. For the ice-Ih system, discussed in chapter 2, three second-order invariant functions provided an accurate parametrization of the energy. [19, 20] We used those same three invariant functions with $\alpha-$coefficients calculated from the 48-water $2 \times 2 \times 1$ cell to describe the pure water portion of the system. On physical

grounds, we expect charge-dipole interactions to be important in the presence of ionic defects. The implication would be that invariants involving variables b_r and c_s where bonds r and s are not close to each other might also be significant. The charge-dipole interaction amounts to collecting a large number of $b_r c_s$ terms together with a single coefficient proportional to the combination $\frac{q\mu}{\epsilon_{eff}}$,

$$E_{CD} = \frac{q\mu}{\epsilon_{eff}} \sum_{rs} I_{rs}(b_1, b_2, \ldots, c_1, c_2, \ldots), \tag{6.7}$$

where ϵ_{eff} is an effective dielectric constant for the medium and the sum is over bonds r and s that are not nearest neighbors.

To account for this possibility, we included interactions (also invariant!) involving charges on the hydroxide ion, L-defect, and water molecules. The energy expression with the defect-water electrostatic interactions is still in the form of Eq. (6.6). The location of the L-defect charge was placed at the midpoint of the two oxygen atoms which formed the L-defect. For the hydroxide ion, the charge was entirely localized on the oxygen atom. Charges for the water molecules were placed at the location of the oxygen and hydrogen atoms. The sum of the hydroxide and L-defect charges, Q_{OH} and Q_L respectively, was constrained to be -1.

$$Q_L + Q_{OH} = -1 \tag{6.8}$$

The sum of the charges on each water molecule was constrained to be zero,

$$Q_O + 2Q_H = 0, \tag{6.9}$$

where Q_O and Q_H are the oxygen and hydrogen atom charges respectively. The energy expression for the defect-defect and defect-water interactions takes the form

$$\underbrace{Q_{OH}(Q_O E_{OH,O} + Q_H E_{OH,H})}_{\text{hydroxide-water}} + \underbrace{Q_L(Q_O E_{L,O} + Q_H E_{L,H})}_{\text{(L-defect)-water}} + \underbrace{Q_L Q_{OH} E_{L,OH}}_{\text{hydroxide-(L-defect)}}, \tag{6.10}$$

where the $E_{j,k}$ are Ewald sums calculated with positive test charges located at the corresponding positions of the $j-$ and $k-$type atoms. In order to use this expression to evaluate the energies of H-bond configurations in a large simulation cell, it will be necessary to know the coordinates of all atoms. To calculate the Ewald sums and fit the charges, we employed the following model to generate atomic coordinates. For each H-bond configuration, all oxygen atoms were fixed at their perfect lattice sites. The hydrogen atoms were placed 1 Å from the covalently bonded oxygen along the line joining the two oxygen atoms in the H-bond.

We proceeded by generating a handful of H-bond configurations in the 96-water cell and used periodic DFT calculations, as described above, to obtain the minimum-energy geometries. Using the calculated energies and model geometries, we fit the charges and invariant coefficients for the $b_r c_s$ type second-order invariants. Again, the coefficients for the bulk ice invariants were taken from previous calculations discussed in chapter 2. With this expression, Metropolis Monte Carlo simulations of the 96-water cell were performed to generate a sampling of configurations for further calculations. An energy expression was parametrized and the procedure repeated until a thorough sampling of the energy range was obtained. Also, with this procedure, we were able to efficiently identify the lowest-energy H-bond configuration, the structure of which is shown in Fig 6.5.

At the beginning of this section, we described the link between energy and the H-bond topology as something that cannot be taken for granted and must be verified. The data in Fig. 6.6 is an important part of that verification process. If the fit using the graph-invariant expression of Eq. (6.6) was perfect, then all points would lie on the diagonal. The low-energy points in Fig. 6.5 are the ice XI-like structures

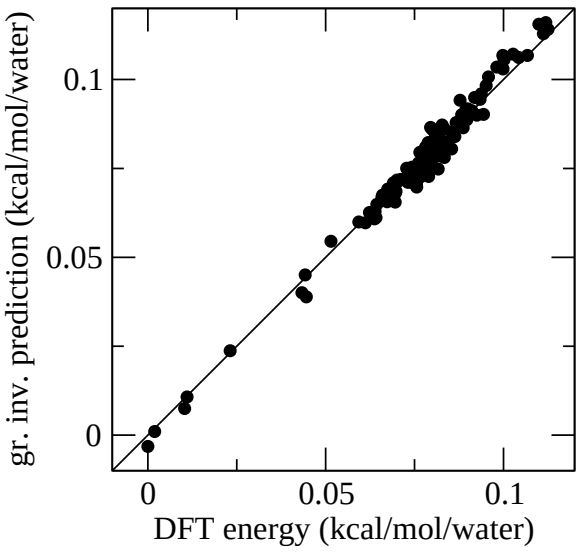

Figure 6.6: Energy of 110 H-bond isomers of a 96-water unit cell containing a hydroxide ion and an L-defect is compared with a fit of the form of Eq. (6.6).

described in section 6.2 with closed loops of H-bonds and paths of reversed H-bonds connecting the hydroxide and the L-defect. In our fit to the data, the charge on the L-defect went to zero and the hydroxide had a charge of -1. (The charge of -0.38 normally associated with an L-defect is a charge associated with a polarization current when a water molecule reorients, not a physical charge.) Increasing the flexibility in the model by allowing a nonzero charge on the hydrogen atom of the hydroxide ion still resulted in the full charge of -1 being located on the oxygen atom of the hydroxide. The charge of the oxygen atoms in the water molecules was -0.20. We found that inclusion of $b_r c_s$ type invariants was not necessary for a good quality fit of the energies. Their contribution to the relative energies of the H-bond configurations was consistently an order of magnitude smaller than the bulk-ice graph-invariant and electrostatic contributions. When included, $6-7$ additional invariants of the

form given in Eq. (6.5) involving bonds r and s that were nearest-neighbors gave a satisfactory fit of the relative energies of H-bond configurations. A good quality fit of the energies without including electrostatic interactions was possible, but as expected, it required a relatively large number of invariants whose generating bond pairs were separated further than next-nearest-neighbors.

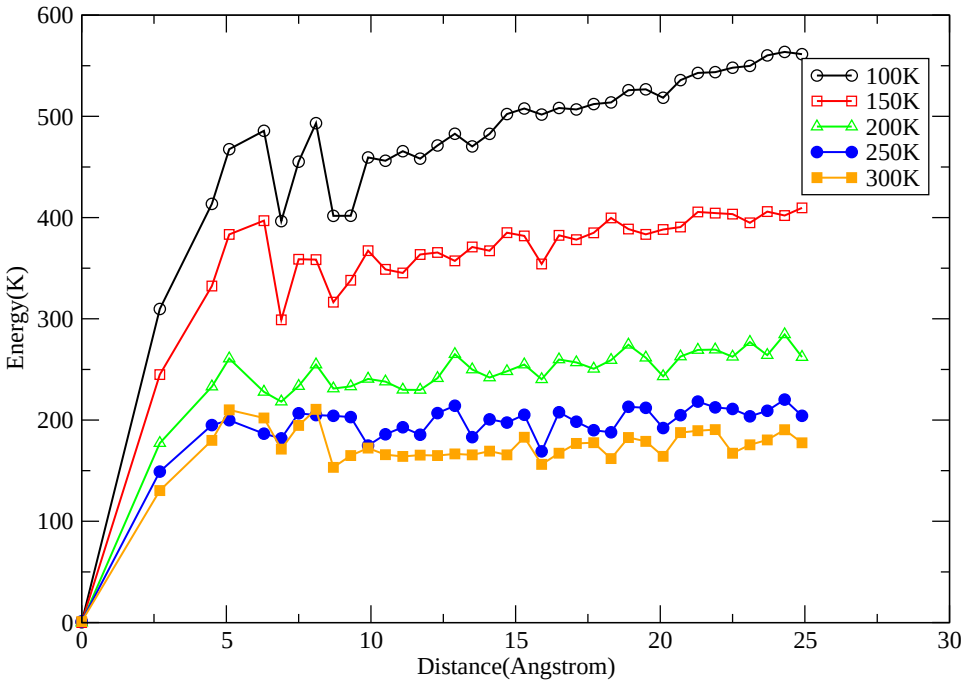

Figure 6.7: Energy as a function of the distance between a hydroxide ion and its original location. Each curve is the result of averaging 10000 trajectories.

Using the graph-invariant theory, extended to treat the presence of defects, we have parametrized an effective Hamiltonian for describing H-bond fluctuations in a large simulation cell when a hydroxide ion and an L-defect are present. The following is preliminary work on the statistical properties of a hydroxide ion in a disordered ice lattice. To investigate the degree to which hydroxide ions are trapped in ice,

we performed a series of simulations at several temperatures. These simulations were performed in a cell measuring 10×10×10 unit cells on each side containing 12000 water molecules. For these simulations, the only trial moves that were attempted involved the hydroxide ion moving one H-bond at a time. One of the three H-bonds donating to the hydroxide was chosen at random to be flipped. If the trial configuration caused the distance between the hydroxide ion and its original location at the start of the simulation to increase, then the move was accepted regardless of the change in energy. The simulations were terminated when the hydroxide distance reached 25 Å, which was the maximum distance possible in this simulation cell due to periodic boundary conditions. For each temperature, averages over 10000 trajectories were used to obtain the energy vs. hydroxide distance curves shown in Fig 6.7. Initial configurations for these trajectories were obtained from standard Metropolis Monte Carlo simulations with the hydroxide and L-defect positions frozen at the largest possible separation allowed in this simulation cell. From the energetics along the hydroxide diffusion paths shown in Fig 6.7, we can see that the general trend is for energy to increase with distance. The barrier for hydroxide diffusion increases with decreasing temperature, almost doubling from 300 to 100 K. In the next section, we present our work to date on the proton transfer between a hydroxide ion and water molecule in a disordered ice lattice.

6.4 Proton-Transfer Barriers in Ice

The information presented up till now concentrated on the equilibrium energetic and structural aspects of defects in a proton-disordered ice lattice. We now investigate the mechanism by which hydroxide ions diffuse through a disordered ice lattice.

The motion of hydroxide ions occurs via proton transfer from one of the three water molecules donating H-bonds to the hydroxide. After one of the protons hops across its H-bond, the water molecule and hydroxide will have switched places resulting in the migration of the hydroxide within the ice lattice. In Figure 6.8a, the proton-transfer barrier for five different H-bond configurations in a 96-water cell are shown. The periodic DFT calculations are similar to those discussed above with a plane wave cutoff of 70 Ry. In these plots, energy is plotted versus the proton-transfer reaction coordinate taken to be the difference between the two oxygen-hydrogen distances in the H-bond, as illustrated in Fig 6.8b. For each proton-transfer event, the zero of energy is taken to be the lowest energy point along the path corresponding to one of the two equilibrium configurations. For all cases, the transition state is found to be close to the midpoint of the H-bond with a proton-transfer barrier height of $\sim 0.8 - 1.0$ kcal mol^{-1}. With such small barrier heights, one would expect that quantum effects will be important to accurately describe proton transfer in an ice lattice. To illustrate this point, in Fig 6.8c, there is an example of fitting a proton-transfer barrier to a double-well potential and solving for the lowest-energy eigenvalues and eigenstates. It is not surprising that we find the lowest energy state lying at, if not above, the barrier for proton transfer. The ground-state probability distribution for this proton is delocalized across both wells. We now report on the current progress of investigating whether the effects on the barrier heights due to proton disorder can be accurately described by a graph-invariant expression.

In addition to the five proton-transfer barriers shown in Figure 6.8, we calculated seven additional barrier heights for different H-bond configurations in the 96-water cell. In these additional calculations, we assume that the transition state for the

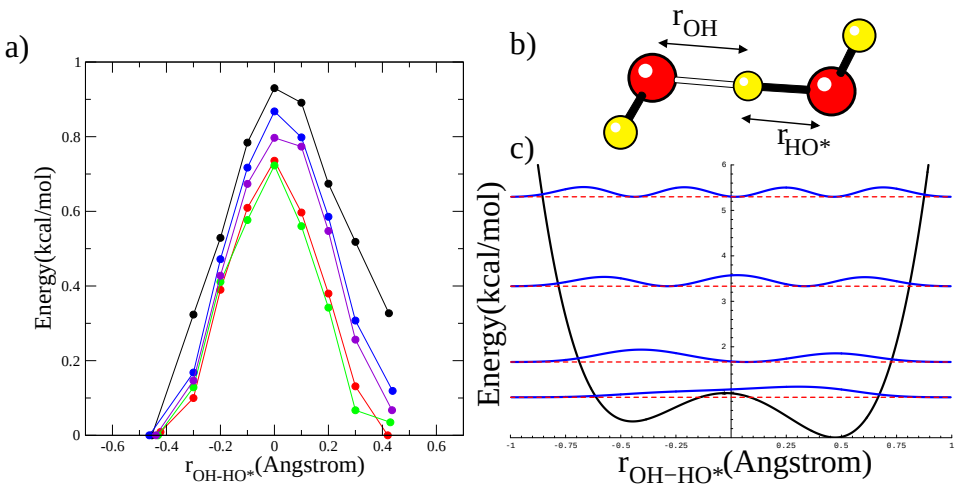

Figure 6.8: a) Potential energy as a function of proton-transfer reaction coordinate for five H-bond configurations in a 96-water cell. b) The reaction coordinate for the proton transfer between a hydroxide and water molecule is taken to be the difference in oxygen-hydrogen distances in the H-bond. c) The energy levels and probability distributions for the lowest states of a double-well potential calculated using a discrete variable representation algorithm [13].

proton is located at the midpoint of the H-bond. Thus, we only used energies of the two minima, E_1 and E_2, and transition state, $E^\dagger$, to determine the barrier heights, as shown in Fig 6.9a. The quantity E_{12} is the average energy of the reactant and product ground-state energies,

$$E_{12} = \frac{1}{2}(E_1 + E_2). \tag{6.11}$$

As shown in the previous section, these are quantities for which we have successfully parametrized an effective Hamiltonian using graph invariants. For the barrier height, we use the following quantity,

$$\Delta E = E^\dagger - E_{12}, \tag{6.12}$$

to parametrize a graph-invariant expression using second-order $b_r c_s$ type invariants.

$$\Delta E(b_1, b_2, \ldots, c_1, c_2, \ldots) = \Delta E_0 + \sum_{rs} \alpha_{rs} I_{rs}(b_1, b_2, \ldots, c_1, c_2, \ldots) \tag{6.13}$$

For this problem, the $c-$variables describe the H-bond that the proton is transferring across and is defined to always take the value of 1. The $b-$variables describe all other H-bonds and take values ± 1 depending on the orientation of the H-bond. Empty H-bonds are assigned the value of zero. In this model, we only examine the case of a single proton-transfer event occurring at a time. The ability of the graph invariant expression, Eq. (6.13), to predict the barrier heights for the 15 proton-transfer reactions is shown in Figure 6.9b for both plane wave cutoffs of 70 and 90 Ry. To achieve good quality fits, it was only necessary to include 6 and 7 invariants, respectively, plus a constant. As can be seen, the graph-invariant expressions do a good job of reproducing the barrier heights. It is also clear, from the figure, that the barrier

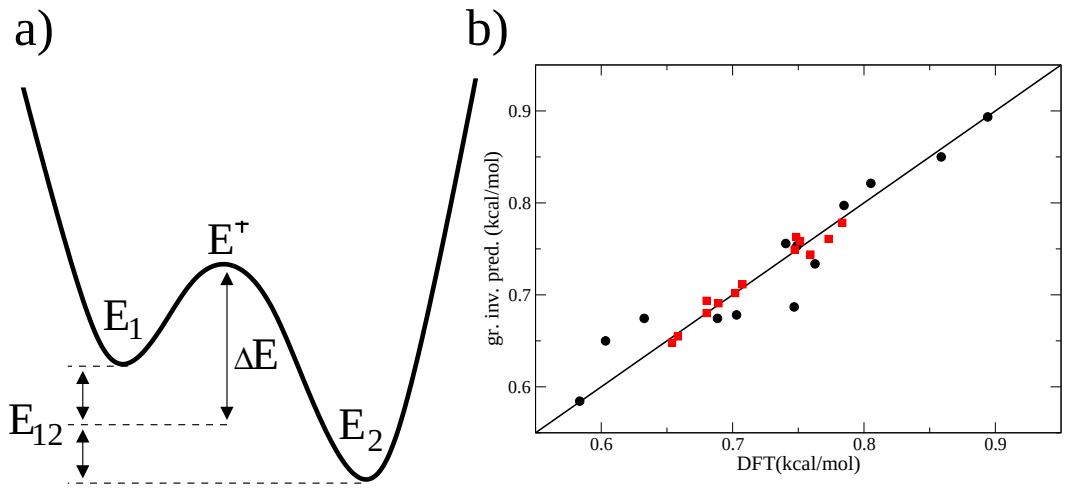

Figure 6.9: a) Model used to calculate barrier heights which are fit to a graph invariant expression. b) Predicted vs. calculated barrier heights for 15 proton transfer events in a 96-water cell calculated at plane wave cutoffs of 70(●) and 90 Ry(■).

heights calculated at 70 Ry are not converged with respect to the plane-wave cutoff. To test if the 90 Ry barrier heights are converged, we need to repeat the calculations at a higher plane-wave cutoff, maybe 120 Ry. We also need to double or triple the sampling of proton-transfer reactions to test the robustness of the graph-invariant fits. It is possible that with a more thorough sampling of H-bond configurations, a good quality fit with graph invariants may require many more terms. With increased sampling, if the quality of the fit degraded past the point of no longer being meaningful, then there may be an alternative worth pursuing. The barrier heights calculated at 90 Ry only span a range of $\sim$0.13 kcal mol^{-1}. It may prove adequate to assume that all barrier heights, ΔE, are independent of the surrounding H-bond topology. We could then simply use the average barrier height, which for the 90 Ry calculations is 0.72 ± 0.04 kcal mol^{-1}.

6.5 Outlook

In this chapter, we successfully extended the graph-invariant theory, discussed in section 2.2, to account for the presence of defects. Using previously determined bulk-ice invariant coefficients, $b_r c_s$ defect type invariants, and defect-water electrostatic interactions, we successfully constructed a model to describe the relative energies of H-bond configurations in a 96-water cell. We calculated barrier heights for the proton transfer between a hydroxide and water molecule. We found that typical barrier heights were less than 1 kcal mol^{-1} indicating that the proton is likely to be delocalized across the H-bond. This indicates that the inclusion of quantum effects are important if one is to obtain an accurate description of hydroxide motion in a disordered ice lattice. We presented preliminary work on using a graph-invariant

expression to account for the effects on the proton-transfer barrier heights due to the surrounding disordered ice lattice. The next piece of the puzzle is to construct an empirical potential, which would keep track of the detailed atomic coordinates, but know nothing about the effects due to H-bond disorder. If we are able to couple these three models together, we may then be able to study the quantum transport of a hydroxide ion in a disordered ice lattice and shed light onto the mechanisms by which proton order/disorder transitions occur in ice.

CHAPTER 7

SITE DISORDER IN ICE VII ARISING FROM H-BOND FLUCTUATIONS

7.1 Introduction

The proton ordering phase transition of ice VII to anti-ferroelectric proton-ordered ice VIII is, in many respects, considered to be well-characterized. What is not well understood, however, is the apparent site disorder of the oxygen atoms as suggested from recent neutron diffraction studies. [44, 137, 138] Studying ice VII in its region of stability, Kuhs *et al.* achieved a good fit to neutron diffraction data treating the thermal motion of the oxygens anharmonically. [44] This model led to a surprisingly short O-D distance of $\sim$0.89 Å which lengthened by $\sim$0.13 Å when this distance was allowed to vary freely after another refinement with a rigid water geometry. From this analysis, it appeared that there was significant motion along the set of $\langle 100 \rangle$ axes suggesting disorder of the oxygen atoms about their perfect lattice sites. Here, the symbol $\langle 100 \rangle$ stands for all axes related by symmetry to the [100] axis, for example: [100], $[\bar{1}00]$, [010], $[0\bar{1}0]$, [001], and $[00\bar{1}]$. Jorgensen and Worlton investigated the structure of ice VII using a time-of-flight neutron diffraction technique. [137] They also found it difficult to separate the static and thermal displacements of the oxygen

atoms. Introducing a multisite model for the hydrogens did elongate the O-D distance somewhat, but it suggested D-O-D angles that did not seem probable. Thus, they also concluded that some displacement of the oxygen along the ⟨100⟩ directions, away from the covalently bonded deuteriums, would allow for the lengthening of the O-D distance.

More recently, an investigation by Nelmes *et al.* refined neutron diffraction data using various combinations of multisite models for both the oxygen and hydrogens treating the thermal motion harmonically. [138] A good fit of their models was measured by the closeness of the water molecule geometry to that found in ice VIII, the proton-ordered phase, with an O-D distance and D-O-D angle of 0.970 Å and 107.3° respectively. [138] They found the best fit was achieved when oxygen atoms were displaced along the set of ⟨111⟩ axes and the hydrogens shifted along 3-fold sites surrounding the ⟨111⟩ axes. This gave an O-D distance and D-O-D angle of 0.977 Å and 107.1° respectively. The best fit that could be achieved using the ⟨100⟩ axes for oxygen, with 3-fold sites for hydrogens, resulted in a water geometry of 1.01 Å and 107°, consistent with the earlier work of Kuhs *et al.* [44] Regardless of model, all fits yielded site displacement magnitudes of ∼0.135Å. The ⟨100⟩ model for oxygen displacement yielded H-bonded oxygen-oxygen distances of 2.833 and 2.839 Å, both in close agreement with their data from ice VIII under similar conditions. However, the ⟨111⟩ model which gave the best water geometry overall also predicted two sets of H-bonded oxygen-oxygen distances that were ∼0.1 Å longer and shorter than the H-bond distances in ice VIII. As the authors indicate, this is a feature not yet observed in spectroscopic studies.

In an attempt to understand these results and shed light on the nature of the static motion of the oxygen atoms in ice VII, we have developed a model that predicts the oxygen displacement from a perfect lattice site as a function of the surrounding H-bond network. Looking at the distance over which H-bond topology affects the site geometry, we find good convergence of the model only including neighboring waters. In section 7.2, we review DFT theory calculations of H-bond configurations of a 32-water ice VII cell, discussed in chapter 2. We develop and parametrize a model in section 7.3 which describes the displacements of oxygen atoms from their perfect lattice sites. In section 7.4, we discuss the results of statistical mechanical calculations on a large simulation cell where we use graph invariants to describe H-bond fluctuations. We conclude with a discussion of the results in section 7.5.

7.2 Periodic DFT Calculations

H-bond configurations used in a previous study of the ice VII/VIII proton ordering phase transition were used to parametrize the oxygen displacement model discussed below. [19, 20] Here, we repeat some details of the calculations for convenience. The ice VII unit cell measures $2\sqrt{2} \times 2\sqrt{2} \times 2$ primitive cells on each side consisting of 32 water molecules with lattice constant $a = 3.337$ Å. Periodic DFT calculations were performed on 50 configurations using the CPMD [69–71] program with the BLYP gradient correction [72, 73] to the local density approximation, Troullier-Martins norm-conserving pseudopotentials [74] and plane wave cutoffs of up to 120 Ry. The increased cutoff, relative to the 70 Ry cutoff used in the previous studies [19, 20], was used to ensure convergence of the geometries. The Brillouin zone sampling was restricted to the $\Gamma-$point.

system	O-H(Å)	H-O-H(°)	O–H(Å)	O-H–O(°)	O–O(Å)
VIII(70Ry)	0.9889 ± 0.0000	105.92 ± 0.00	1.9016 ± 0.0000	177.30 ± 0.00	2.8898 ± 0.0000
VIII(90Ry)	0.9844 ± 0.0000	106.24 ± 0.00	1.9061 ± 0.0000	177.56 ± 0.00	2.8898 ± 0.0000
VIII(120Ry)	0.9837 ± 0.0000	106.25 ± 0.02	1.9068 ± 0.0008	177.56 ± 0.02	2.8898 ± 0.0008
VII(70Ry)	0.9893 ± 0.0004	105.34 ± 0.30	1.9021 ± 0.0090	177.72 ± 1.03	2.8907 ± 0.0085
VII(90Ry)	0.9847 ± 0.0004	105.61 ± 0.31	1.9066 ± 0.0098	177.87 ± 0.99	2.8908 ± 0.0093
VII(120Ry)	0.9840 ± 0.0004	105.59 ± 0.30	1.9073 ± 0.0100	177.88 ± 0.98	2.8908 ± 0.0096

Table 7.1: Averaged geometrical features of H-bond configurations of an ice VII unit cell for a series of plane wave cutoffs. Geometrical properties labeled ice VIII were averaged over the 32-water configuration corresponding to the experimental ice VIII structure with error bars indicating one standard deviation. Those properties labeled ice VII were averaged over all waters in the 50 H-bond configurations studied here. The O–O distances reported are H-bonded oxygen-oxygen distances.

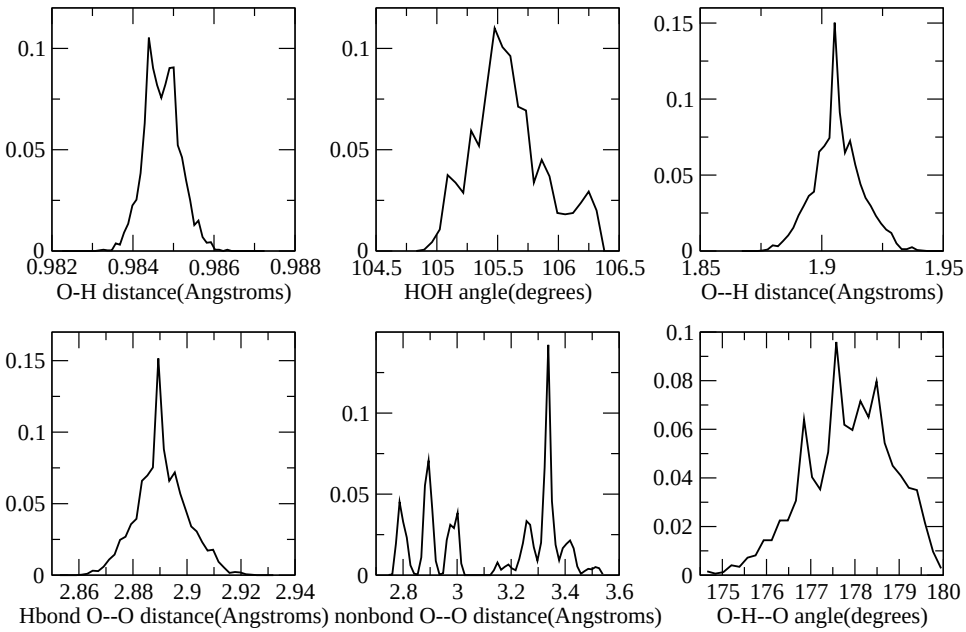

Figure 7.1: Probability distributions for various geometrical features calculated from the 50 H-bond configurations optimized with a 90 Ry plane wave cutoff.

From the optimized geometries, probability distributions of certain distances and angles were calculated and are shown in Figure 7.1. Averages of the distances and angles, presented in Table 7.1, showed a decreasing change with increasing plane wave cutoff suggesting we have nearly reached convergence with respect to geometrical properties. We find that the H-bonded oxygen-oxygen probability distribution has a single peak with an average of 2.8908 $\pm$ 0.0093 Å. We do not see evidence of a bimodal distribution of H-bonded distances with a peak separation of $\sim$0.2 Å as suggested by Nelmes *et al.* [138] However, analysis of the *nonbonded* oxygen-oxygen distances shows three peaks each separated by $\sim$0.1 Å with the central peak located very close to the H-bonded oxygen-oxygen distance. Average oxygen-oxygen distances for the nearest-nonbonded peaks, shown in Figure 7.1, are 2.7956 $\pm$ 0.0153,

2.8928 ± 0.0126, and 2.9855 ± 0.0154 Å. As discussed below, the largest component of the oxygen site displacement is in a direction away from the water dipole vector. When nearest-neighbor nonbonded waters have dipoles pointing toward each other, similar to waters labeled "0" and "12" in Figure 7.2b, the oxygen displacements are away from each other giving rise to the peak near 2.99 Å. When the dipoles point away from each other, like waters labeled "0" and "6" (also "0" and "7") in Figure 7.2b, the displacements push the waters closer generating the peak near 2.79 Å. Dipoles oriented in the same direction result in a nonbonded oxygen-oxygen distance unchanged from the hydrogen bonded distance. Orientations of dipoles whose dot product is zero, waters "0" and "13", can have distances of 2.89 Å and, coincidentally, one of the other values depending on whether the dipole of the central water, labeled "0" in Figure 7.2b, points towards or away from the nonbonded neighbor.

7.3 H-Bond Model for Site Displacements

To model the oxygen site displacement, we seek an expression that accounts for the surrounding H-bond network of a given water molecule. In the previous chapters, we have shown that an economical description of the dependence of scalars, like the energy, on H-bond topology can be developed. The key is to form combinations of variables that capture the orientation of H-bonds that are invariant to all symmetry operations of the appropriate space group. We refer to these combinations as graph invariants. Here we extend that idea by forming combinations of H-bond variables that transform as a first-rank vectorial tensor. The simplest function that captures how the displacement vector, $\mathbf{d}_0$, depends on the local H-bond topology is a linear

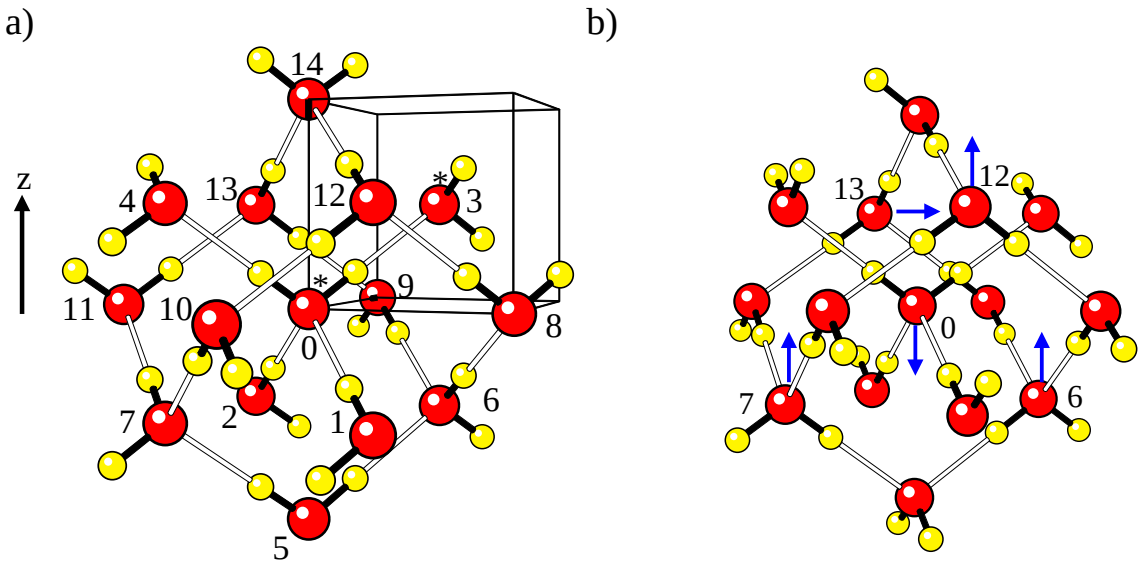

Figure 7.2: (a) Nearest H-bonded neighbors (1-4), nearest non-H-bonded neighbors (5-14) surrounding a central water labeled "0" in the figure. We refer to the orientation of the central water, dipole pointing in the +z−direction and hydrogen bonds along the ⟨111⟩ axes, as the "canonical" orientation. Water molecules labeled with asterisks are those that make up the primitive unit cell of ice VII which the thin black lines outline. (b) Arrows on the central water and its four nearest-nonbonded neighbors indicating the direction of the site displacements as discussed in the text. The water labeled "13" has its dipole vector in the $xy-$plane while the other labeled waters (0,6,7,12) have their dipoles pointing along the $z-$axis.

combination of H-bond vectors. Higher order combinations that transform as a first-rank tensor can be generated with group theoretical projection operators [22,51], but we have found that the lowest-order linear description given in the following equation is adequate to describe site disorder in ice VII.

$$\mathbf{d}_0 = \mathbf{c}_0\hat{\mu}_0 + \sum_{i=1}^{2} \mathbf{c}_i\hat{\mu}_i + \sum_{i=3}^{4} \mathbf{c}_i\hat{\mu}_i + \sum_{i=5}^{14} \mathbf{c}_i\hat{\mu}_i + \ldots \tag{7.1}$$

The $\mathbf{c_i}$ are 3×3 coefficient matrices and $\hat{\mu}_\mathbf{i}$ is a unit vector in the direction of the dipole of the ith water where the indices are defined in Figure 7.2. The leading term in the expression, $\hat{\mu}_0$, is a sum over the two bond vectors of the water whose displacement

is being described by the linear expansion. It is found that the water is displaced in a direction opposite to the direction of the dipole, placing the center of mass of the molecule closer to the perfect lattice site. Keeping only this term in the expression results in a model identical to the $\langle 100 \rangle$ model used to fit experimental data.

$$\mathbf{d}_0^{\langle 100 \rangle} = \mathbf{c}_0 \hat{\mu}_0 \tag{7.2}$$

The next two terms in Eq. (7.1) arise from nearest neighbors on the same sub-lattice which donate and accept hydrogen bonds respectively. Each of these four waters can only take three of the six allowed orientations, due to the ice rules, resulting in 81 possible displacements from the set of $\langle 100 \rangle$ axes. The next term in the expression comes from the 10 closest neighbors found on the other sub-lattice which were divided into 5 groups of waters depending on their height with respect to the z-axis. We found no significant improvement in fitting the oxygen site displacement when additional waters were included in the linear model.

$$error = \sum_{i}^{config} \sum_{j}^{water} \left\{ [\mathbf{R}_j + \mathbf{d}_j^{(i)}] - [\mathbf{r}_j^{(i)} + \mathbf{s}^{(i)}] \right\}^2 \tag{7.3}$$

The coefficient matrices, the $\mathbf{c}$'s in Eq. (7.1), were determined by minimizing the least squares error defined by Eq. (7.3), where the index i runs over the 50 H-bond configurations and j over the 32 water molecules per configuration. The perfect lattice positions, $\mathbf{R}_j$, for the jth water were generated using the lattice constant $a = 3.337$ Å, the same lattice constant used in the periodic DFT calculations. The displacement of the oxygen from its perfect lattice site, $\mathbf{d}_j^{(i)}$, for the jth water in the ith configuration was defined in Eq. (7.1). $\mathbf{r}_j^{(i)}$ is the position of the jth water in the ith configuration in the optimized geometry obtained from periodic DFT calculations. A translation for each H-bond configuration, $\mathbf{s}^{(i)}$, was included to account for any overall translation of

the system that may have occurred during the geometry optimization. All coefficient matrices could be made to be of the form

$$\mathbf{c} = \begin{pmatrix} c_{11} & c_{12} & 0 \\ c_{12} & c_{11} & 0 \\ 0 & 0 & c_{33} \end{pmatrix}$$

without any degradation in quality of fit to the data. Since we divide the fifteen waters shown in Figure 7.2 into eight unique contributions, this leads to a total of 22 independent parameters which are listed in Table 7.2. The coefficient matrix for the water labeled "0" only has one nonzero entry, c_{33}, because $\hat{\mu}_0$ is taken to be parallel to the $z-$axis in the canonical orientation. If this was the only term used in

waters	c_{11}	c_{12}	c_{33}
0	0	0	−0.06644760
1−2	−0.00236387	−0.00147139	−0.00298849
3−4	−0.00295796	−0.00163781	−0.00281003
5	−0.01463340	−0.01180770	−0.00569223
6−7	0.00923378	0.00288609	0.00415282
8−11	0.00087710	0.00414371	0.00107050
12−13	−0.00211376	−0.00142694	0.00455538
14	0.01100470	−0.00684993	0.00402371

Table 7.2: Matrix elements for the coefficient matrices, the **c**'s in Eq. (7.1), for the oxygen displacement, in units of Ångströms, for a water molecule in the canonical orientation as shown in Figure 7.2. These coefficients were obtained using the geometries calculated with a 90 Ry plane wave cutoff.

the model, $\mathbf{d}_0^{\langle 100 \rangle}$, then this nonzero entry would correspond to the site displacement magnitude in the $\langle 100 \rangle$ model discussed above. Fitting the data to the $\mathbf{d}_0^{\langle 100 \rangle}$ model gave $c_{33} = -0.076$Å which is only slightly larger than the corresponding coefficient in Table 7.2.

There are two ways to measure the degree to which our model links site displacements to H-bond topology: 1) prediction of the displacements in their original crystal lattice orientation from perfect lattice positions, 2) rotation of each water into the canonical orientation defined in Figure 7.2a and then measuring the displacement from the perfect lattice position. In the former case, the displacements range from -0.1 to $+0.1$ Å. The displacements of waters in their original crystal lattice orientation take place with equal magnitude in six directions from the perfect lattice sites. In the latter case, because the waters are now oriented in the same way and the displacement largely occurs in a direction opposite to the water dipole, the displacements now range from -0.1 to 0 Å in the $z-$direction, the direction of the dipole in the canonical orientation, and are much smaller in the $x-$ and $y-$directions. Agreement between the model and calculated site displacements is shown in Figure 7.3 for water molecules in their original crystal lattice orientation and the canonical orientation. The largest disagreement between the model and calculated displacement is $\sim$0.03 Å with 3% of oxygens having deviations larger than 0.02 Å. As shown in Figure 7.3, when all waters are similarly oriented, the deviations are magnified. The largest displacement obtained using predictions from the $\mathbf{d}_0^{\langle 100 \rangle}$ model was $\sim$0.04Å with 38% and 5% of oxygens having deviations larger than 0.02 and 0.03Å respectively.

7.4 Statistical Mechanical Results

We performed Metropolis Monte Carlo simulations on a simulation cell measuring eight primitive cells on each side containing 1024 water molecules. Results reported below were obtained from simulations at 1000 K, essentially infinite temperature for the H-bond orientations. Data obtained at lower temperatures for ice VII was

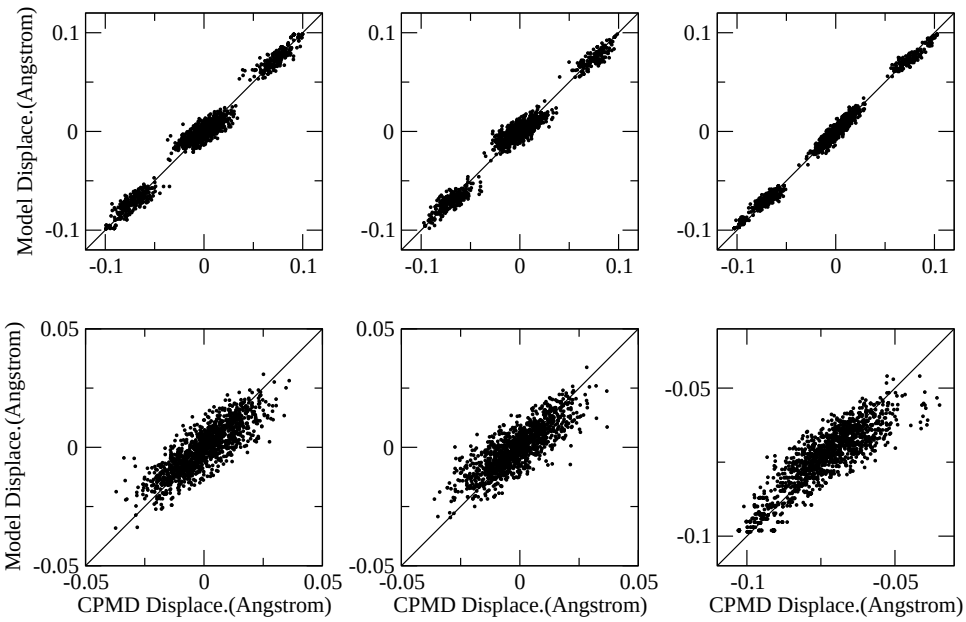

Figure 7.3: Fit of the oxygen-displacement model to the oxygen displacements of waters in the 50 optimized H-bond configurations. The top row shows the data for waters in their original orientation in the crystal lattice where the dipoles can point in any one of six directions. The bottom row shows data for all waters in the canonical orientation where their dipole now points towards positive z. The columns, left to right, show the agreement along the x, y, and z axes respectively. All points would lie on the straight line if there was perfect agreement.

essentially identical to data at 1000 K in line with the fact that only 7% of the configurational entropy is lost before the ordering transition in our simulations. [19, 20] Additional simulation details, including a description of the graph-invariant expression used here to describe H-bond fluctuations, are identical to those found in previous work on the ice VII/VIII proton ordering transition presented in chapter 2. Using the site-displacement model developed here, we calculated equilibrium distributions for the site displacements and oxygen-oxygen distances. As seen in Figure 7.4, the probability distributions obtained from the statistical mechanical simulations are similar

to those obtained from *ab initio* calculations on H-bond configurations chosen "semi-randomly" for the 32-water cell. For the oxygen-site displacement distribution, the peak near 0.1 Å in the data for the optimized geometries is mostly due to ice VIII like H-bond configurations, those with most neighboring water dipoles pointing in the same direction, which are rarely sampled at temperatures above the ordering transition. The 3-D probability distribution of the atomic center of oxygen displaced from

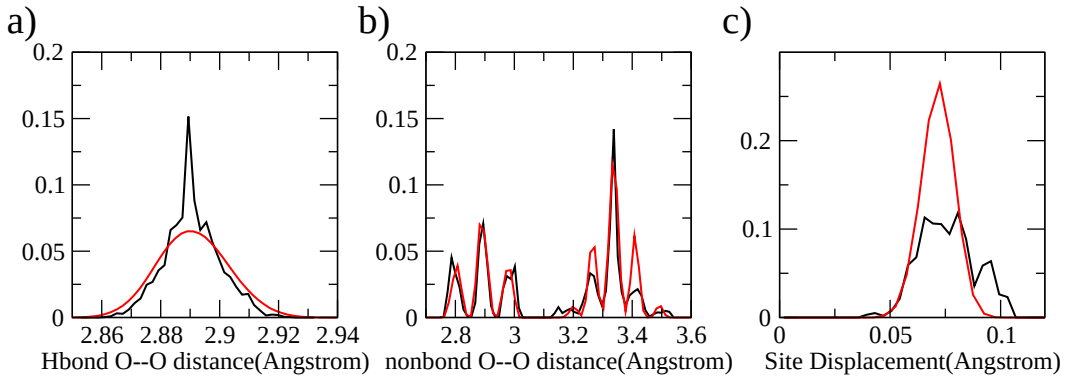

Figure 7.4: The red curves are the probability distributions for the bonded(a) and nonbonded(b) oxygen-oxygen distances calculated from Monte Carlo simulations at 1000 K. The black curves are the same as those shown in Figure 7.1 to compare with the simulated structure. (c) Probability distribution of the site displacement calculated from 50 H-bond configurations(black) and Monte Carlo simulations(red).

its perfect lattice site, obtained from Monte Carlo simulations at 1000 K, is shown in Figure 7.5a. The probability distribution is spread across six sites which are located on the $\langle 100 \rangle$ axes as discussed above. As one looks down an axis, the $z-$axis for example, one can see a $4-$fold symmetry in the probability density. Contour plots, projection onto the $xy-$plane, of the lobes lying on the negative $x-$axis and positive $z-$axis are shown in Figures 7.5b and c. In both contours, the largest probability of

finding the oxygen center is found to lie on the axes with probability decreasing away from the axis. The 4−fold symmetry is clearly seen in the contour plot of the lobe located on the positive $z-$axis viewed down the $z-$axis.

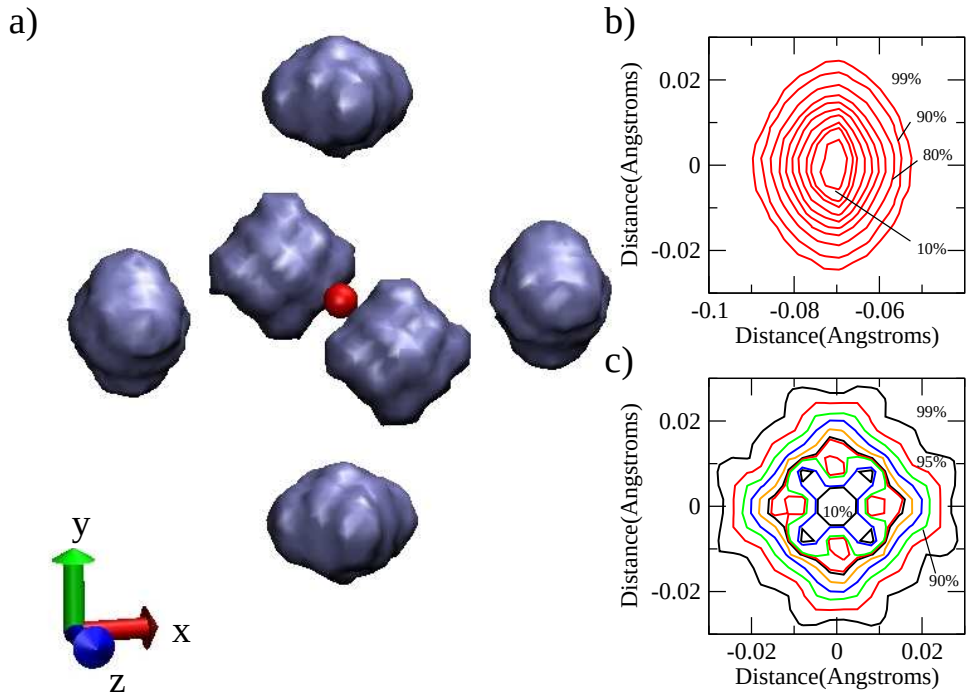

Figure 7.5: (a) 3-D probability distribution of the position of the oxygen centers relative to the perfect lattice site, small red sphere, obtained from Monte Carlo simulations at 1000 K. The center of each lobe is located on one of the $\langle 100 \rangle$ axes. (b) and (c) Contour plots of the probability distribution, projected onto the $xy-$plane, of the position of the oxygen centers relative to the perfect lattice site. (b) The oxygen sites closest to the negative $x-$axis, $[\bar{1}00]$, with some contours labeled indicating the fraction of oxygen atoms enclosed. The most probable location of the oxygen center is within the contour labeled 10%. (c) The oxygen sites closest to the positive $z-$axis, [001]. In both plots, starting from the contour labeled 90%, the contours decrease in increments of 10% as one looks towards the center of each distribution. For clarity, the 20% contour, nearly identical to the 30% contour, was omitted in (c).

7.5 Discussion

This work has described the success of expressing the displacement of an oxygen atom from its perfect lattice site, obtained from periodic DFT calculations, as a function of the surrounding H-bond topology. Combined with an analytic technique to describe H-bond fluctuations, graph invariants, we were able to perform statistical mechanical calculations on the site displacements in a large simulation cell. We find that the oxygen atoms are displaced along the $\langle 100 \rangle$ axes and not the recently suggested $\langle 111 \rangle$ axes. [138] The maximum of the probability distribution for the site displacements is near 0.071 Å. The hydrogen bonded oxygen-hydrogen and oxygen-oxygen distances had unimodal probability distributions with average lengths of 1.9073 and 2.8908 Å respectively. The nonbonded oxygen-oxygen probability distribution had three peaks separated by $\sim$0.1 Å with the central peak centered at the H-bonded oxygen-oxygen distance

The site displacement model is sufficient to explain the sub-lattice shift observed in anti-ferroelectric ice VIII. The model predicts a sub-lattice shift of 0.196 Å(0.203 Å) in agreement with the present calculated shift, 0.205 Å(0.204 Å), with a plane wave cutoff of 90 Ry(120 Ry) and previous experimental and calculated shifts. [45, 68, 139] By optimizing the H-bond configurations at increasing plane wave cutoffs, we found that the geometrical features, such as H-bonded oxygen-oxygen distances, are nearly converged by 90 Ry, although other properties, such as the energy and forces, need much larger cutoffs. [140] We have not attempted to calculate the thermal motion of the oxygen atoms, which would require lattice force constants available from our periodic electronic structure calculations, but the degree of static motion we observed here is already on the order of the site displacements observed experimentally.

BIBLIOGRAPHY

[1] Victor F. Petrenko and Robert W. Whitworth. *Physics of Ice*. Oxford University Press: New York, 1999.

[2] Rachel Howe and R. W. Whitworth. A determination of the crystal structure of ice XI. *J. Chem. Phys.*, 90(8):4450, 1989.

[3] S. M. Jackson, V. M. Nield, R. W. Whitworth, M. Oguro, and C. C. Wilson. Single-crystal neutron diffraction studies of the structure of ice XI. *J. Phys. Chem. B*, 101(32):6142, 1997.

[4] A. J. Leadbetter, R. C. Ward, J. W. Clark, P. A. Tucker, T. Matsuo, and H. Suga. The equilibrium low-temperature structure of ice. *J. Chem. Phys.*, 82(1):424, 1985.

[5] Christina M. B. Line and R. W. Whitworth. A high resolution neutron powder diffraction study of D_2O ice XI. *J. Chem. Phys.*, 104(24):10008, 1996.

[6] S. M. Jackson and R. W. Whitworth. Evidence for ferroelectric ordering in ice Ih. *J. Chem. Phys.*, 103(17):7647, 1995.

[7] S. M. Jackson and R. W. Whitworth. Thermally-stimulated depolarization studies of the ice XI−ice Ih phase transition. *J. Phys. Chem. B*, 101(32):6177, 1997.

[8] H. T. Stokes and D. M. Hatch, 2004. FINDSYM, stokes.byu.edu/isotropy.html.

[9] Sam J. La Placa, Walter C. Hamilton, Barclay Kamb, and Anand Prakash. On a nearly proton-ordered structure for ice IX. *J. Chem. Phys.*, 58(2):567, 1973.

[10] J. F. Nagle. Lattice statistics of hydrogen bonded crystals. I. The residual entropy of ice. *J. Math. Phys.*, 7(8):1484, 1966.

[11] Rachel Howe and R. W. Whitworth. The configurational entropy of partially ordered ice. *J. Chem. Phys.*, 86(11):6443, 1987.

[12] Colin Lobban, John L. Finney, and Werner F. Kuhs. The structure and ordering of ices III and V. *J. Chem. Phys.*, 112(16):7169, 2000.

[13] Daniel T. Colbert and William H. Miller. A novel discrete variable representation for quantum mechanical reactive scattering via the S-matrix Kohn method. *J. Chem. Phys.*, 96(3):1982, 1992.

[14] J. D. Londono, W. F. Kuhs, and J. L. Finney. Neutron diffraction studies of ices III and IX on under-pressure and recovered samples. *J. Chem. Phys.*, 98(6):4878, 1993.

[15] Linus Pauling. The structure and entropy of ice and of other crystals with some randomness of atomic arrangement. *J. Am. Chem. Soc.*, 57:2680, 1935.

[16] W. F. Giauque and J. W. Stout. The entropy of water and the third law of thermodynamics. The heat capacity of ice from 15 to 273°K. *J. Am. Chem. Soc.*, 58:1144, 1936.

[17] Y. Tajima, T. Matsuo, and H. Suga. Phase transition in KOH-doped hexagonal ice. *Nature(London)*, 299:810, 1982.

[18] M. J. Iedema, M. J. Dresser, D. L. Doering, J. B. Rowland, W. P. Hess, A. A. Tsekouras, and J. P. Cowin. Ferroelectricity in water ice. *J. Phys. Chem. B*, 102(46):9203, 1998.

[19] Sherwin J. Singer, Jer-Lai Kuo, Tomas K. Hirsch, Chris Knight, Lars P. Ojamäe, and Michael L. Klein. Hydrogen bond topology and the ice VII/VIII and Ih/XI proton ordering phase transitions. *Phys. Rev. Lett.*, 94(13):135701, 2005.

[20] Chris Knight, Sherwin J. Singer, Jer-Lai Kuo, Tomas K. Hirsch, Lars Ojamäe, and Michael L. Klein. Hydrogen bond topology and the ice VII/VIII and Ih/XI proton ordering phase transition. *Phys. Rev. E*, 73(5):056113, 2006.

[21] V. Buch, P. Sandler, and J. Sadlej. Simulations of H_2O solid, liquid, and clusters, with emphasis on ferroelectric ordering transition in hexagonal ice. *J. Phys. Chem. B*, 102(44):8641, 1998.

[22] Jer-Lai Kuo and Sherwin J. Singer. Graph invariants for periodic systems: towards predicting physical properties from the hydrogen bond topology of ice. *Phys. Rev. E*, 67(1):016114, 2003.

[23] Chris Knight and Sherwin J. Singer. Prediction of a phase transition to a hydrogen bond ordered form of ice VI. *J. Phys. Chem. B*, 109(44):21040, 2005.

[24] Chris Knight and Sherwin J. Singer. A reexamination of the ice III/IX hydrogen bond ordering phase transition. *J. Chem. Phys.*, 125(6):064506, 2006.

[25] Christoph G. Salzmann, Paolo G. Radaelli, Andreas Hallbrucker, Erwin Mayer, and John L. Finney. The preparation and structures of hydrogen ordered phases of ice. *Science*, 311:1758, 2006.

[26] Chris Knight and Sherwin J. Singer. Hydrogen bond ordering in ice V and the transition to ice XIII. *J. Chem. Phys.*, 129(16):164513, 2008.

[27] Paul J. Wooldridge and Paul Devlin. Proton trapping and defect energetics in ice from FT-IR monitoring of photoinduced isotopic exchange of isolated D_2O. *J. Chem. Phys.*, 88(5):3086, 1988.

[28] J. P. Cowin, A. A. Tsekouras, M. J. Iedema, K. Wu, and G. B. Ellison. Immobility of protons in ice from 30 to 190K. *Nature(London)*, 398(6726):405, 1999.

[29] C. Knight and S. J. Singer. Theoretical study of a hydroxide ion within the ice-Ih lattice. In Werner F. Kuhs, editor, *Physics and chemistry of ice*, Symposium on the Physics and Chemistry of Ice, page 339, Cambridge, April 2007. The Royal Society of Chemistry.

[30] Hiroshi Suga. A facet of recent ice sciences. *Thermochim. Acta*, 300:117, 1997.

[31] G. P. Johari and E. Whalley. The dielectric properties of ice Ih in the range 272−133K. *J. Chem. Phys.*, 75(3):1333, 1981.

[32] S. Kawada and J. Niinuma. Curie-Weiss behavior of the static dielectric constant of the debye component in ice Ih. *J. Phys. Soc. Jap.*, 43(2):715, 1977.

[33] S. Kawada. Dielectric anisotropy in ice Ih. *J. Phys. Soc. Jap.*, 44(6):1881, 1978.

[34] Shuji Kawada. Dielectric dispersion and phase transition of KOH doped ice. *J. Phys. Soc. Jpn.*, 32(5):1442, 1972.

[35] Hiroshi Fukazawa, Shinji Mae, Susumu Ikeda, and Okitsugu Watanabe. Proton ordering in Antarctic ice observed by Raman and neutron scattering. *Chem. Phys. Lett.*, 294:554, 1998.

[36] Y. Wang, J. C. Li, A. I. Kolesnikov, S. Parker, and S. J. Johnsen. Inelastic neutron scattering investigation of Greenland ices. *Physica B*, 276−278:282, 2000.

[37] A. D. Fortes, I. G. Wood, D. Grigoriev, M. Alfredsson, S. Kipfstuhl, K. S. Knight, and R. I. Smith. No evidence for large-scale proton ordering in Antarctic ice from powder neutron diffraction. *J. Chem. Phys.*, 120(24):11376, 2004.

[38] G. P. Johari. An interpretation for the thermodynamic features of ice Ih/XI transformation. *J. Chem. Phys.*, 109(21):9543, 1998.

[39] Marinus Kunst and John M. Warman. Nanosecond time-resolved conductivity studies of pulse-ionized ice. 2. The mobility and trapping of protons. *J. Chem. Phys.*, 87(21):4093, 1983.

[40] Madhusudan Tyagi and S. S. N. Murthy. Dielectric relaxation in ice and ice clathrates and its connection to the low-temperature phase transition induced by alkali hydroxides as dopants. *J. Phys. Chem. A*, 106(20):5072, 2002.

[41] P. W. Bridgman. The phase diagram of water to 45,000 kg/cm^2. *J. Phys. Chem.*, 5:964, 1937.

[42] Barclay Kamb and Briant L. Davis. Ice VII, the densest form of ice. *Proc. Natl. Acad. Sci. U.S.A.*, 52(6):1433, 1964.

[43] G. E. Walrafen, M. Abebe, F. A. Mauer, S. Block, G. J. Piermarini, and R. Munro. Raman and x-ray investigations of ice VII to 36.0 GPa. *J. Chem. Phys.*, 77(4):2166, 1982.

[44] W. F. Kuhs, J. L. Finney, C. Vettier, and D. V. Bliss. Structure and hydrogen ordering in ices VI, VII and VIII by neutron powder diffraction. *J. Chem. Phys.*, 81(8):3612, 1984.

[45] R. J. Nelmes, J. S. Loveday, R. M. Wilson, J. M. Besson, Ph. Pruzan, S. Klotz, G. Hamel, and S. Hull. Neutron diffraction study of the structure of deuterated ice VII to 10 GPa. *Phys. Rev. Lett.*, 71(8):1192, 1993.

[46] E. Whalley, D. W. Davidson, and J. B. R. Heath. Dielectric properties of ice VII. ice VIII: A new phase of ice. *J. Chem. Phys.*, 45(11):3976, 1966.

[47] G. P. Johari, A. Lavergne, and E. Whalley. Dielectric properties of ice VII and VIII and the phase boundary between ice VI and VII. *J. Chem. Phys.*, 61(10):4292, 1974. [erratum: *ibid.* **73**, 4150 (1980)].

[48] Ph. Pruzan, J. C. Chervin, and B. Canny. Determination of the D_2O ice VII-VIII transition line by raman scattering up to 51 GPa. *J. Chem. Phys.*, 97(1):718, 1992.

[49] Carl W. F. T. Pistorius, Eliezer Rapoport, and J. B. Clark. Phase diagram of H_2O and D_2O at high pressures. *J. Chem. Phys.*, 48(12):5509, 1968.

[50] Shannon McDonald, Lars Ojamäe, and Sherwin J. Singer. Graph theoretical generation and analysis of hydrogen-bonded structures with applications to the neutral and protonated water cube and dodecahedral clusters. *J. Phys. Chem. A*, 102(17):2824, 1998.

[51] Jer-Lai Kuo, James V. Coe, Sherwin J. Singer, Yehuda B. Band, and Lars Ojamäe. On the use of graph invariants for efficiently generating hydrogen bond topologies and predicting physical properties of water clusters and ice. *J. Chem. Phys.*, 114(6):2527, 2001.

[52] Stephen D. Belair, Joseph S. Francisco, and Sherwin J. Singer. Hydrogen bonding in cubic $(H_2O)_8$ and $OH\cdot(H_2O)_7$ clusters. *Phys. Rev. A*, 71(1):013204, 2005.

[53] N. Bjerrum. Structure and properties of ice. *Science*, 115:386, 1952.

[54] Tomas K. Hirsch and Lars Ojamäe. Quantum-chemical and force-field investigations of ice Ih: Computation of proton-ordered structures and prediction of their lattice energies. *J. Phys. Chem. B*, 108(40):15856, 2004.

[55] D. J. McGinty. Vapor phase homogeneous nucleation and the thermodynamical properties of small clusters of argon atoms. *J. Chem. Phys.*, 55(2):580, 1971.

[56] J. J. Burton. Vibrational frequencies and entropies of small clusters of atoms. *J. Chem. Phys.*, 56(6):3133, 1972.

[57] M. R. Hoare. Structure and dynamics of simple microclusters. *Adv. Chem. Phys.*, 40:49, 1979.

[58] Frank H. Stillinger and Thomas A. Weber. Hidden structure in liquids. *Phys. Rev. A*, 25(2):978, 1982.

[59] Frank H. Stillinger and Thomas A. Weber. Dynamics of structural transitions in liquids. *Phys. Rev. A*, 28(4):2408, 1983.

[60] Paul G. Mezey. *Potential Energy Hypersurfaces*, volume 53 of *Studies in Physical and Theoretical Chemistry*. Elsevier:New York, 1987.

[61] G. Franke, E. R. Hilf, and P. Borrmann. The structure of small clusters: multiple normal modes model. *J. Chem. Phys.*, 98(4):3496, 1993.

[62] David J. Wales. Coexistence in small inert gas clusters. *Mol. Phys.*, 78(1):151, 1993.

[63] Jonathan P. K. Doye and David J. Wales. Calculation of thermodynamic properties of small Lennard-Jones clusters incorporating anharmonicity. *J. Chem. Phys.*, 102(24):9659, 1995.

[64] Kurt Binder, editor. *Monte Carlo Methods in Statistical Physics*, volume 7 of *Topics in Current Physics*. Springer, New York, 2nd edition, 1986.

[65] M. Matsumoto and T. Nishimura. Mersenne twister: a 623-dimensionally equidistributed uniform pseudorandom number generator. *ACM Trans. Model. Comput. Simul.*, 8(1):3, 1998.

[66] Aneesur Rahman and Frank H. Stillinger. Proton distribution in ice and the Kirkwood correlation factor. *J. Chem. Phys.*, 57(9):4009, 1972.

[67] Steven W. Rick and A. D. J. Haymet. Dielectric constant and proton order and disorder in ice Ih: Monte carlo computer simulations. *J. Chem. Phys.*, 118(20):9291, 2003.

[68] Jer-Lai Kuo and Michael L. Klein. Structure of ice-VII and ice-VIII: A quantum mechanical study. *J. Phys. Chem. B*, 108(51):19634, 2004.

[69] R. Car and M. Parrinello. Unified approach for molecular dynamics and density-functional theory. *Phys. Rev. Lett.*, 55(22):2471, 1985.

[70] Roberto Car and Michele Parrinello. The unified approach for molecular dynamics and density functional theory. In A. Polian, P. Loubeyre, and N. Boccara, editors, *Simple Molecular Systems Very High Density*, volume 186, page 455. Plenum, NATO ASI Ser. B, New York, 1989.

[71] CPMD, Copyright IBM Corp. 1990-2006, Copyright MPI für Festkörperforschung Stuttgart 1997-2001.

[72] A. D. Becke. Density-functional exchange-energy approximation with correct asymptotic behavior. *Phys. Rev. A*, 38(6):3098, 1988.

[73] C. Lee, W. Yang, and R. G. Parr. Development of the Colle-Salvetti correlation-energy formula into a functional of the electron density. *Phys. Rev. B*, 37:785, 1988.

[74] N. Troullier and José Luriaas Martins. Efficient pseudopotentials for plane-wave calculations. *Phys. Rev. B*, 43(3):1993, 1991.

[75] B. Delley. An all-electron numerical method for solving the local density functional for polyatomic molecules. *J. Chem. Phys.*, 92(1):508, 1990.

[76] V. Milman, B. Winkler, J. A. White, C. J. Pickard, M. C. Payne, E. V. Akhmatskaya, and R. H. Nobes. Electronic structure, properties, and phase stability of inorganic crystals: A pseudopotential plane-wave study. *Int. J. Quantum Chem.*, 77(5):895, 2000.

[77] John P. Perdew and Yue Wang. Accurate and simple density functional for the electronic exchange energy: Generalized gradient approximation. *Phys. Rev. B*, 33(12):8800, 1986.

[78] John P. Perdew. In Paul Ziesche and Helmut Eschrig, editors, *Electronic Structure of Solids, '91*, page 11, Berlin, 1991. Wissenschaftsbereich Theoretische Physik, Akademie Verlag.

[79] John P. Perdew and Yue Wang. Accurate and simple analytic representation of the electron-gas correlation energy. *Phys. Rev. B*, 45(23):13244, 1992.

[80] Yoshimitsu Tajima, Takasuke Matsuo, and Hiroshi Suga. Calorimetric study of phase transition in hexagonal ice doped with alkali hydroxides. *J. Phys. Chem. Solids*, 45(11-12):1135, 1984.

[81] Takasuke Matsuo, Yoshimitsu Tajima, and Hiroshi Suga. Calorimetric study of a phase transition in D_2O ice Ih doped with KOD: ice XI. *J. Phys. Chem. Solids*, 47(2):165, 1986.

[82] Takasuke Matsuo and Hiroshi Suga. Calorimetric study of ices Ih doped with alkali hydroxides and other impurities. *J. Phys., Colloq.*, 48(C1):477, 1987.

[83] Barclay Kamb and Anand Prakash. Structure of ice III. *Acta Crystallogr., Sect. B: Struct. Crystallogr. Cryst. Chem.*, B24:1317, 1968.

[84] E. Whalley, J. B. R. Heath, and D. W. Davidson. Ice IX: An antiferroelectric phase related to ice III. *J. Chem. Phys.*, 48(5):2362, 1968.

[85] K. Nishibata and E. Whalley. Thermal effects of the transformation ice III−IX. *J. Chem. Phys.*, 60(8):3189, 1974.

[86] Barclay Kamb. Structure of ice VI. *Science*, 150:205, 1965.

[87] Barclay Kamb. Crystallography of ice. In E. Whalley, Jones S. J., and L. W. Gold, editors, *Physics and chemistry of ice*, Symposium on the Physics and Chemistry of Ice, page 28, Ottawa, August 1972. Royal Society of Canada.

[88] G. P. Johari and E. Whalley. Dielectric properties of ice VI at low temperatures. *J. Chem. Phys.*, 64(11):4484, 1976.

[89] G. P. Johari and E. Whalley. Evidence for a very slow transformation in ice VI at low temperatures. *J. Chem. Phys.*, 70(5):2094, 1979.

[90] H. J. Monkhorst and J. D. Pack. Special points for brillouin-zone integrations. *Phys. Rev. B*, 13(12):5188, 1976.

[91] B. Kamb and S. J. La Placa. Reversible order-disorder transformation in ice V. *EOS Trans. Am. Geophys. Union*, 55:1202, 1974.

[92] G. Tammann. Ueber die Grenzen des festen Zustandes IV. *Ann. Phys.*, 2:1, 1900.

[93] Ronald L. McFarlan. The structure of ice III. *J. Chem. Phys.*, 4:253, 1936.

[94] J. E. Bertie, L. D. Calvert, and E. Whalley. Transformations of ice II, ice III, and ice V at atmospheric pressure. *J. Chem. Phys.*, 38(4):840, 1963.

[95] G. P. Arnold, R. G. Wenzel, S. W. Rabideau, N. G. Nereson, and A. L. Bowman. Neutron diffraction study of ice polymorphs under helium pressure. *J. Chem. Phys.*, 55(2):589, 1971.

[96] J. E. Bertie and E. Whalley. Infrared spectra of ices II, III, and V in the range 4000 to 350 cm^{-1}. *J. Chem. Phys.*, 40(6):1646, 1964.

[97] Y. P. Handa, D. D. Klug, and E. Whalley. Energies of the phases of ice at low temperature and pressure relative to ice Ih. *Can. J. Chem.*, 66:919, 1988.

[98] J. F. Nagle. In E. Whalley, Jones S. J., and L. W. Gold, editors, *Physics and chemistry of ice*, Symposium on the Physics and Chemistry of Ice, page 70, Ottawa, August 1972. Royal Society of Canada.

[99] Isao Minagawa. Ferroelectric phase transition and anisotropy of dielectric constant in ice Ih. *J. Phys. Soc. Jap.*, 50(11):3669, 1981.

[100] Luis G. MacDowell, Eduardo Sanz, Carlos Vega, and José Luis F. Abascal. Combinatorial entropy and phase diagram of partially ordered ice phases. *J. Chem. Phys.*, 121(20):10145, 2004.

[101] J. D. Bernal and R. H. Fowler. A theory of water and ionic solution, with particular reference to hydrogen and hydroxyl ions. *J. Chem. Phys.*, 1(8):515, 1933.

[102] Jer-Lai Kuo. The low-temperature proton-ordered phases of ice predicted by ab-initio methods. *Phys. Chem. Chem. Phys.*, 7(21):3733, 2005.

[103] Jer-Lai Kuo, Michael L. Klein, and Werner F. Kuhs. The effect of proton disorder on the structure of ice-Ih: A theoretical study. *J. Chem. Phys.*, 123:134505, 2005.

[104] C. G. Salzmann, P. G. Radaelli, A. Hullbrucker, E. Mayer, and J. L. Finney. New hydrogen ordered phases of ice. In Werner F. Kuhs, editor, *Physics and chemistry of ice*, Symposium on the Physics and Chemistry of Ice, page 521, Cambridge, April 2007. Royal Society of Chemistry.

[105] Christoph G. Salzmann, Andreas Hallbrucker, John L. Finney, and Erwin Mayer. Raman spectroscopic study of hydrogen ordered ice XIII and of its reversible phase transition to disordered ice V. *Phys. Chem. Chem. Phys.*, 8:3088, 2006.

[106] V. M. Nield and R. W. Whitworth. The structure of ice Ih from analysis of single-crystal neutron diffuse scattering. *J. Phys.: Condens. Matter*, 7(43):8259, 1995.

[107] Barclay Kamb, Anand Prakash, and Carolyn Knobler. Structure of ice V. *Acta Crystallogr.*, 22:706, 1967.

[108] W. C. Hamilton, B. Kamb, S. J. La Placa, and A. Prakash. Deuteron arrangements in high-pressure forms of ice. In Nikolaus Riehl, Bernhard Bullemer, and Hermann Engelhardt, editors, *Physics of ice*, International Symposium on Physics of Ice, page 44, New York, 1969. Plenum Press.

[109] G. J. Wilson, R. K. Chan, D. W. Davidson, and E. Whalley. Dielectric properties of ices II, III, V, and VI. *J. Chem. Phys.*, 43(7):2384, 1965.

[110] Y. P. Handa, D. D. Klug, and E. Whalley. Phase transitions of ice V and VI. *J. Phys. (Paris)*, 48(C1):435, 1987.

[111] G. P. Johari and E. Whalley. The dielectric relaxation time of ice V, its partial anti-ferroelectric ordering and the role of bjerrum defects. *J. Chem. Phys.*, 115(7):3274, 2001.

[112] E. A. DiMarzio and F. H. Stillinger. Residual entropy of ice. *J. Chem. Phys.*, 40(6):1577, 1964.

[113] C. Knight and S. J. Singer. Tackling the problem of hydrogen bond order and disorder in ice. In Werner F. Kuhs, editor, *Physics and chemistry of ice*, Symposium on the Physics and Chemistry of Ice, page 329, Cambridge, April 2007. Royal Society of Chemistry.

[114] Gareth A. Tribello and Ben Slater. Proton ordering energetics in ice phases. *Chem. Phys. Lett.*, 425(4-6):246, 2006.

[115] John P. Perdew, Kieron Burke, and Matthias Ernzerhof. Generalized gradient approximation made simple. *Phys. Rev. Lett.*, 77(18):3865, 1996.

[116] Yingkai Zhang and Weitao Yang. Comment on "Generalized gradient approximation made simple". *Phys. Rev. Lett.*, 80(4):890, 1998.

[117] Christoph G. Salzmann, Paolo G. Radaelli, John L. Finney, and Erwin Mayer. A calorimetric study on the low temperature dynamics of doped ice V and its reversible phase transition to hydrogen ordered ice XIII. *Phys. Chem. Chem. Phys.*, 10:6313, 2008.

[118] H. Eugene Stanley. *Introduction to Phase Transitions and Critical Phenomena*. Oxford University Press, New York, 1971.

[119] L. D. Landau and E. M. Lifshitz. *Statistical Physics, Course of Theoretical Physics Vol. 5*. Pergamon, New York, 3rd edition, 1980.

[120] Michael E. Fisher. Scaling, universality and renormalization group theory. In F. J. W. Hahne, editor, *Critical Phenomena*, page 1. Springer, New York, 1983.

[121] R. W. Whitworth. Comment on "Ferroelectricty in water ice". *J. Phys. Chem. B*, 103(38):8192, 1999.

[122] J. P. Cowin and M. J. Iedema. Reply to comment on "Ferroelectricty in water ice". *J. Phys. Chem. B*, 103(38):8194, 1999.

[123] R. P. Wayne. *Chemistry of Atmospheres*. Oxford University Press, Oxford, 1991.

[124] Gary Ritzhaupt and J. P. Devlin. Direct spectroscopic observation of proton transfer rates: activation energy for proton exchange in ice Ic. *Chem. Phys. Lett.*, 65(3):592, 1979.

[125] William B. Collier, Gary Ritzhaupt, and J. Paul Devlin. Spectroscopically evaluated rates and energies for proton transfer and bjerrum defect migration in cubic ice. *J. Phys. Chem.*, 88(3):363, 1984.

[126] J. Paul Devlin. Vibrational spectra and point defect activities of icy solids and gas phase clusters. *Int. Rev. Phys. Chem.*, 9(1):29, 1990.

[127] Bin Chen, Jung Mee Park, Ivaylo Ivanov, Gloria Tabacchi, Michael L. Klein, and Michele Parrinello. First-principles study of aqueous hydroxide solutions. *J. Am. Chem. Soc.*, 124(29):8534, 2002.

[128] Bin Chen, Ivaylo Ivanov, Jung Mee Park, Michele Parrinello, and Michael L. Klein. Solvation structure and mobility mechanism of OH^-: A Car-Parrinello molecular dynamics investigation of alkaline solutions. *J. Phys. Chem. B*, 106(46):12006, 2002.

[129] Zhongwei Zhu and Mark E. Tuckerman. Ab initio molecular dynamics investigation of the concentration dependence of charged defect transport in basic solutions via calculation of the infrared spectrum. *J. Phys. Chem. B*, 106(33):8009, 2002.

[130] Mark E. Tuckerman, Dominik Marx, and Michele Parrinello. The nature and transport mechanism of hydrated hydroxide ions in aqueous solution. *Nature*, 417:925, 2002.

[131] D. Asthagiri, Lawrence R. Pratt, J. D. Kress, and M. A. Gomez. The hydration state of HO^-(aq). *Chem. Phys. Lett.*, 380(5-6):530, 2003.

[132] D. Asthagiri, Lawrence R. Pratt, J. D. Kress, and M. A. Gomez. Hydration and mobility of HO^-. *Proc. Nat. Acad. Sci. U.S.A.*, 101(19):7229, 2004.

[133] M. E. Tuckerman, A Chandra, and D. Marx. Structure and dynamics of HO^-. *Acc. Chem. Res.*, 39(2):151, 2006.

[134] R. Podeszwa and V. Buch. Structure and dynamics of orientational defects in ice. *Phys. Rev. Lett.*, 83(22):4570, 1999.

[135] Lukasz Cwiklik and Victoria Buch. Hydroxide trapped in the interior of ice: a computational study. *Phys. Chem. Chem. Phys.*, 11(9):1294, 2009.

[136] Maurice de Koning, Alex Antonelli, Antonio J. R. da Silva, and A. Fazzio. Orientational defects in ice Ih: An interpretation of electrical conducitivity measurements. *Phys. Rev. Lett.*, 96(7):075501, 2006.

[137] James D. Jorgensen and Thomas G. Worlton. Disordered structure of D_2O ice VII from *in situ* neutron powder diffraction. *J. Chem. Phys.*, 83(1):329, 1985.

[138] R. J. Nelmes, J. S. Loveday, W. G. Marshall, G. Hamel, J. M. Besson, and S. Klotz. Multisite disordered structure of ice VII to 20 GPa. *Phys. Rev. Lett.*, 81(13):2719, 1998.

[139] Lars Ojamäe, Kersti Hermansson, Roberto Dovesi, Carla Roetti, and V. R. Saunders. Mechanical and molecular properties of ice VIII from crystal-orbital *ab initio* calculations. *J. Chem. Phys.*, 100(3):2128, 1994.

[140] Hee-Seung Lee and Mark E. Tuckerman. Ab initio molecular dynamics with discrete variable representation basis sets: techniques and application to liquid water. *J. Phys. Chem. A*, 110(16):5549, 2006.